

# SN 2022oqm – a Ca-rich Explosion of a Compact Progenitor Embedded in C /O Circumstellar Material

Ido Irani,<sup>1</sup> Ping Chen,<sup>1</sup> Jonathan Morag,<sup>1</sup> Steve Schulze,<sup>2</sup> Avishay Gal-Yam,<sup>1</sup> Nora L. Strotjohann,<sup>1</sup> Ofer Yaron,<sup>1</sup> Erez A. Zimmerman,<sup>1</sup> Amir Sharon,<sup>1</sup> Daniel A. Perley,<sup>3</sup> J. Sollerman,<sup>4</sup> Aaron Tohuvaohu,<sup>5</sup> Kaustav K. Das,<sup>6</sup> Mansi M. Kasliwal,<sup>6</sup> Rachel Bruch,<sup>1</sup> Thomas G. Brink,<sup>7,8</sup> WeiKang Zheng,<sup>7,9</sup> Alexei V. Filippenko,<sup>7</sup> Kishore C. Patra,<sup>7,10</sup> Sergiy S. Vasylyev,<sup>7,11</sup> Yi Yang,<sup>7,12</sup> Matthew J. Graham,<sup>6</sup> Joshua S. Bloom,<sup>7,13</sup> Paolo Mazzali,<sup>3,14</sup> Josiah Purdum,<sup>6</sup> Russ R. Laher,<sup>15</sup> Avery Wold,<sup>15</sup> Yashvi Sharma,<sup>6</sup> Leander Lacroix,<sup>16</sup> and Michael S. Medford<sup>7,13</sup>

<sup>1</sup>Department of Particle Physics and Astrophysics, Weizmann Institute of Science, 234 Herzl St, 7610001 Rehovot, Israel

<sup>2</sup>Department of Physics, The Oskar Klein Center, Stockholm University, AlbaNova, SE-10691 Stockholm, Sweden

<sup>3</sup>Astrophysics Research Institute, Liverpool John Moores University, IC2 Liverpool Science Park, 146 Brownlow Hill, Liverpool L3 5RF, UK

<sup>4</sup>Department of Astronomy, The Oskar Klein Center, Stockholm University, AlbaNova, SE-10691 Stockholm, Sweden

<sup>5</sup>David A. Dunlap Department of Astronomy and Astrophysics, University of Toronto, Toronto, ON, Canada

<sup>6</sup>Division of Physics, Mathematics and Astronomy, California Institute of Technology, Pasadena, CA 91125, USA

<sup>7</sup>Department of Astronomy, University of California, Berkeley, CA 94720-3411, USA

<sup>8</sup>Wood Specialist in Astronomy

<sup>9</sup>Eustace Specialist in Astronomy

<sup>10</sup>Nagaraj-Noll-Otellini Graduate Fellow

<sup>11</sup>Steven Nelson Graduate Fellow

<sup>12</sup>Bengier-Winslow-Robertson Postdoctoral Fellow

<sup>13</sup>Lawrence Berkeley National Laboratory, 1 Cyclotron Road, MS 50B-4206, Berkeley, CA 94720, USA

<sup>14</sup>Max-Planck Institute for Astrophysics, Garching, Germany

<sup>15</sup>IPAC, California Institute of Technology, 1200 E. California Boulevard, Pasadena, CA 91125, USA

<sup>16</sup>LPNHE, Sorbonne-Université, Paris

## Abstract

We present the discovery and analysis of SN 2022oqm, a Type Ic supernova (SN) detected  $< 1$  day after explosion. The SN rises to a blue and short-lived (2 days) initial peak. Early-time spectral observations of SN 2022oqm show a hot (40,000 K) continuum with high-ionization C and O absorption features at velocities of  $4000 \text{ km s}^{-1}$ , while its photospheric radius expands at  $20,000 \text{ km s}^{-1}$ , indicating a pre-existing distribution of expanding C/O material. After  $\sim 2.5$  days, both the spectrum and light curves evolve into those of a typical SN Ic, with line velocities of  $\sim 10,000 \text{ km s}^{-1}$ , in agreement with the photospheric radius evolution. The optical light curves reach a second peak at  $t \approx 15$  days. By  $t = 60$  days, the spectrum of SN 2022oqm becomes nearly nebular, displaying strong Ca II and [Ca II] emission with no detectable [O I], marking this event as Ca-rich. The early behavior can be explained by  $10^{-3} M_{\odot}$  of optically thin circumstellar material (CSM) surrounding either (1) a massive compact progenitor such as a Wolf-Rayet star, (2) a massive stripped progenitor with an extended envelope, or (3) a binary system with a white dwarf. We propose that the early-time light curve is powered by both interaction of the ejecta with the optically thin CSM and shock cooling (in the massive-star scenario). The observations can be explained by CSM that is optically thick to X-ray photons, is optically thick in the lines as seen in the spectra, and is optically thin to visible-light continuum photons that come either from downscattered X-rays or from the shock-heated ejecta. Calculations show that this scenario is self-consistent.

## 1. Introduction

While the light curves of Type Ia supernovae (SNe Ia) are well explained by the radioactive decay of  $^{56}\text{Ni}$ , many core-collapse SNe (CCSNe) require an additional powering mechanism for their early-time light curves (For reviews, see Maguire 2017; Arcavi 2017; Pian & Mazzali 2017, and references therein). In the absence of circumstellar material (CSM), the early ultraviolet (UV) through optical light curves of SNe are expected to be the result of shock breakout from the stellar surface (Matzner & McKee 1999), or due to the subsequent cooling of the shocked material (for a review, see Waxman & Katz 2017; Levinson & Nakar 2020).

If CSM is present, an early-time UV-optical component can be explained by the breakout of a radiation-mediated shock (RMS) from the CSM (Campana et al. 2006; Waxman et al. 2007; Ofek et al. 2010, 2014b; Waxman & Katz 2017; Förster et al. 2018), or possibly due to interaction of the ejecta with confined CSM ejected shortly ( $\sim 1$  yr) prior to explosion (Murase et al. 2014; Maeda et al. 2021; Maeda & Moriya 2022). In contrast, interaction resulting from progenitors with typical Wolf-Rayet (W-R) stellar winds is not expected to contribute to the optical light curve in SNe Ib/c (Chevalier & Fransson 2006).

The early-time light curves and spectra of SNe are sensitive to the properties of the progenitor star. If shock cooling is the dominant source of energy, the early light curves will be sensitive to the progenitor radius and mass, as well as to the slope of the outer density profile (Nakar & Sari 2010; Rabinak & Waxman 2011; Piro 2015; Sapir & Waxman 2017; Piro et al. 2021; Morag et al. 2022). If there is confined CSM around the progenitor star, the result of elevated mass loss in the months prior to explosion (e.g., Ofek et al. 2014a; Strotjohann et al. 2021), early-time SN spectra can show narrow high-ionization features (Gal-Yam et al. 2014; Khazov et al. 2016; Yaron et al. 2017; Bruch et al. 2021; Jacobson-Galán et al. 2022b).

The past decade has seen a rapid increase in the early detection of SNe by high-cadence wide-field surveys such as the Palomar Transient Factory (PTF; Law et al. 2009; Kulkarni 2013), which detected several such SNe (Gal-Yam et al. 2011; Arcavi et al. 2011; Nugent et al. 2011; Gal-Yam et al. 2014; Ben-Ami et al. 2014; Khazov et al. 2016; Yaron et al. 2017). Since then, the Astroid-Terrestrial impact Last Alert System (ATLAS; Tonry et al. 2018), the Zwicky Transient Facility (ZTF; Bellm et al. 2019; Graham et al. 2019), the Distance Less than 40 Mpc Survey (DLT40; Tartaglia et al. 2018), and most recently the Young Supernovae Experiment (YSE; Jones et al. 2021) have been conducting 1–3 day cadence wide-

field surveys and regularly detect SNe (e.g. Ho et al. 2019; Soumagnac et al. 2020; Bruch et al. 2021; Gal-Yam et al. 2022; Perley et al. 2022; Terreran et al. 2022; Jacobson-Galán et al. 2022b; Tinyanont et al. 2022; Hosseinzadeh et al. 2022) and fast-transients (e.g. Perley et al. 2018; Ho et al. 2020b; Perley et al. 2021; Ofek et al. 2021) shortly after explosion. Consequently, the study of the early emission from SN explosions is at the forefront of current efforts in the field (Modjaz et al. 2019).

While the early evolution of SNe II and IIB is relatively well studied (Bersten et al. 2012; Gal-Yam et al. 2014; Rubin et al. 2016; Garnavich et al. 2016; Rubin & Gal-Yam 2017; Arcavi et al. 2017; Khazov et al. 2016; Bersten et al. 2018; Prentice et al. 2020; Bruch et al. 2021; Ganot et al. 2022; Martinez et al. 2022; Medler et al. 2022), multiband observations in both UV and visible light have been obtained during the first few days for only a handful of stripped-envelope SNe (SESNe; but see Taddia et al. 2015). Occasionally, a coincident gamma-ray burst (GRB) or X-ray flash (XRF) resulted in intense UV-optical follow-up observations (Campana et al. 2006; Soderberg et al. 2008). Several other well-studied normal and peculiar SNe Ic (De et al. 2018; Horesh et al. 2020), broad-lined SNe Ic (Ic-BL; reported by Ho et al. 2019, 2020a), and SNe Icn (Gal-Yam et al. 2022; Perley et al. 2022; Pellegrino et al. 2022; Gagliano et al. 2022) have been found, showing diverse properties. In some of these cases, a short-lived early blue peak has been observed, possibly consistent with the shock cooling of a low-mass envelope, shock-breakout from a confined shell of CSM, or the subsequent cooling of the shocked material. For example, the SN Ic iPTF15dtg (Taddia et al. 2016) had an early blue peak associated with the cooling envelope of a massive star, as  $M_{\text{ej}} \approx 10 M_{\odot}$  were ejected in the explosion, while other events, such as PTF11mb, developed a longer double-peaked structure (Taddia et al. 2018).

Owing to the absence of He and H in their spectra, SN Ic progenitors have been suggested to lose their envelope prior to explosion, either due to stellar winds (Filippenko 1997, and references therein) or through binary interaction (Podsiadlowski et al. 1992; Yoon et al. 2010; Smith 2014). The presence and distribution of CSM around SESN progenitors, as well as the measurement of progenitor properties from the shock-cooling peak of SNe, can provide vital clues to better understand the yet unknown details of the evolution of massive progenitors of SNe and their explosion mechanism.

Here, we report the early-time detection and extensive follow-up observations of SN 2022oqm, a relatively normal SN Ic with an early-time UV peak as well as

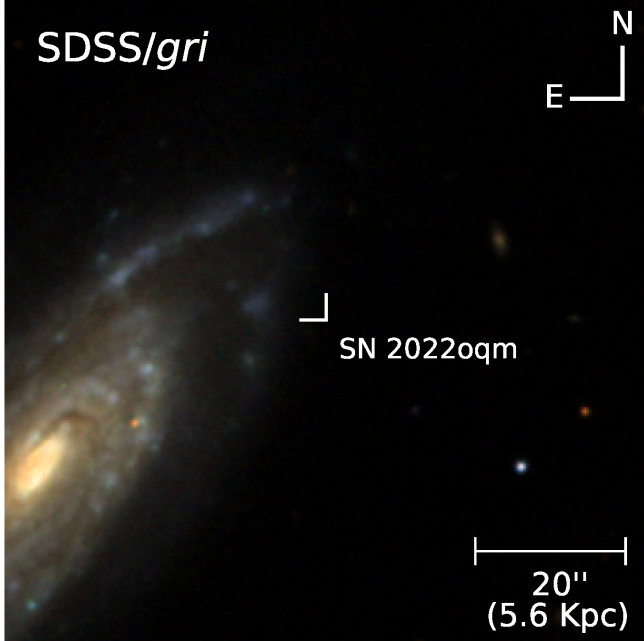


**Figure 1.** The location of SN 2022oqm marked by a white arrow on a false-color SDSS *gri* image of the host galaxy NGC 5875. The SDSS *gri* images were combined using the methods of [Lupton et al. \(2004\)](#).

high-ionization and short-lived C/O lines with  $4000\text{--}5000\text{ km s}^{-1}$  velocities, likely originating in an optically thin CSM surrounding the expanding ejecta. In § 2 we report the discovery of the SN. We describe in § 3 the multiwavelength monitoring campaign of SN 2022oqm and its host galaxy. Section 4 presents an analysis of the spectral and photometric evolution, and we derive basic properties of the explosion such as its blackbody evolution, ejected (and  $^{56}\text{Ni}$ ) mass, and the host-galaxy properties. In § 5, we discuss our findings and propose that the early-time light curve is explained by an initial CSM interaction possibly followed by a brief period of shock-cooling emission. We present possible interpretations for the origin of SN 2022oqm in § 6, and we summarize our findings in § 7.

Throughout the paper we use a  $\Lambda$ CDM cosmological model with  $H_0 = 67.4\text{ km s}^{-1}\text{ Mpc}^{-1}$ ,  $\Omega_M = 0.315$ , and  $\Omega_\Lambda = 0.685$  ([Planck Collaboration et al. 2018](#)).

## 2. Discovery

### 2.1. Supernova Discovery

SN 2022oqm was first detected by the ZTF survey ([Bellm et al. 2019](#); [Graham et al. 2019](#)) at  $\alpha = 15^{\text{h}}09^{\text{m}}08.22^{\text{s}}$ ,  $\delta = +52^\circ 32' 05''.28$  (J2000.0). It was observed on 2022 July 11 at 04:40 (UTC dates are used throughout this paper; JD = 2,459,771.695) with a *g*-band magnitude of  $17.32 \pm 0.04$ , following a nondetection one day prior (JD = 2,459,770.764) with a  $5\sigma$  limit

of  $g = 19.94$  mag, indicating a rise of  $\gtrsim 2.6$  mag in just one day.

The SN was internally designated ZTF22aasxgjp and was reported to the Transient Name Server<sup>1</sup> by a ZTF duty astronomer ([Zimmerman et al. 2022](#)). It was discovered in NGC 5875 with a redshift of  $z = 0.0113$  ([Albareti et al. 2017](#)); its location is shown in Fig. 1.

We adopt a Hubble-flow distance of  $d = 58 \pm 4.1$  Mpc provided by the NASA Extragalactic Database calculator, embedded in the NGC 5875 object page (NED)<sup>2</sup> and corrected for Virgo, Great Attractor, and Shapley supercluster infall ([Mould et al. 2000](#)), corresponding to a distance modulus of  $33.82 \pm 0.15$  mag. This implies that the absolute magnitude of SN 2022oqm at discovery was  $M_g = -16.6 \pm 0.16$  mag (corrected for Galactic reddening; see § 2.3).

Rapid spectroscopic and photometric observations were obtained shortly thereafter, following the methodology of [Gal-Yam et al. \(2011\)](#). Within the first 8 hr, we obtained optical *ugri* photometry and a low-resolution spectrum with the Spectral Energy Distribution Machine (SEDM; [Ben-Ami et al. 2012](#); [Blagorodnova et al. 2018](#)), a spectrum with the Gemini Multi-Object Spectrograph (GMOS; [Hook et al. 2004](#)), and UV photometry using the UV/Optical Telescope (UVOT; [Gehrels et al. 2004](#)) at the Neil Gehrels *Swift* Observatory. The SEDM photometry showed SN 2022oqm to be blue ( $g - r = -0.29$  mag) and rapidly rising, with an additional rise of  $\sim 0.3$  mag over 3 hr (i.e., rising with a rate of  $2.4\text{ mag day}^{-1}$ ). SEDM spectroscopy (resolution  $\mathcal{R} \approx 100$ ) and GMOS ( $\mathcal{R} \approx 1500$ ) spectra revealed highly ionized C IV, O V, and O IV features with velocities of  $\sim 4000\text{ km s}^{-1}$ . UV photometry indicated that SN 2022oqm was bright, with  $M_{\text{UVM2}} = -17.79 \pm 0.15$  mag. Attempts to obtain UV spectra of SN 2022oqm using the *Hubble Space Telescope* (*HST*) and *Swift* UVOT were unsuccessful owing to technical reasons (*HST*) and lack of sufficient signal (*Swift*).

### 2.2. Explosion-Time Estimate

Typically, in order to establish an explosion time using a well-sampled light curve, the flux in a given band can be extrapolated to zero assuming a power-law rise (e.g., [Bruch et al. 2021](#); [Soumagnac et al. 2020](#)).

A potentially superior alternative is possible for objects with spectral energy distributions (SEDs) that are well fit by a blackbody. In such cases, the light-curve behavior in a given band is determined by the radius and temperature evolution. A physically motivated model

<sup>1</sup> <https://www.wis-tns.org/>

<sup>2</sup> <https://ned.ipac.caltech.edu/>

for the rise can thus be acquired from assuming a power-law behavior for the temperature and radius,

$$T_{\text{eff}} = T_0(t - t_0)^\alpha \text{ and } R_{\text{BB}} = R_0(t - t_0)^\beta, \quad (1)$$

where  $T_0$  and  $R_0$  are respectively the temperature and radius at day 1, and  $\alpha$  and  $\beta$  are their corresponding power-law slopes. Using this model, we constrain the rise using all multiband information during the first 2 days. The advantage of this method is its sensitivity to the decline of the UV bands as well as the rise of the optical bands, and the ability to simultaneously utilize all available photometric bands. We discuss the fitting process in detail in § 4.2, and adopt an estimate for the explosion date (JD) of  $t_{\text{exp}} = 2,459,771.2 \pm 0.2$ . Times  $t$  reported hereafter are relative to this date. This estimate is consistent with an explosion time measured using a power-law extrapolation of the  $g$ -band flux to zero.

### 2.3. Extinction

We correct for foreground Galactic reddening using the Schlafly & Finkbeiner (2011) recalibration of the Schlegel et al. (1998) extinction maps. At the location of SN 2022oqm, these imply a reddening of  $E(B - V) = 0.017$  mag, which we correct assuming a Cardelli et al. (1989) extinction law with  $R_V = 3.1$ . To estimate the host-galaxy extinction, we apply the methods of Stritzinger et al. (2018), who found that the variance of the optical colors of SNe Ic is minimal 10 days after maximum brightness. We determine the peak times and colors by fitting a low-order polynomial to a range of 10 days around the respective peak time and 10 days after. We evaluate the  $g - r$  and  $g - i$  color 10 days after the  $g$ -band peak, as well as the  $g - r$  and  $r - i$  colors 10 days after the  $r$ -band peak, and find good agreement with a negligible ( $E(B - V) < 0.02$  mag) amount of host extinction. This conclusion is consistent with the location of the SN at a large offset from its host galaxy (Fig. 1), and with the absence of narrow Na I D doublet in absorption. This line is correlated with dust extinction and reddening (Poznanski et al. 2012), but was not detected in any of our high signal-to-noise-ratio (S/N) spectra. Hence, we do not apply any host extinction correction to our data.

## 3. Observations

All observations are made public via WISEREP (Yaron & Gal-Yam 2012).

### 3.1. Spectroscopy

We obtained 36 epochs of spectroscopy between  $t = 0.6$  days and  $t = 60.1$  days. The details of the observations and reductions for the telescopes used are provided below.

- 8 m Gemini North telescope on Maunakea; 2 epochs. GMOS was used to obtain the data. For each spectrum, four 900 s exposures were obtained in the long-slit mode with the B600 grating ( $\mathcal{R} \approx 1500$ ), and two different central wavelengths of 5200 Å and 5250 Å were adopted to cover the chip gap. The data were reduced using the Gemini IRAF package v. 1.14.<sup>3</sup> The slit was oriented at or near the parallactic angle to minimize slit losses caused by atmospheric dispersion (Filippenko 1982).
- 1.5 m telescope at Palomar Observatory (P60); 16 epochs. Data were acquired with the integral field unit (IFU;  $\mathcal{R} \approx 100$ ) SEDM, and reduced using the automatic SEDM pipeline (Rigault et al. 2019; Kim et al. 2022). The slit was oriented at or near the parallactic angle.
- 2.56 m Nordic Optical Telescope (NOT) at the Observatorio del Roque de los Muchachos on La Palma (Spain); 7 epochs between July 11 and September 8.<sup>4</sup> Low-resolution spectra were obtained with the Alhambra Faint Object Spectrograph and Camera (ALFOSC)<sup>5</sup> with a 1'' wide slit and grism #4 ( $\mathcal{R} = 360$ ), providing a wavelength coverage of 3500–9000 Å. The data were reduced using standard methods with the data-reduction pipelines PyNOT<sup>6</sup> v. 1.0.1 and PypeIt v. 1.8.1 (Prochaska et al. 2020). The slit was oriented at or near the parallactic angle.
- 3 m Shane telescope at Lick Observatory; 7 epochs. We used the Kast double spectrograph (Miller et al. 1988) configured with the 2'' wide slit, the 600/4310 grism, and the 300/7500 grating to obtain a series of 7 optical spectra. This configuration resulted in a spectral resolution of a  $\sim 5$  Å on the blue side ( $\sim 3630$ – $5680$  Å) and  $\sim 12$  Å on the red side ( $\sim 5450$ – $10,740$  Å), corresponding to a resolving power of  $\mathcal{R} \approx 800$  across the observed band. All spectra were obtained at an airmass

<sup>3</sup> <http://www.gemini.edu/observing/phase-iii/understanding-and-processing-data/data-processing-software/gemini-iraf-general>

<sup>4</sup> Program ID 64-501; PI J. Sollerman

<sup>5</sup> <http://www.not.iac.es/instruments/alfosc>

<sup>6</sup> <https://github.com/jkrogager/PyNOT>

less than 1.6 and with the slit was oriented at or near the parallactic angle. Data were reduced (including removal of telluric features) following the approach described by [Silverman et al. \(2012\)](#). At each epoch 3 red side exposures were taken to minimize the effects of cosmic rays. A single blue side exposure was taken with an additional 60s in order to synchronize its readout time with the final red exposure.

- 5 m Hale telescope at Palomar Observatory (P200); 2 epochs. We used the Double Beam Spectrograph (DBSP; [Oke & Gunn 1982](#)). The data were reduced following standard procedures using the P200/DBSP pipeline described by [Roberson et al. \(2022\)](#). The 600/4000 and 316/7500 gratings were used in the blue and red arms, respectively, corresponding to a resolving power of  $\mathcal{R} \approx 1000$  over the observed 3200–10,000 Å bandpass. The slit was oriented at or near the parallactic angle.
- 2.0 m Liverpool Telescope (LT; [Steele et al. 2004](#)); one epoch. The Spectrograph for the Rapid Acquisition of Transients (SPRAT; [Piascik et al. 2014](#)) was used to obtain data, which were reduced using the LT pipeline ([Smith et al. 2016](#)). The blue optimized mode was used, with a central spectral resolution of  $\mathcal{R} = 350$ . The slit was oriented at or near the parallactic angle.
- 10 m Keck I telescope at the W. M. Keck Observatory; 1 epoch. The Low-Resolution Imaging Spectrometer (LRIS; [Oke et al. 1995](#)) was used to acquire a single long-slit spectrum using the 1''0 wide slit oriented at the parallactic angle. The 600/4000 grism and 400/8500 grating were used for the blue and red arms, respectively. This configuration resulted in spectral resolutions of  $\sim 5$  Å on the blue side ( $\sim 3165$ – $5643$  Å) and  $\sim 9$  Å on the red side ( $\sim 5359$ – $10,256$  Å), and a resolving power of  $\mathcal{R} \approx 900$ . Data were reduced using the LPipe automaed pipeline ([Perley 2019](#)).

The details of the spectroscopic observations are listed in [Table 1](#), and the spectra are shown in [Fig. 2](#). All spectra have been calibrated to the Galactic-extinction-corrected ZTF  $g$ ,  $r$ , and  $i$  photometry by scaling the reduced spectrum with a linear function to match the flux obtained from photometry.

### 3.2. Photometry

ZTF photometry in the  $gri$  bands was acquired using the ZTF camera ([Dekany et al. 2020](#)) mounted on

**Table 1.** Summary of Spectroscopic Observations of SN 2022oqm

Start Date (UTC)	Phase (d)	Telescope	Spectrograph	Exp (s)
2022-07-11.31	0.60	P60	SEDM	1800
2022-07-11.42	0.70	Gemini-N	GMOS	3600
2022-07-11.91	1.20	NOT	ALFOSC	1800
2022-07-12.21	1.50	P60	SEDM	1800
2022-07-12.98	2.26	LT	SPRAT	750
2022-07-13.18	2.46	P60	SEDM	1800
2022-07-13.92	3.20	NOT	ALFOSC	1800
2022-07-14.22	3.50	P60	SEDM	1800
2022-07-15.89	5.17	NOT	ALFOSC	600
2022-07-17.18	6.46	P60	SEDM	1800
2022-07-17.99	7.27	NOT	ALFOSC	1800
2022-07-18.18	7.47	P60	SEDM	1800
2022-07-20.18	9.46	P60	SEDM	1800
2022-07-21.23	10.52	Shane	Kast	2160/2100
2022-07-21.27	10.56	Gemini-N	GMOS	1600
2022-07-22.32	11.60	P200	DBSP	300
2022-07-25.30	14.59	Shane	Kast	1860/1800
2022-07-26.17	15.46	P60	SEDM	1800
2022-07-27.24	16.52	P60	SEDM	1800
2022-07-27.93	17.22	NOT	ALFOSC	1200
2022-07-29.20	18.48	Shane	Kast	1860/2100
2022-08-05.19	25.47	Shane	Kast	2460/2400
2022-08-07.16	27.45	P60	SEDM	1800
2022-08-10.19	30.47	P60	SEDM	1800
2022-08-14.16	34.44	P60	SEDM	1800
2022-08-15.88	36.16	NOT	ALFOSC	2400
2022-08-19.16	36.44	P60	SEDM	1800
2022-08-19.24	36.52	Shane	Kast	3360/3300
2022-08-20.26	40.54	P200	DBSP	600
2022-08-22.20	42.49	Shane	Kast	3360/3300
2022-08-28.18	48.47	P60	SEDM	2250
2022-08-29.16	49.44	P60	SEDM	2250
2022-09-01.14	52.43	P60	SEDM	2250
2022-09-04.21	55.49	Shane	Kast	3360/3300
2022-09-08.85	60.14	NOT	ALFOSC	3600
2022-09-23.24	74.53	Keck	LRIS	1200

the 48 inch (1.2 m) Samuel Oschin Telescope at Palomar Observatory (P48). These data were processed using the ZTF Science Data System (ZSDS; [Masci et al. 2019](#)). Light curves were obtained using the ZTF forced-photometry service<sup>7</sup> on difference images produced using the optimal image subtraction algorithm of [Zackay et al. \(2016\)](#) at the position of the SN, calculated from the median ZTF alert locations to lie at  $\alpha = 15^{\text{hr}}09^{\text{m}}08.213^{\text{s}}$ ,  $\delta = +52^{\circ}32'05''.17$  (J2000.0). We

<sup>7</sup> See [ztf.forced\\_photometry.pdf](#) under <https://irsa.ipac.caltech.edu/data/ZTF/docs>

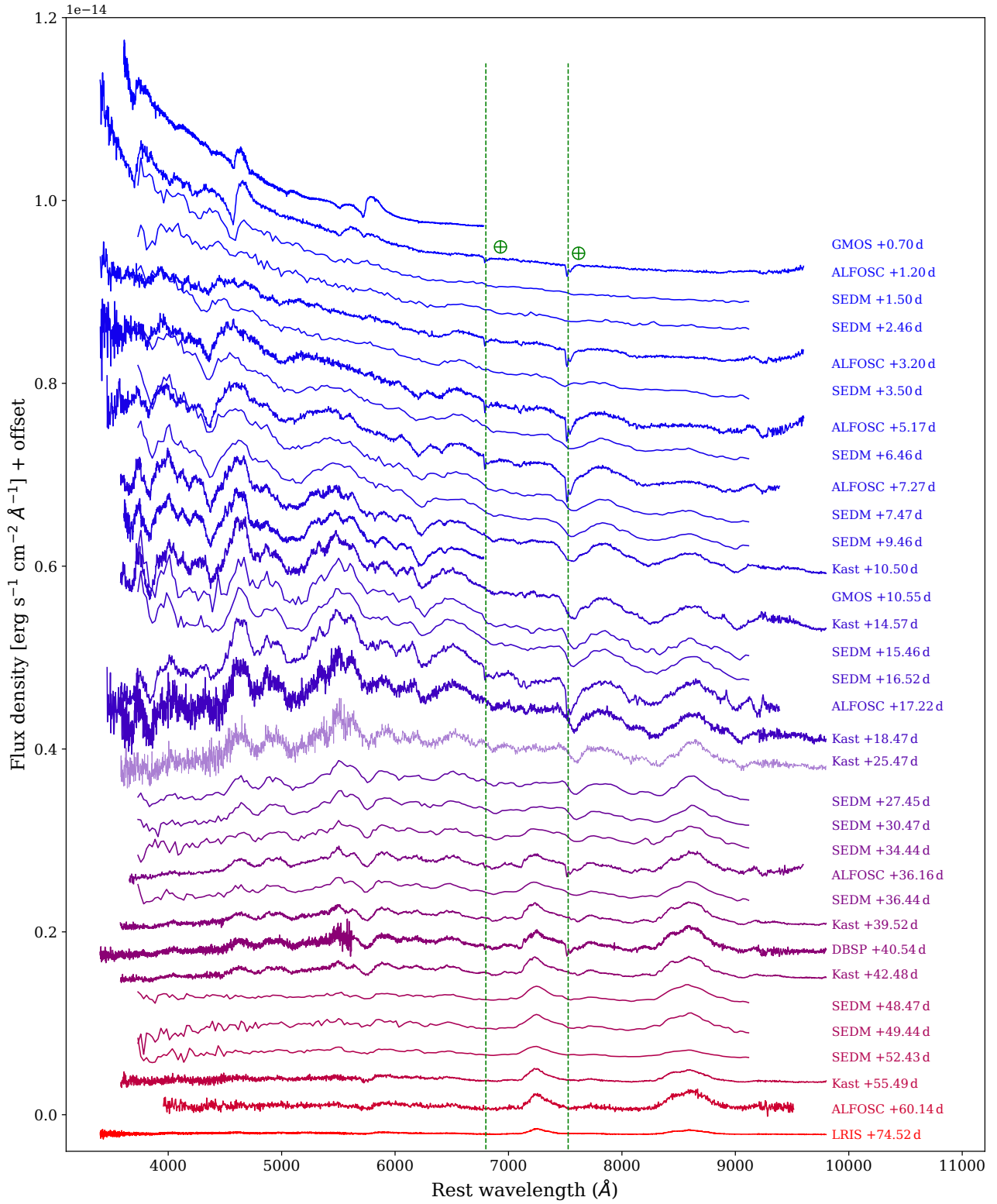


**Figure 2.** Spectral evolution of SN 2022oqm. The phases are reported relative to the estimated explosion time of JD = 2,459,771.217. The locations of telluric features are marked with vertical green dashed lines.

removed images that have flagged difference images, bad pixels close to the SN position, a large standard deviation in the background region, or a seeing of more than  $4''$ . We performed a baseline correction to ensure the mean of the pre-SN flux is zero. We report detections above a  $3\sigma$  threshold, and  $5\sigma$  nondetections. These data are provided in Table 2.

In addition to the ZTF photometry, we triggered an extensive photometric follow-up campaign using the following telescopes.

- The UV-Optical Telescope (UVOT) onboard the *Neil Gehrels Swift Observatory* (Gehrels et al. 2004; Roming et al. 2005). The images were reduced using the *Swift* HEASOFT<sup>8</sup> toolset. Individual exposures comprising a single epoch were summed using `uvotimsum`. Source counts were then extracted using `uvotsource` from the summed images using a  $5''$  circular aperture. The background was estimated from several larger regions surrounding the host galaxy. These counts were then converted to fluxes using the photometric zero points of Breeveld et al. (2011) with the latest calibration files from September 2020. We did not attempt to subtract the host flux at the location of the SN. This is justified, as the field was observed before the SN exploded in the *UVW1* and *U* bands, revealing no underlying sources. This is also corroborated by archival Legacy Survey images (Dey et al. 2019) from the Beijing-Arizona Sky Survey fields (Zou et al. 2017), and by deep PS1 imaging (Flewelling et al. 2020). We used the *Swift* pre-SN images in the *UVW1* and *U* bands, and the surrounding host flux in the *UVW2*, *UVM2*, *B*, and *V* bands, and estimate the host contribution to the SN flux as negligible in all bands for all of the epochs presented in this paper.
- The Optical Imager (IO:O) at the 2.0 m robotic LT the Observatorio del Roque de los Muchachos. We used the *u*, *g*, *r*, *i*, and *z* filters. Images were reduced using the IO:O automatic pipeline; image subtraction versus Pan-STARRS (*g*, *r*, *i*, *z*) or SDSS (*u*) reference imaging was performed with a custom IDL routine. Aperture photometry was conducted on the subtracted image using SDSS secondary standards.
- The Rainbow Camera (Blagorodnova et al. 2018) on the Palomar 60 inch (1.52 m) telescope (P60;

Cenko et al. 2006). Reductions were performed using the automatic pipeline described by Fremming et al. (2016).

- The 0.75 m Katzman Automatic Imaging Telescope (KAIT) and the 1.0 m Nickel telescope at Lick Observatory. The data were reduced using a custom pipeline<sup>9</sup> presented by Stahl et al. (2019). No image-subtraction procedure was applied (see above for *Swift*), and the Pan-STARRS1<sup>10</sup> catalog was used for calibration. Point-spread-function (PSF) photometry was obtained using DAOPHOT (Stetson 1987) from the IDL Astronomy User’s Library<sup>11</sup>. Apparent magnitudes were all measured in the KAIT4/Nickel2 natural system, and then transformed back to the standard system using local calibrators and color terms for KAIT4 and Nickel2 (Stahl et al. 2019).
- The 6.5 m MMT equipped with the Magellan infrared spectrograph (MMIRS) at the Fred Lawrence Whipple Observatory. We acquired 1 epoch of *JHK<sub>s</sub>* imaging with  $90''$  dithers between different exposures. The images were reduced by customized scripts within IRAF which include dark subtraction, sky subtraction, and coaddition of multiple exposures. Instrumental magnitudes of all stars in the imaging field with  $S/N > 5$  were obtained with PSF photometry using IRAF task *daophot*, and the zero point was obtained by calibrating the instrumental magnitudes to the 2MASS catalog (Skrutskie et al. 2006).

The resulting light curves appear in Fig. 3. Some cross-instrument differences between the *Swift*/UVOT and the KAIT and Nickel *V*-band photometry remain, so we apply a  $-0.18$  mag offset for clarity to the *Swift*/UVOT *V*-band photometry to align these data in all figures where the light curves appear. The offset is not applied in our analysis, and applying it does would change any of the results.

### 3.3. X-ray Follow-up Observations

While monitoring SN 2022oqm with UVOT, *Swift* also observed the field between 0.3 and 10 keV with its on-board X-ray telescope (XRT) in photon-counting mode (Burrows et al. 2005). We analyzed these data with the online tools provided by the UK *Swift* team<sup>12</sup> that use

<sup>8</sup> <https://heasarc.gsfc.nasa.gov/docs/software/heasoft/> v. 6.26.1.

<sup>9</sup> <https://github.com/benstahl92/LOSSPhotPypeline>

<sup>10</sup> <http://archive.stsci.edu/panstarrs/search.php>

<sup>11</sup> <http://idlastro.gsfc.nasa.gov/>

<sup>12</sup> [https://www.swift.ac.uk/user\\_objects](https://www.swift.ac.uk/user_objects)

**Table 2.** Log of photometric observations (truncated)

JD	$t$ [rest-frame days]	Instrument	Filter	AB Magnitude
2459771.7	0.47	P48/ZTF	$g$	$17.23 \pm 0.02$
2459771.81	1.47	P60/SEDM	$r$	$17.34 \pm 0.02$
2459771.83	1.51	P60/SEDM	$g$	$17.03 \pm 0.03$
2459771.84	1.53	P60/SEDM	$r$	$17.35 \pm 0.02$
2459771.84	2.53	P60/SEDM	$i$	$17.66 \pm 0.03$
2459772.04	3.44	Swift/UVOT	$W1$	$16.04 \pm 0.04$
2459772.04	3.51	Swift/UVOT	$U$	$16.26 \pm 0.04$
2459772.04	3.58	Swift/UVOT	$B$	$16.47 \pm 0.06$
2459772.04	4.47	Swift/UVOT	$W2$	$15.88 \pm 0.03$
2459772.05	5.46	Swift/UVOT	$V$	$16.85 \pm 0.11$
2459772.05	5.5	Swift/UVOT	$M2$	$15.88 \pm 0.03$
2459772.39	5.54	LT/IO:O	$g$	$16.91 \pm 0.08$
2459772.39	8.43	LT/IO:O	$r$	$17.17 \pm 0.05$
2459772.39	8.51	LT/IO:O	$i$	$17.51 \pm 0.07$
2459772.39	10.43	LT/IO:O	$u$	$16.62 \pm 0.06$
2459772.39	11.37	LT/IO:O	$z$	$17.78 \pm 0.09$

<sup>a</sup> All measurements are reported in the AB system and are corrected for Galactic line-of-sight reddening.

<sup>b</sup> The full table is made available electronically on WISeREP.

the methods described by Evans et al. (2007, 2009) and the software package HEASoft v. 6.29.

SN 2022oqm evaded detection at all epochs ( $N = 16$ , between  $t = 0.8$  and  $t = 16$  days). The median  $3\sigma$  count (ct)-rate limit of each observing block is  $0.006 \text{ ct s}^{-1}$  (0.3–10 keV). Stacking all data lowers the upper limit to  $0.0004 \text{ ct s}^{-1}$ . Assuming a Galactic neutral hydrogen column density of  $n(H) = 1.73 \times 10^{20} \text{ cm}^{-2}$  (HI4PI Collaboration et al. 2016) and a power-law spectrum with a photon index of 2, the count rates correspond to an unabsorbed flux limit of  $2.2 \times 10^{-13}$  (the median luminosity of the unbinned data) and  $1.5 \times 10^{-14} \text{ erg cm}^{-2} \text{ s}^{-1}$  (binned over all epochs) in the 0.3–10 keV bandpass. At the distance of SN 2022oqm this corresponds to luminosity  $L_X < 8.7 \times 10^{40} \text{ erg s}^{-1}$  (unbinned) and  $L_X < 6.2 \times 10^{39} \text{ erg s}^{-1}$  (binned) in the range 0.3–10 keV.

### 3.4. Search for Prediscovery Emission

Many SNe with spectroscopic and photometric signatures of CSM show prediscovery emission in the weeks, months, or years before the explosion. While in most cases prediscovery emission has been detected for SNe IIn (e.g., Fraser et al. 2013; Mauerhan et al. 2013; Ofek et al. 2013; Pastorello et al. 2013; Margutti et al. 2013; Strotjohann et al. 2021), precursors have also been detected for SNe Ibn (Pastorello et al. 2007; Foley et al. 2007), SNe Ic-BL (Corsi et al. 2014; Ho et al. 2019), and possibly for a SN IIB (Strotjohann et al. 2015). Here, we check for prediscovery emission for SN 2022oqm.

The ZTF survey first started monitoring the position of SN 2022oqm 4.3 yr before the SN explosion and we

obtain a forced-photometry light curve for all difference images available at IPAC<sup>13</sup> following the methods described by Strotjohann et al. (2021). We discard 5.8% of the observations because they have either flagged difference images, bad pixels close to the SN position, a large standard deviation in the background region, or a seeing disk  $> 4''$ . After these quality cuts, we are left with a total of 2329 pre-SN observations during 658 different nights. We perform a baseline correction and verify that the error bars are large enough to account for random scatter before the SN explosion. Next, we bin the light curve using a variety of bin sizes (1, 3, 7, 15, 30, and 90-day-long bins) owing to the unknown outburst duration and search the unbinned and binned light curves for  $5\sigma$  detections before the SN explosion.

We do not detect any pre-SN outbursts and here present limits for 7-day-long bins. We correct for the Galactic foreground extinction of  $E(B - V) = 0.017 \text{ mag}$  and adopt a distance modulus of 33.8 mag. The median limiting magnitude is  $-12.9 \text{ mag}$  in the  $g$  and  $r$  bands, and  $-13.9 \text{ mag}$  in the  $i$  band. ZTF  $i$ -band observations are generally less constraining owing to the reduced sensitivity of the CCD and because fewer observations are obtained in this band. Eruptions that are brighter than  $-13 \text{ mag}$  in the  $r$  band and last for at least a week can be excluded during 78 weeks (84 weeks for the  $g$  band); this corresponds to 35% of the time during the 4.3 yr before the explosion. In the last 3 months

<sup>13</sup> <https://irsa.ipac.caltech.edu/applications/ztf/>



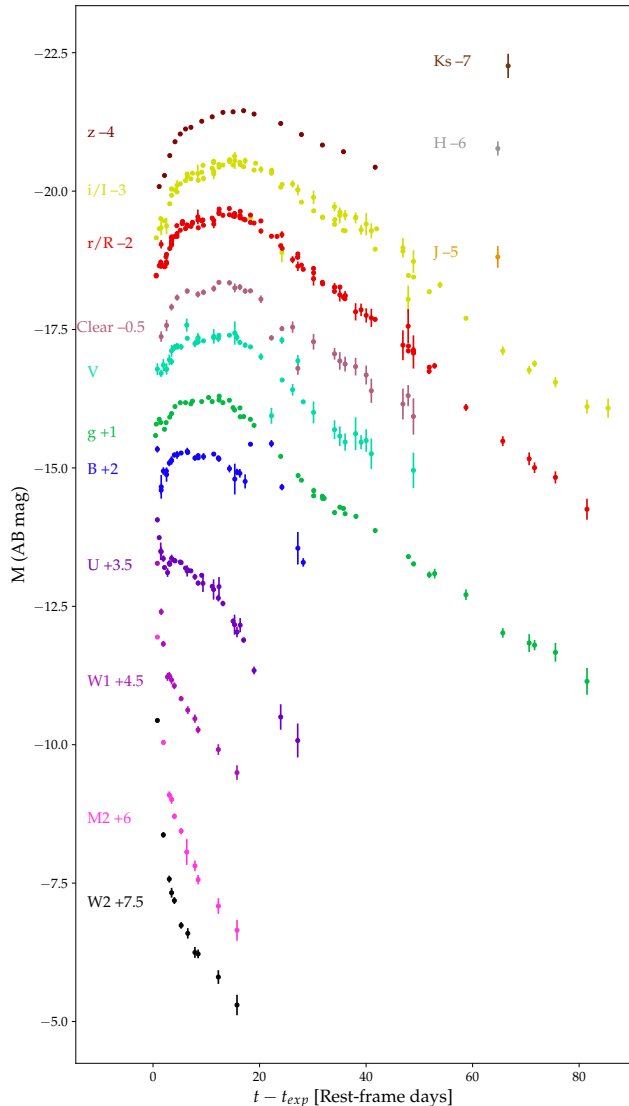


**Figure 3.** The UV-optical and NIR light curves of SN 2022oqm. Note the early blue peak, most notable in the  $u$  and  $g$  bands.

before the SN explosion, the position was mostly observed in the  $i$  band and the absolute magnitude limits in this time window are shown in Fig. 4. During this time we can exclude week-long precursor eruptions that are brighter than  $-14$  mag in the  $i$  band. This rules out our bright precursors, in the range observed for strongly interacting SNe IIn and SNe Ibn, which typically reach  $M_r \approx -14$  mag, and can occasionally reach  $-17$  mag (Strotjohann et al. 2021, and references therein).

## 4. Analysis

### 4.1. Spectral Analysis

We use the parameterized supernova synthetic-spectrum SYNOW code (Branch et al. 2005) in order to

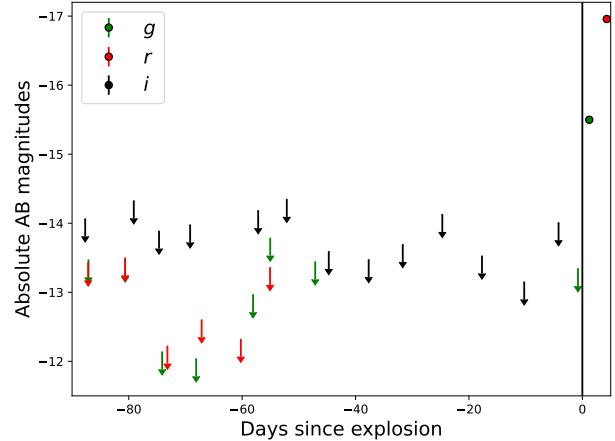


**Figure 4.** Light curve in 7-day bins for the last 100 days before the SN explosion. Arrows mark  $5\sigma$  upper limits in the ZTF  $g$ ,  $r$ , and  $i$  bands. No predisccovery emission is detected at the SN site throughout the ZTF survey.

interpret the  $t = 0.7$  d GMOS spectrum, chosen since it is the earliest high-resolution spectrum. Using this approach, a blackbody is first fit to the continuum. A spherical expansion velocity is assumed and various ions are added in order to match the lines. Owing to the simplifying underlying assumptions of the SYNOW approach (e.g., spherical, homologous expansion, and resonant-scattering line formation above a sharp blackbody-spectrum-emitting photosphere), this modeling can only be used to identify and verify the prominent line features, but not to assess physical parameters such as elemental abundances or relative mass fractions. We therefore also avoid performing any fine tuning of the different ion parameters.

We display three possible fits in Fig. 5, with an increasing amount of lines matched by the fit. The fits are obtained for an expansion velocity of  $4000 \text{ km s}^{-1}$  and for a blackbody temperature of  $40,000 \pm 10,000 \text{ K}$ . In the first panel, we acquire a good match for all features  $\gtrsim 4300 \text{ \AA}$  by high-ionization lines of pure carbon and oxygen (C IV and O V). In the second panel, the overplotted yellow fit shows that the dip around  $4070 \text{ \AA}$  is likely O V  $\lambda 4124$ . However, forming this feature in SYNOW requires the assumption of a higher specific excitation temperature value for this ion, leading to an overshoot in the strengths of the additional O V absorption around  $5040 \text{ \AA}$  and  $5500 \text{ \AA}$ . This is not surprising given the limitations of the code; overall, the identification of O V with multiple observed features seems secure. The third panel includes O IV, which serves mainly to explain the dip on the blue edge — the strong O IV  $\lambda\lambda 3726, 3729$  lines (blueshifted by  $\sim 4000 \text{ km s}^{-1}$ ). O IV also contributes to the C IV feature around  $4600 \text{ \AA}$

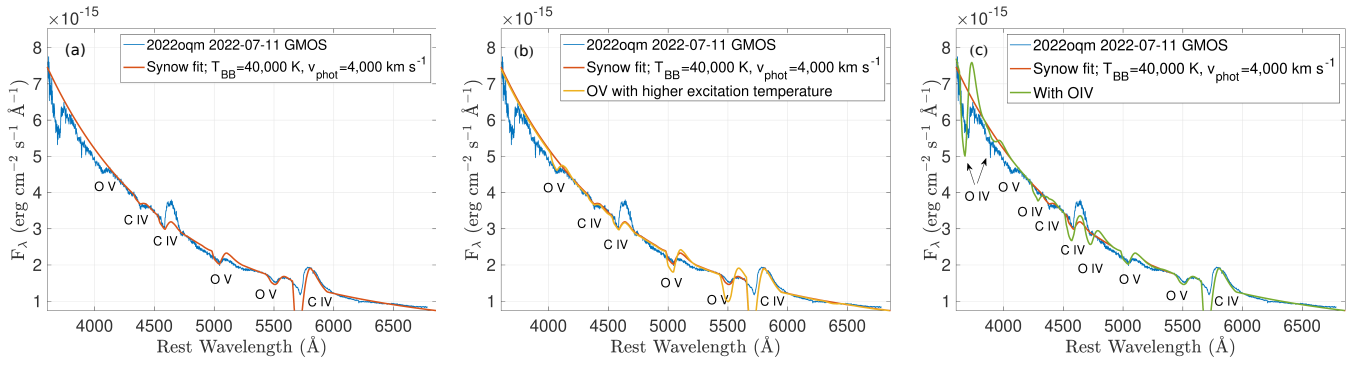


**Figure 5.** SYNOW fits to the first high-spectral resolution spectrum (GMOS;  $t = 0.7$  d). All fits assume a 40,000 K continuum and an expansion velocity of  $4000 \text{ km s}^{-1}$ . (a) C IV and O V using the default parameters of SYNOW. (b) The same as (a) but with a higher specific excitation temperature for O V. (c) The same as (a), but also including O IV.

and creates additional dips that explain weak features in the spectrum, suggesting the likely existence of O IV. We note that the  $\lambda\lambda 3726, 3729$  lines are also associated with [O II] transitions, but this interpretation is disfavored owing to the multiple other high-ionization features, and the low density associated with [O II] transitions. Also, while the feature at  $\sim 4600 \text{ \AA}$  is close to the He II  $\lambda 4686$  line, associating the two would place the maximum absorption of the feature at  $\sim 7000 \text{ km s}^{-1}$ , which is inconsistent with the other features in the spectrum. This would not match the emission peak, missing it by  $\sim 3000 \text{ km s}^{-1}$ . Similarly, associating the  $5800 \text{ \AA}$  feature with He I  $\lambda 5876$  requires an expansion velocity of  $8000 \text{ km s}^{-1}$ , and it would place the peak emission  $\sim 4500 \text{ km s}^{-1}$  from the line rest wavelength. A C/O composition is favored, requiring a single expansion velocity and better matching the peak emission in all lines.

Figure 6 shows the early-time spectral evolution of SN 2022oqm at subsequent epochs. The high-ionization C/O features observed in the first spectrum evolve into lower-ionization features over the first 3 days. In the second epoch, these features widen to a velocity of  $5500 \text{ km s}^{-1}$ , measured from peak emission to absorption. By  $t = 3.2$  days, all features broaden to a line velocity of  $\sim 10,000 \text{ km s}^{-1}$ . This evolution can be seen in the inset of Fig. 6.

While the absorption minima of the early-time spectra have velocities of  $4000 \text{ km s}^{-1}$  and  $5500 \text{ km s}^{-1}$  for the first and second epochs (respectively), the blue edge of the absorption reaches SN-ejecta-like velocities of  $\sim 12,000 \text{ km s}^{-1}$  in the first epoch and extends out to  $\sim 15,000 \text{ km s}^{-1}$  in the second epoch. It is well known for W-R stars that the asymptotic wind velocity is typically only measured in strong UV resonance lines. Indeed, Perley et al. (2022) show that in the early-time spectra of SN 2021csp, a SN Icn with a C/O expanding CSM (indicated by the narrow  $\sim 2000 \text{ km s}^{-1}$  features in its early spectrum), the blue edge of the optical C

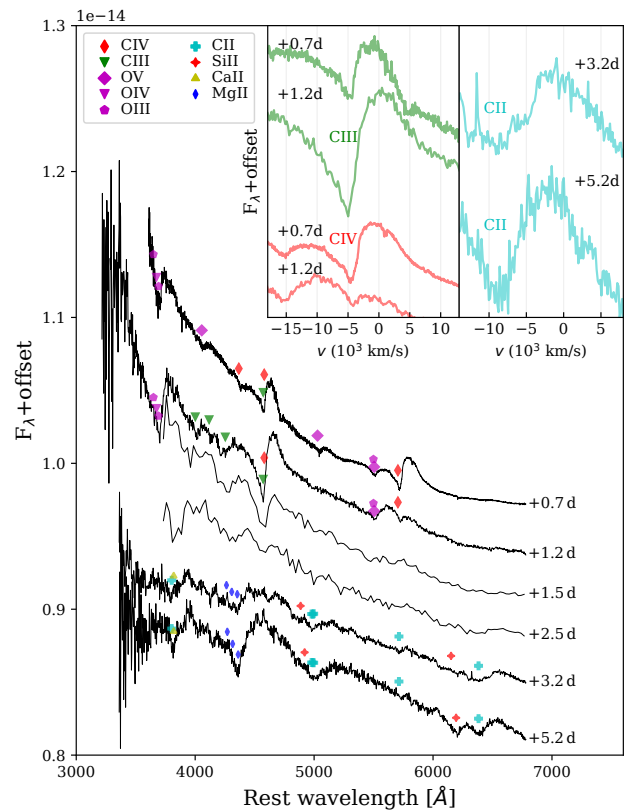


**Figure 6.** Early-time spectra of SN 2022oqm. The main panel shows the spectral evolution in the first few days, and the inset shows a zoom-in view of the C IV  $\lambda\lambda 5801, 5812$ , C III  $\lambda\lambda 4647, 4650$ , and C II  $\lambda 6578$  features. At  $t < 3$  d, the spectrum is dominated by C/O high-ionization features with  $4000\text{--}5000 \text{ km s}^{-1}$  velocities. After  $t = 3$  d, the spectrum develops low-ionization absorption features with  $\sim 10,000 \text{ km s}^{-1}$  velocities.

features is at lower velocities by a factor of 1.5 compared with those measured for UV C lines. Applying such a correction factor to our data would imply a velocity dis-

tribution extending to  $\sim 20,000 \text{ km s}^{-1}$  for the features in the early spectra. However, the emission maximum is much less extended, at  $v = 5000 \text{ km s}^{-1}$ .

During its photospheric phase, SN 2022oqm develops typical SN Ic features — namely Si II  $\lambda 6355$ , O I  $\lambda 7774$ , Ca II  $\lambda\lambda 3934, 3969$ , Ca II  $\lambda\lambda\lambda 8498, 8542, 8662$ , and Mg II  $\lambda 4481$ , as well as a prominent Na I  $\lambda\lambda 5890, 5896$ . As the evolution progresses, the spectrum develops Fe absorption features and unusually strong Ca II and later also [Ca II] emission. This suggests a Ca-rich SN Ic classification is appropriate for SN 2022oqm.

By the time it becomes partially nebular at  $t = 60$  days, the spectrum is dominated by the Ca emission features on the red side, with Fe II absorption upon an elevated continuum on the blue side as well as a Na I  $\lambda\lambda 5890, 5896$  P Cygni profile. There is no detectable  $\lambda\lambda 6300, 6364$  [O I] emission during the early nebular phase, indicating that SN 2022oqm falls into the category of “Ca-rich SNe” (Filippenko et al. 2003; Perets et al. 2010). To place an upper limit on the [O I] emission, we assume it accounts for all the luminosity in a region surrounding the line with a similar velocity to the [Ca II] feature, and find that  $L_{[\text{O I}]} < 1.1 \times 10^{37} \text{ erg s}^{-1}$  and that the flux ratio  $[\text{Ca II}]/[\text{O I}] > 4$ . Since the  $[\text{Ca II}]/[\text{O I}]$  ratio can be time variable, De et al. (2020) used a criterion of  $[\text{Ca II}]/[\text{O I}] > 2$  for a single phase to ensure good separation of Ca-rich events at all phases. To extract the velocity of the Ca II  $\lambda\lambda 7291, 7324$  feature, we fit the velocity profile of Ca II  $\lambda\lambda 7291, 7324$  with a Gaussian model. We adopt an average wavelength of 7307.5 for the reference wavelength, and fit two individual components with the same width, height, and offset. Our best-fit model had a full width at half-maximum intensity (FWHM) of  $6900 \text{ km s}^{-1}$  (velocity of a single component) and a blueshift of  $\Delta v = 1700 \text{ km s}^{-1}$ . Thus, in addition to its unusual strength, the [Ca II] feature has an FWHM at the high end of the SN Ic distribution (Prentice et al. 2022).

#### 4.2. Blackbody Evolution

We linearly interpolate the UV-optical light curves of SN 2022oqm to the times of UV observations and construct an SED. Using the `Scipy curve_fit` package, we fit this SED to a Planck function and recover the evolution of the blackbody temperature, radius, and luminosity parameters  $T_{\text{eff}}$ ,  $R_{\text{BB}}$ , and  $L_{\text{BB}}$ , respectively. In order to have  $\chi^2_\nu$  close to 1, we assume a 0.1 mag systematic error in addition to the statistical errors. This systematic error should account for both cross-calibration errors between different instruments and intrinsic deviations from a perfect blackbody. The fit results are shown in Fig. 7 (a-c), and the SED fits are displayed in

Fig. A4. In addition to the best-fit blackbody luminosity, we calculate a pseudobolometric luminosity: we perform a trapezoidal integration of the interpolated SED and extrapolate it to the UV and infrared (IR) using the blackbody parameters. Both estimates are consistent within the uncertainty for all times. However, as strong emission lines develop in the spectrum, the continuum contribution decreases, and as the peak of the SED moves to the IR, the blackbody extrapolation is less reliable. This is likely more significant at  $t > 40$  days when the spectrum is dominated by strong Ca II lines and the directly observed luminosity accounts for only 30% of the implied total luminosity.

At the latest epoch ( $t = 66$  days), we also include  $JHK_s$  near-infrared (NIR) photometry in our fits. We find poor agreement between the full SED and a single blackbody. However, the  $JHK_s$  bands alone are well fit with a blackbody at  $\sim 1650 \text{ K}$  and a radius of  $4.4 \times 10^{15} \text{ cm}$ , which is  $\sim 80\%$  of the radius of freely expanding ejecta at  $10,000 \text{ km s}^{-1}$ . We show the results of this fit in Fig. A1. This NIR emission could be explained by the onset of dust formation within the ejecta around this time. Alternatively, it could be a result of strong nebular lines forming in the IR. For this epoch, we extrapolate the pseudobolometric luminosities by fitting the  $JHK_s$  bands, and extrapolating only to the IR. The blackbody fit parameters and pseudobolometric luminosities are given in Table 3.

We find that the early-time light-curve behavior is fully explained by the blackbody evolution. During the first 2.5 days, the temperature cools rapidly, with a best-fitting power law of  $\sim t^{-1}$ . During this time the UV emission declines rapidly, with the  $UVW2$  light curve falling by  $1.5 \text{ mag day}^{-1}$ . After day 3, the temperature evolution slows down, and the  $UVW2$  light-curve decline rate slows down by an order of magnitude. At early times, the photospheric radius is well described by an approximate free expansion,  $R_{\text{BB}} \propto vt$ , with  $v = 20,000 \text{ km s}^{-1}$ , which slows down significantly after  $\sim 3.5$  days. To check if the early light-curve behavior is fully explained by a cooling and expanding blackbody, we use an empirical light-curve model: we assume that  $T_{\text{eff}}$  and  $R_{\text{BB}}$  evolve according to

$$T_{\text{eff}} = \begin{cases} T_0(t - t_0)^\alpha & (t - t_0) < t_{\text{br}}, \\ T_{02}(t - t_0)^{\alpha_2} & (t - t_0) > t_{\text{br}}, \end{cases} \quad (2)$$

$$R_{\text{BB}} = \begin{cases} R_0(t - t_0)^\beta & (t - t_0) < t_{\text{br},2}, \\ R_{02}(t - t_0)^{\beta_2} & (t - t_0) > t_{\text{br},2}. \end{cases} \quad (3)$$

Here the variables are defined in a way similar to that of Eq. 1. This phenomenological model has 9 free pa-

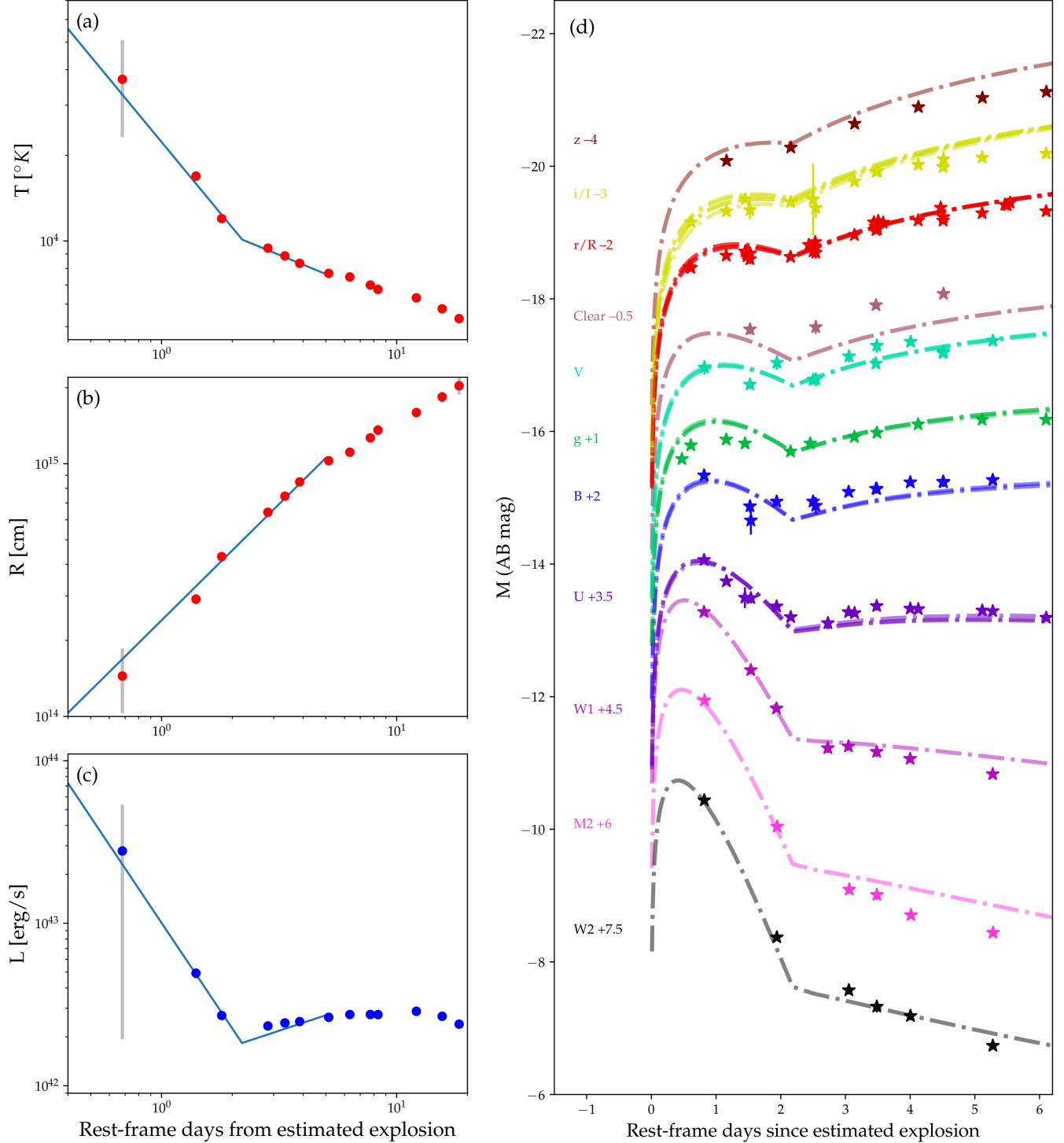


**Figure 7.** (Blackbody evolution of SN2022oqm. Data points are calculated by interpolating the SED at the times of UV photometry. The solid lines show the best-fit broken power law to the light curves. The blackbody evolution shows a dramatic transformation at  $t \approx 2.5$  d, characterized by a temperature break at  $t_{\text{br}} = 2.2$  days from a rapid  $\sim t^{-1}$  temperature decline to a slower  $\sim t^{-0.3}$  evolution (a), while maintaining a smooth rise in radius (b) with a corresponding impact on the bolometric luminosity (c). (d) shows the corresponding light-curve fits of SN 2022oqm to a broken temperature and radius power-law evolution model. The break in temperature evolution at  $t_{\text{br}} = 2.2$  naturally accounts for the rapid rise and early peak.

parameters:  $T_0$ ,  $R_0$ ,  $\alpha$ ,  $\beta$ ,  $\alpha_2$ ,  $\beta_2$ ,  $t_{\text{br}}$ ,  $t_{\text{br},2}$ , and  $t_0$ , where  $T_{02}$  and  $R_{02}$  are calculated by demanding continuity at the power-law break. Given a set of parameters and the subsequent blackbody evolution, we generate light curves using

$$f_\nu(t) = 4\pi^2 R_{\text{BB}}^2 B_\nu(T_{\text{eff}}(t)) \quad (4)$$

which we fit to the SN light curves by integrating the SED adopting each filter transmission curve. The fits are performed until  $t = 5$  d, before significant features develop in the spectra. Our best-fit light-curve model is shown in Fig. 7, and the corresponding blackbody power laws are plotted in Fig. 7. We find that a cooling blackbody with  $T_{\text{eff}} = (22,000 \text{ K})((t - t_0)/\text{d})^{-1}$  and  $R_{\text{BB}} = (2.7 \times 10^{14} \text{ cm})((t - t_0)/\text{d})^{0.9}$  can explain the full early light-curve behavior, up to  $t = 3$  d. The break in the temperature evolution to  $\alpha_2 = -0.3$  naturally accounts for the first peak and the subsequent slowing in light-curve evolution in the blue bands. Table 4 shows the best-fit parameters and their respective uncertainties.

#### 4.3. Light-Curve Evolution

The early-time light-curve evolution of SN 2022oqm is characterized by a rapid decline in the UV (e.g., the *UVW2* light curve drops by  $1.5 \text{ mag day}^{-1}$ ), an early peak in the blue (*u* and *g* bands), and a rise in the red and IR bands. The UV decline slows after  $t > 3$  days, as explained above.

At later times ( $t > 10$  days), the light curve is well described by the radioactive decay of  $^{56}\text{Ni}$  diffusing from the inner part of the ejecta (Arnett 1982). We fit the model of Inserra et al. (2013) to the bolometric light curves up to  $t = 40$  days (after which we consider the bolometric luminosity unreliable), starting from the second peak in the bolometric light curve at  $t \approx 12$  days:

$$\frac{L_{\text{SN}}(t)}{10^{43} \text{ erg s}^{-1}} = e^{-(t/\tau_m)^2} \int_0^{t/\tau_m} P(t') 2 \left( \frac{t'}{\tau_m} \right) e^{(t'/\tau_m)^2} \frac{dt'}{\tau_m}, \quad (5)$$

where  $P(t)$  is the  $^{56}\text{Ni}$  decay energy and  $\tau_m$  is the diffusion timescale parameter,

$$\tau_m = 10.0 \left( \frac{\kappa}{0.1 \text{ cm}^2 \text{ g}^{-1}} \right)^{0.5} \left( \frac{M_{\text{ej}}}{M_\odot} \right)^{\frac{3}{4}} \left( \frac{E_{\text{kin}}}{10^{51} \text{ erg}} \right)^{-\frac{1}{4}} \text{ day}, \quad (6)$$

where  $\kappa$  is the ejecta opacity,  $M_{\text{ej}}$  is the ejected mass, and  $E_{\text{kin}}$  is the kinetic energy of the ejecta. Here we adopt the following energy-deposition rate  $Q_\gamma$  for

$^{56}\text{Ni} \rightarrow ^{56}\text{Co} \rightarrow ^{56}\text{Fe}$  decay (Swartz et al. 1995; Junde 1999) corresponding to a  $^{56}\text{Ni}$  mass  $M_{\text{Ni}}$ :

$$\frac{Q_\gamma(t)}{10^{43} \text{ erg s}^{-1}} = \frac{M_{\text{Ni}}}{M_\odot} \left[ 1.38 e^{\frac{-t}{111.4\text{d}}} + 6.54 e^{\frac{-t}{8.8\text{d}}} \right], \quad (7)$$

$$\frac{Q_{\text{pos}}(t)}{10^{41} \text{ erg s}^{-1}} = \frac{M_{\text{Ni}}}{M_\odot} 4.64 \left[ e^{\frac{-t}{111.4\text{d}}} - e^{\frac{-t}{8.8\text{d}}} \right], \quad (8)$$

$$P = Q_\gamma f_{\text{dep}} + Q_{\text{pos}}, \quad (9)$$

where  $f_{\text{dep}}$  is the fraction of deposited energy due to  $\gamma$ -ray escape,

$$f_{\text{dep}} = 1 - \exp(-t_\gamma^2/t^2). \quad (10)$$

Until  $t = 50$  days, the bolometric light curve is well described ( $\chi^2/\text{dof} = 0.7$ ) by a model with a  $^{56}\text{Ni}$  mass of  $M_{\text{Ni}} = 0.106 \pm 0.001 M_\odot$ , a diffusion timescale  $\tau_m = 10 \pm 0.38$  days, and a  $\gamma$ -ray escape time of  $t_\gamma = 36.0 \pm 0.8$  days. We note that this fit accounts only for statistical uncertainties, and the errors on these parameters are therefore probably underestimated. After  $t = 50$  days, the estimated bolometric luminosity declines sharply, but this is likely due to the underestimation of the IR flux owing to the lack of IR observations. This is illustrated during the last epoch at  $t = 66$  days, where IR data have been obtained and the pseudobolometric luminosity is calculated using the *griJHK<sub>s</sub>* bands. An extrapolation based on the blackbody fit to the *JHK<sub>s</sub>* bands recovers 65% of the missing luminosity compared to the Ni fit. Given the partial coverage of the SED, we consider it likely that the luminosity continues to follow the Ni model.

Assuming  $v_{\text{ej}} = 10,000 \text{ km s}^{-1}$  (appropriate for the bulk of the mass) and  $\kappa = 0.07 \text{ cm}^2 \text{ g}^{-1}$  as used by Barbarino et al. (2021), we acquire from  $\tau_m$  an estimate of  $M_{\text{ej}} = 1.1 \pm 0.04 M_\odot$ , and a kinetic energy of  $E_{\text{kin}} = 6.6 \times 10^{50} \text{ erg}$ .<sup>14</sup> Fitting of the  $t < 50$  days light curve using the methods of Sharon & Kushnir (2020) yields  $M_{\text{Ni}} = 0.113_{-0.001}^{+0.002} M_\odot$  and  $t_\gamma = 36 \pm 2$  days, in good agreement with the parameters derived using Eq. (5). Figure 8 shows the best-fit model to the late-time bolometric light curve. While  $^{56}\text{Ni}$  decay can account for the late-time behavior of the light curve, an additional powering mechanism is required to explain the early-time luminosity. The inferred  $^{56}\text{Ni}$  mass, kinetic energy, and ejected mass are within the distribution of values found for SNe Ic by Barbarino et al. (2021)

<sup>14</sup> We note that assuming a higher typical ejecta velocity, as suggested by the early radius evolution and the nebular [Ca II] FWHM, could result in a higher estimate for  $M_{\text{ej}}$ . For example, if  $15,000 \text{ km s}^{-1}$  is assumed,  $M_{\text{ej}}$  would be  $1.7 M_\odot$ .

**Table 3.** Blackbody evolution of SN 2022oqm

JD	t [rest-frame days]	T <sub>eff</sub> [°K]	R <sub>BB</sub> [10 <sup>14</sup> cm]	L <sub>BB</sub> [10 <sup>42</sup> erg s <sup>-1</sup> ]	L <sub>pseudo</sub> [10 <sup>42</sup> erg s <sup>-1</sup> ]	L <sub>pseudo,extrap</sub> [10 <sup>42</sup> erg s <sup>-1</sup> ]	χ <sup>2</sup> /dof
2459772.04	0.82	37000 ± 13800	1.44 ± 0.41	27.83 ± 25.9	3.02 ± 3.02	28.28 ± 23.51	10.6
2459772.77	1.54	16900 ± 700	2.91 ± 0.14	4.93 ± 0.37	2.91 ± 2.91	4.88 ± 0.15	3.94
2459773.18	1.94	12000 ± 200	4.29 ± 0.11	2.7 ± 0.07	2.19 ± 2.19	2.79 ± 0.02	1.71
2459774.22	2.97	9400 ± 200	6.43 ± 0.2	2.33 ± 0.06	2.01 ± 2.01	2.44 ± 0.01	2.61
2459774.74	3.48	8900 ± 200	7.44 ± 0.27	2.43 ± 0.07	2.13 ± 2.13	2.59 ± 0.01	3.57
2459775.27	4.0	8300 ± 200	8.48 ± 0.35	2.48 ± 0.08	2.17 ± 2.17	2.66 ± 0.02	6.01
2459776.55	5.28	7700 ± 100	10.28 ± 0.41	2.64 ± 0.08	2.23 ± 2.23	2.8 ± 0.02	5.8
2459777.75	6.46	7500 ± 100	11.11 ± 0.47	2.74 ± 0.08	2.26 ± 2.26	2.89 ± 0.02	4.88
2459779.17	7.87	7000 ± 100	12.66 ± 0.53	2.74 ± 0.09	2.15 ± 2.15	2.84 ± 0.02	5.23
2459779.78	8.47	6800 ± 100	13.59 ± 0.67	2.74 ± 0.11	2.11 ± 2.11	2.84 ± 0.03	8.16
2459783.62	12.27	6300 ± 100	15.95 ± 0.7	2.87 ± 0.09	2.13 ± 2.13	2.99 ± 0.03	6.11
2459787.15	15.75	5800 ± 100	18.38 ± 0.92	2.68 ± 0.1	1.84 ± 1.84	2.78 ± 0.03	5.43
2459790.0	18.57	5300 ± 200	20.35 ± 1.51	2.39 ± 0.11	1.43 ± 1.43	2.49 ± 0.05	8.23
2459793.0	21.54	5200 ± 200	20.31 ± 1.5	2.07 ± 0.09	1.18 ± 1.18	2.13 ± 0.04	6.47
2459796.0	24.51	5200 ± 200	18.09 ± 1.23	1.69 ± 0.06	0.94 ± 0.94	1.72 ± 0.03	4.04
2459799.0	27.47	4900 ± 100	18.5 ± 1.22	1.4 ± 0.05	0.69 ± 0.69	1.45 ± 0.03	3.0
2459802.0	30.44	4700 ± 100	18.88 ± 1.25	1.19 ± 0.04	0.54 ± 0.54	1.24 ± 0.03	2.83
2459805.0	33.41	4600 ± 100	18.16 ± 1.21	1.02 ± 0.04	0.45 ± 0.45	1.05 ± 0.02	2.73
2459807.0	35.38	4600 ± 100	17.01 ± 0.98	0.91 ± 0.03	0.39 ± 0.39	0.93 ± 0.02	2.06
2459809.0	37.36	4600 ± 100	16.26 ± 1.01	0.83 ± 0.03	0.36 ± 0.36	0.85 ± 0.02	2.32
2459813.0	41.32	4500 ± 100	15.01 ± 1.07	0.68 ± 0.03	0.28 ± 0.28	0.68 ± 0.02	2.5
2459817.0	45.27	4600 ± 200	12.74 ± 1.13	0.52 ± 0.03	0.19 ± 0.19	0.53 ± 0.02	2.04
2459820.0	48.24	4600 ± 200	11.26 ± 1.04	0.41 ± 0.02	0.16 ± 0.16	0.42 ± 0.01	1.99
2459824.0	52.19	4600 ± 200	9.43 ± 1.1	0.29 ± 0.02	0.09 ± 0.09	0.29 ± 0.01	2.23
2459837.5	65.54	1650 ± 20	44.4 ± 1.3	0.1 ± 0.002	0.09 ± 0.002	0.17 ± 0.01	0.2

<sup>a</sup> A 0.1 mag systematic error was assumed when performing the fits.

<sup>b</sup> After  $t = 40$  days, we consider the blackbody fits and extrapolation to the IR and UV as unreliable, since the spectrum becomes line-dominated. We report the values here for completeness.

<sup>c</sup> The last epoch is fit only to the *JHK*, but integrated using all observed bands, as discussed in the text.

Rodríguez et al. (2022), with the ejecta mass lying toward the low end of the mass distribution. A rough order-of-magnitude estimate for the  $\gamma$ -ray escape time  $t_\gamma$  and the diffusion time  $\tau_m$  comes from demanding an optical depth of unity for  $\gamma$ -ray escape, and a dynamical timescale for the diffusion of order  $c/v$ . This implies a ratio of  $\frac{t_\gamma}{t_{\text{diff}}} \approx \sqrt{\left(\frac{c}{v}\right) \frac{\kappa_\gamma}{\kappa_{\text{opt}}}} \approx 3.3$ , in good agreement with our findings. An order-of-magnitude estimate for the values of these timescales  $t_\gamma \approx \sqrt{\frac{3\kappa_\gamma M}{4\pi v^2}} \approx 50$  days and  $t_{\text{diff}} \approx \sqrt{\frac{3\kappa_{\text{opt}} M}{4\pi v c}} \approx 14$  days is also consistent with our fit results. The  $\gamma$ -ray escape time of SN 2022oqm is short for a typical SN Ic, compared to the typical  $t_\gamma \approx 100$  days found by Sharon & Kushnir (2020). In their recent work, Sharon & Kushnir (2023) measure the  $\gamma$ -ray deposition history for five Ca-rich SNe Ib, and find that they have both low <sup>56</sup>Ni masses (0.01–0.05  $M_\odot$ ), and  $t_\gamma$  in the 30–70 day range. Compared with the Ca-rich SN Ib population, SN 2022oqm has a higher <sup>56</sup>Ni mass, but a similar  $t_\gamma$ , placing it closer to the SN Ia population in this parameter space.

#### 4.4. Host-Galaxy Properties

SN 2022oqm exploded at a distance of 16.6 kpc (59′.3) from the center of the spiral galaxy NGC 5875 (Fig. 1). To measure the galaxy properties, we retrieved science-ready stacked images from the *Galaxy Evolution Explorer* (*GALEX*) general release 6/7 (Martin et al. 2005), the Sloan Digital Sky Survey data release 9 (SDSS DR9; Ahn et al. 2012), the Panoramic Survey Telescope and Rapid Response System (Pan-STARRS, PS1) DR1 (Chambers et al. 2016), and *WISE* (Wright et al. 2010) images from the unWISE archive (Lang 2014).<sup>15</sup> We measured the brightness of the host using LAMBDA<sup>16</sup> (Lambda Adaptive Multi-Band Deblending Algorithm in R; Wright et al. 2016) and the methods described by Schulze et al. (2021). In short, these involve the removal of contaminating foreground sources, identifying an appropriate aperture, and using it to extract photometry simultaneously from all available bands. The photome-

<sup>15</sup> <http://unwise.me>

<sup>16</sup> <https://github.com/AngusWright/LAMBDA>

**Table 4.** Power law fits for the early blackbody evolution SN 2022oqm

$T_0$ [°K]	$R_0$ [ $10^{14}$ cm]	$\alpha$	$\beta$	$t_{exp}$ [JD]	$t_{br}$ [rest days]	$\alpha_2$
$22000 \pm 4000$	$2.7^{+0.5}_{-1.4}$	$-1.0^{+0.1}_{-0.2}$	$0.9^{+0.3}_{-0.1}$	$2459771.2^{+0.2}_{-0.2}$	$2.2^{+0.2}_{-0.3}$	$-0.3^{+0.1}_{-0.1}$

<sup>a</sup> A 0.1 mag systematic error was assumed when performing the fits.

<sup>b</sup> In our best fit,  $\beta_2 = \beta$ . Thus, we do not report  $\beta_2$  or  $t_{br,2}$

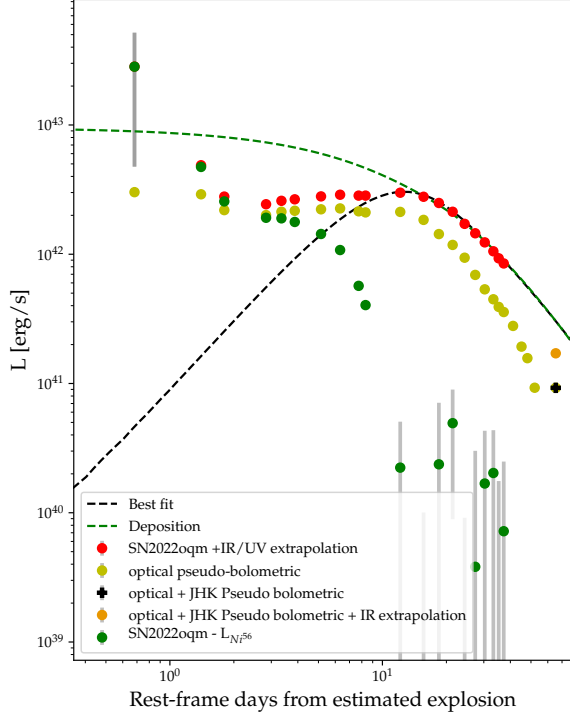


**Figure 8.** A bolometric light-curve fit to an Arnett model. The best-fit model is the black dashed curve. The red data points are the integrated observed luminosity with blackbody extrapolation corrections for the UV and IR, and the green points are the difference between these two. The yellow points are the integrated luminosities with no UV/IR corrections (pseudobolometric). Note that these diverge from the bolometric data as the IR corrections become more important at late times. The black “plus sign” is the integrated luminosity including the late-time *griJHK<sub>s</sub>* bands, and the orange point is this luminosity including an IR extrapolation correction based on the *JHK<sub>s</sub>* blackbody fits, as described in the text. We do not fit an optical blackbody to this epoch for a UV component, since the optical SED is dominated by emission lines

try is summarized in Table 5. We find a half-light radius of  $r_{50} = 21''.4$  (6 kpc) in the SDSS *r* band, which places

**Table 5.** Photometry of the host galaxy of SN 2022oqm

Survey	Filter	Brightness [AB mag]
<i>GALEX</i>	<i>FUV</i>	$15.79 \pm 0.03$
<i>GALEX</i>	<i>NUV</i>	$15.25 \pm 0.02$
SDSS	<i>u</i>	$14.09 \pm 0.04$
SDSS	<i>g</i>	$12.90 \pm 0.04$
SDSS	<i>r</i>	$12.29 \pm 0.03$
SDSS	<i>i</i>	$11.96 \pm 0.04$
SDSS	<i>z</i>	$11.73 \pm 0.03$
Pan-STARRS	<i>g</i>	$12.90 \pm 0.03$
Pan-STARRS	<i>r</i>	$12.29 \pm 0.02$
Pan-STARRS	<i>i</i>	$12.05 \pm 0.01$
Pan-STARRS	<i>z</i>	$11.90 \pm 0.03$
Pan-STARRS	<i>y</i>	$11.69 \pm 0.08$
<i>WISE</i>	<i>W1</i>	$11.99 \pm 0.01$
<i>WISE</i>	<i>W2</i>	$12.52 \pm 0.02$

NOTE—All measurements are reported in the AB system and not corrected for reddening.

SN 2022oqm at an offset of  $2.8 r_{50}$  from the center of its host galaxy.

The SED was modelled with the software package *prospector* (Johnson et al. 2021), as described in detail by Schulze et al. (2021). We assumed a Chabrier initial mass function (IMF; Chabrier 2003) and approximated the star-formation history (SFH) by a linearly increasing SFH at early times followed by an exponential decline at late times (functional form  $t \times \exp(-t/\tau)$ ). The model includes an extinction correction using the Calzetti et al. (2000) model. We use the dynamic sampling package *dynesty* (Speagle 2020) to sample the posterior probability distribution and extract the median host-galaxy properties.

The host is a fairly massive ( $\log_{10}(M/M_{\odot}) \approx 10.66^{+0.10}_{-0.31}$ ) star-forming galaxy (star-formation rate  $\text{SFR} = 3.52^{+1.17}_{-0.72} M_{\odot} \text{ yr}^{-1}$ ) with moderate extinction ( $E(B-V)_{\text{star}} = 0.24^{+0.04}_{-0.03}$  mag). The mass and the SFR are within the distributions measured for host galaxies of SNe Ic from the PTF survey (Schulze et al. 2021). Although the SN is located in the outskirts of its host (Fig. 1), the location is not unusual for SNe Ic explod-

ing in galaxies of similar mass (Schulze et al. 2021). Our spectroscopic observations sampled different regions of the host galaxy. However, none of the slit alignments of our GMOS or NOT spectra showed any prominent H II region emission at a distance  $\lesssim 3$  kpc along the slit, so we cannot constrain the metallicity or the SFR in the direct vicinity of SN 2022oqm. In Fig. A3 we show the NOT and GMOS slit orientations, as well as the surroundings of the explosion site. Since our spectroscopic observations did not cover all nearby regions, we cannot rule out the presence of a nearby star-forming region. The most nearby well-defined star-forming region is 3.8 kpc southeast of the SN explosion site. We measure the line fluxes of prominent emission lines ([O III]  $\lambda\lambda 4959, 5007$ , H $\alpha$ , H $\beta$ , and [N II]  $\lambda 6584$ ), finding values of  $1.4 \pm 0.2$ ,  $1.6 \pm 0.2$ ,  $5.6 \pm 0.6$ , and  $1.9 \pm 0.3$  in units of  $10^{-15} \text{ erg s}^{-1} \text{ cm}^{-2}$ , respectively (calibrated to PS1  $r$ -band photometry). Using the O3N2 and R3 strong-line metallicity indicators and the calibrations of Curti et al. (2017), we infer a metallicity of  $0.88^{+0.10}_{-0.11}$  solar for this region. This value is near the average for the explosion-site metallicity in the sample of Galbany et al. (2018).

A visual inspection of deep stacks from the Beijing-Arizona Sky Survey (BASS; Dey et al. 2019) and GALEX show no point source or elevated extended emission in the vicinity of the SN. BASS has a median point-source limit of  $r = 23.6$  mag, implying  $M_r \gtrsim -10$  mag or an optical surface brightness limit of  $\sim 23.5 \text{ mag arcsec}^{-2}$ . The GALEX all-sky survey has a limit of  $\text{NUV} = 20.5$  mag, implying a region with  $M_{\text{NUV}} \gtrsim -13$  mag or with a UV surface brightness of  $\sim 24 \text{ mag arcsec}^{-2}$  can still exist in the vicinity of the SN, corresponding to a point-source SFR limit of  $\Sigma_{\text{SFR}} = 0.01 M_{\odot} \text{ yr}^{-1}$  (Salim et al. 2007). Since many H II regions have a lower average SFR (Relaño & Kenicutt 2009), this does not rule out an H II region below the GALEX detection limit.

## 5. Discussion

We presented extensive UV-optical observations of SN 2022oqm in § 3, as well as our X-ray limits and observations of the SN host galaxy. In § 4, we analyzed these observations. We showed that the early-time spectra of SN 2022oqm are well explained by an expanding C/O shell moving at  $4000 \text{ km s}^{-1}$ , with line velocities increasing to typical SN ejecta velocities by day 3. At the same time, the blackbody evolution transitions from a rapid cooling and a decline in the bolometric luminosity, to a slower evolution in both parameters. This transition is reflected by a double peak in the optical light curve, and a shift from a fast to slow decline in the UV bands. Fol-

lowing this transition, the spectrum evolves like those of spectroscopically normal (but relatively fast-rising) SNe Ic, until it becomes nebular at  $t \approx 60$  days.

The nebular spectrum has strong [Ca II] and Ca II emission, with no detectable [O I], indicating that the object is Ca-rich. We fit the late-time post-peak ( $t > 12$  days) light curve to a  $^{56}\text{Ni}$ -decay model and find typical SN Ic values of  $M_{\text{ej}} = 1.1 M_{\odot}$ ,  $M_{\text{Ni}} = 0.12 M_{\odot}$ , and  $E_{\text{kin}} = 6.6 \times 10^{50} \text{ erg}$  (e.g., Barbarino et al. 2021). We analyze the host-galaxy observations and find that it is a typical star-forming and massive spiral galaxy. However, the explosion site is more than 3 kpc away from the nearest obvious star-forming region, and offset by 16 kpc from the center of light of its host. In the following, we discuss the implications of our observations on the powering mechanism of the early-time light curve and on the progenitor star of SN 2022oqm.

### 5.1. The Early-Time Features

At early times, the spectra of SN 2022oqm show high-ionization C and O features with absorption minima at velocities of  $\sim 4000\text{--}5500 \text{ km s}^{-1}$ , and a blue edge of  $12,000\text{--}15,000 \text{ km s}^{-1}$ , which (as discussed in § 4.1) could indicate a maximal expansion velocity of  $18,000\text{--}22,000 \text{ km s}^{-1}$  as would have been measured in the UV. At the same time, we observe that the photospheric radius is expanding at  $> 20,000 \text{ km s}^{-1}$ . Later in the evolution, the absorption minima and blue edge accelerate significantly, to absorption minima of  $10,000 \text{ km s}^{-1}$  at  $t = 3.2$  day. It is difficult to fully explain this evolution as being due to the ejecta alone, as it would require non-homologous expansion (slow above fast), or with CSM alone, as the blue edge has ejecta-like high velocities.

The absorption minimum at  $\sim 4000\text{--}5500 \text{ km s}^{-1}$  implies that the photosphere is expanding behind an optically thin line-forming region, itself expanding at a lower velocity. The simplest interpretation is that the lines originate from an expanding shell of CSM surrounding the progenitor star, in addition to a weaker absorption component by the ejecta extending to the photospheric velocity.

An expansion velocity of  $4000 \text{ km s}^{-1}$  is consistent with a continuous wind around a W-R progenitor star (Nugis & Lamers 2000), with the escape velocity of a white dwarf (WD), or with a late-stage eruption resulting from a deposition of energy deep under the stellar surface (Matsumoto & Metzger 2022). An eruptive mass-loss episode occurring days to weeks before the explosion is often seen in other types of SNe. Such eruptions typically lack spectroscopic observations to constrain the ejected CSM velocity (Ofek et al. 2013,



2014b; Strotjohann et al. 2015, 2021; Jacobson-Galán et al. 2022b).

A distribution of expansion velocities in the CSM could explain the apparent line acceleration between the first ( $t = 0.7$  days) and second ( $t = 1.2$  days) spectra. First, the ejecta sweep up the slower CSM (at  $4000 \text{ km s}^{-1}$ ), and later they reach the faster material at  $5500 \text{ km s}^{-1}$ , which accounts for the observed shift of the absorption minimum to higher velocities. As more and more material is accelerated to ejecta velocities, the blue edge of the absorption features becomes more pronounced and extends to higher velocities.

The high velocity could also be explained by radiative acceleration of the optically thin material above the photosphere, by the free-streaming photons from the luminous underlying ejecta. The velocity gain of an optically thin shell of material above a source with integrated luminosity  $E_{\text{rad}}(t)$  at radius  $r_{\text{CSM}}$  is given by

$$\frac{v_{\text{rad}}(t)}{\text{km s}^{-1}} = 1000 \left( \frac{E_{\text{rad}}(t)}{10^{48} \text{ erg}} \right) \left( \frac{\kappa_{\text{fw}}}{10 \text{ cm}^2 \text{ g}^{-1}} \right) \left( \frac{r_{\text{CSM}}}{5 \times 10^{14} \text{ cm}} \right)^{-2}, \quad (11)$$

where  $\kappa_{\text{fw}}(t) = \int \kappa_{\nu} f_{\nu}(t) d\nu / \int f_{\nu}(t) d\nu$  is the flux-weighted opacity (applicable at  $\tau_{\text{diff}} < 1$ ), and  $f_{\nu}$  is the spectral flux density. Scattering opacity alone ( $\sim 0.2 \text{ cm}^2 \text{ g}^{-1}$ ) is not sufficient to accelerate material to the observed velocities, or to explain the acceleration observed in the first few spectra. However, a high effective cross-section due to bound-free and bound-bound processes on the order of  $\gtrsim 10 \text{ cm}^2 \text{ g}^{-1}$  is achievable with an illuminating blackbody spectrum at  $T \gtrsim 10,000 \text{ K}$ , producing a large fraction of photons with energies  $\gtrsim 10 \text{ eV}$ . It can also be achieved with a mild X-ray flux of  $\sim 1\%$  of the UV-optical luminosity, absorbed through photoionization in the CSM, and consistent with the highly ionized species observed during the first three days. We thus consider radiative acceleration as a plausible mechanism for explaining the initially high observed velocities and the acceleration between epochs. As we do not know the exact conditions in the CSM, we refrain from making an explicit calculation, leaving this for future work.

Another explanation for the early emission is from an optically thick shell surrounding the ejecta. Soumagnac et al. (2019) show that breakout from an aspherical shell of CSM could form an increasing photospheric radius, with no actual expansion taking place. In this type of scenario, the expansion is unrelated to the ejecta velocity, but a result of breakout from an increasingly large region. In § 5.3.3 we show that the amount of mass required to make this material optically thick is inconsistent with the integrated luminosity, dis-

favoring this interpretation. In the absence of optically thick material which can facilitate a radiation-mediated shock, temporally-resolved acceleration of the CSM by the shock over a timescale of a few days can be ruled out. The shocks in such systems should be collisionless and would accelerate the material on very short ( $\sim 1 \text{ m}$ ) length scales (Katz et al. 2012), directly to the ejecta velocity seen at  $t > 3$  days.

Here we do not discuss other, more complicated asymmetric configurations. However, such a scenario would have to produce significant absorption at  $\sim 4000 \text{ km s}^{-1}$ . This is a challenge to line-of-sight-based interpretations, such as bipolar outflows, that can explain the slower components with material moving nearly perpendicular to our line of sight. Such models will have a hard time creating significant absorption at low velocities; the obscuring material needs to be placed in front of most of the emitting material. From this point, we assume that a spherical, slowly expanding CSM is the source of the  $4000\text{--}5000 \text{ km s}^{-1}$  features.

## 5.2. Comparison with Other Supernovae

We compare the spectra, light curves, and blackbody evolution of SN 2022oqm with those of other SNe Ic, Icn, and Ic-BL having extensive UV and optical observations at early times, and that either were suggested to have some amount of CSM around their progenitor star, or exhibit an early UV-optical peak. In order to contrast SN 2022oqm with typical SNe Ic, which usually lack early UV observations, we show a comparison with SN 2020scb, a normal SN Ic detected by ZTF with good constraints on its explosion time and early UV observations (Dahiwalé & Fremling 2020). For the sake of uniformity, UVOT and ZTF (if used) light curves were re-reduced using the methods described in § 3, and the blackbody fits are performed with the methods described in § 4.

In Fig. 9, we show a comparison of the early-time  $r$ ,  $u/U$ , and  $UVW1$  light curves of these SNe with SN 2022oqm. While the diversity in absolute magnitude is large, SN 2022oqm is similar to SN 2020bvc (Izzo et al. 2020; Ho et al. 2020a), SN 2006aj (Campana et al. 2006), SN 2014ft (De et al. 2018), and SN 2020oi (Horesh et al. 2020; Rho et al. 2021) in showing an early peak in the UV light curves and later rising to a second peak. In contrast to these, SN 2020scb (this work), SN 2018gep (Ho et al. 2019), SN 2019hgp (Gal-Yam et al. 2022), and SN 2021csp (Perley et al. 2022) display a different behavior consistent with a single-peaked light curve. In Fig. 10, we compare the  $r/R$ -band light curves of SN 2022oqm to SN 2007gr, SN 2020oi, SN 2020bvc, SN 2014ft,

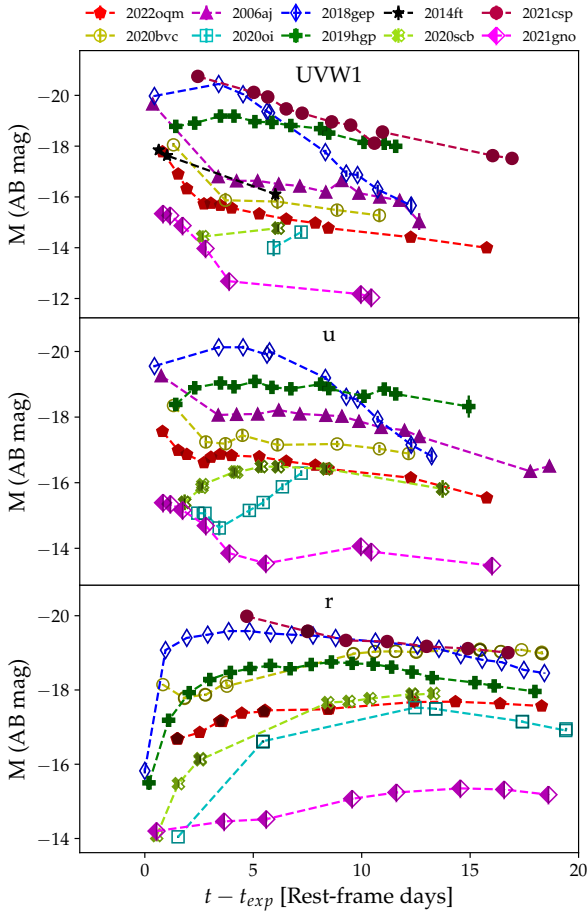


**Figure 9.** The early light-curve evolution of SN 2022oqm (filled pentagons) compared to that of several SNe Ic, Ic-BL, and Ic<sub>n</sub> in the  $r$ ,  $u$ , and  $UVW1$  bands. Several other SNe show a break in their UV light curves, combined with a fast rise in their optical light curve.

SN 2012hn, SN 2019ehk, SN 2021gno (Jacobson-Galán et al. 2022a) and SN 2020scb (a) relative to peak and (b) in absolute magnitude. SN 2022oqm shows a fast rise to peak, to an elevated emission unseen in other comparison objects. Initially it declines at a comparable rate to SN 2021gno, but this changes at  $t \approx 35$  days ( $\sim 20$  days after peak), as the ejecta become transparent to gamma rays.

Figure 11 illustrates a comparison of the blackbody evolution of these SNe with that of SN 2022oqm. In Fig. 12, we normalize the temperature evolution to an arbitrary time and temperature, selected to emphasise a transition in the temperature power-law slope (if such a transition exists). Similarly to SN 2022oqm, other SNe with an early peak in their light curve show a transi-

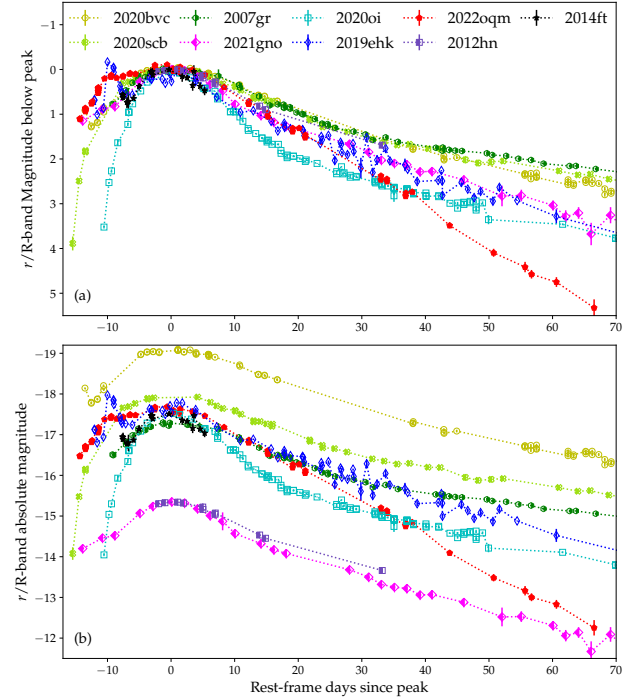


**Figure 10.** A comparison of the  $r/R$ -band light curves of SN 2022oqm to SN 2007gr (Ic), SN 2020oi (Ic), SN 2020bvc (Ic-BL), SN 2014ft (US-Ic), SN 2012hn (Ca-Ic), SN 2021gno (Ca-Ib), SN 2019ehk (Ca-IIb), and SN 2020scb (Ic). We show the light curve (a) relative to the  $r/R$  peak and (b) in absolute magnitude. SN 2022oqm shows an emission excess before peak, and then declines faster than other SNe Ic.

tion from a steep to a shallow power-law evolution. A steep temperature power law also provides a reasonable explanation for the fast rise, as the peak of the SED will move into the UV and optical bands faster than for a typical SN.

Figure 13 shows a spectral comparison of selected objects with SN 2022oqm. In the upper panel, two spectra of SN 2022oqm at +0.7 day and +1.2 day after the explosion are compared to the ultrastripped Type Ic SN 2014ft (De et al. 2018), the broad-line Type Ic SN 2018gep (Ho et al. 2019), and SN 2020bvc (Izzo et al. 2020; Ho et al. 2020a). Although the spectra of SN 2014ft have lower signal-to-noise ratios, they closely resemble those of SN 2022oqm; the prominent features match well with the C/O-dominated line profiles in SN 2022oqm, suggesting a similar origin for the early-time spectroscopic features of SN 2014ft.

In the photospheric phase, the spectra of SN 2022oqm look quite similar to typical SNe Ic such as SN 2007gr (Valenti et al. 2008; Hunter et al. 2009), as shown in the middle panel of Fig. 13. SN 2007gr was a carbon-rich SN Ic with C II  $\lambda\lambda 6580, 7234$  clearly detected in the premaximum spectra (Valenti et al. 2008). The C II

$\lambda\lambda 6580, 7234$  lines are likewise detected in SN 2022oqm. As shown in the bottom panel, the (early) nebular-phase spectra of SN 2022oqm exhibit both a strong Ca II NIR triplet and the forbidden [Ca II]  $\lambda\lambda 7291, 7324$ , but no clear detection of [O I]  $\lambda\lambda 6300, 6363$ , similar to SN 2014ft. The strong emission of [Ca II] compared to [O I] means that SN 2022oqm belongs to the population of “Ca-rich” SNe such as SN 2019ehk (Jacobson-Galán et al. 2020; De et al. 2021) and SN 2012hn (Valenti et al. 2014). We note that the [Ca II]  $\lambda\lambda 7291, 7234$  lines in the +60.1 d spectrum of SN 2022oqm are blueshifted by  $\sim 1700 \text{ km s}^{-1}$ , which was also shown for SN 2014ft (+36.5 d;  $\sim 2500 \text{ km s}^{-1}$ ) and SN 2012hn (+31.0 d;  $\sim 1300 \text{ km s}^{-1}$ ), indicating that those spectra may not be fully nebular in the red side of the spectrum. At this phase, the blue side of the spectrum shows an elevated continuum and a P Cygni profile at  $\sim 5900 \text{ \AA}$ . This feature can either be associated with the Na I  $\lambda\lambda 5890, 5896$  doublet, or with He I  $\lambda 5876$ . The latter is disfavored owing to the lack of stronger features at 6678 and 7065  $\text{\AA}$  (Gal-Yam 2017).

As mentioned in § 4.2, at  $t = 66$  days,  $\sim 75\%$  of the bolometric luminosity is observed in the NIR. This could be explained either by strong emission lines, or a blackbody component with 1650 K and a radius of  $4.4 \times 10^{15} \text{ cm}$ , in reasonable agreement with free expansion at  $10,000 \text{ km s}^{-1}$  for the duration of the SN. The NIR  $V - H$  color at this time ( $V - H \approx 3 \text{ mag}$  in the Vega system) is quite high compared to most of the 64 SESNe observed by Bianco et al. (2014, compare to their Fig. 13) during their entire evolution, and consistent with those of SN 2006jc (Pastorello et al. 2007; Foley et al. 2007) at a similar phase. One possible explanation would be dust formation, observed in some SNe Ic as early as day 60 (Rho et al. 2021). This would be consistent with the observed nebular Ca II and [Ca II] asymmetry toward the blue side, possibly due to the obscuration of the most redshifted parts of the ejecta.

### 5.3. Early-Time Powering Mechanism

While  $^{56}\text{Ni}$  provides a good mechanism for powering the second peak, it cannot explain the early-time contribution to the light curve. We integrate the difference between the bolometric light curve and the best-fit  $^{56}\text{Ni}$  model for all observed times and find  $E = 2.1 \times 10^{48} \text{ erg}$  radiated by an early-time additional component. There are several possible origins for this component:

1. shock cooling of a low-mass envelope;
2. CSM interaction; and
3. shock breakout in extended CSM.

We examine each of these possibilities in light of the observed properties of SN 2022oqm.

#### 5.3.1. Shock Cooling at Early and Intermediate Times

The good agreement of the spectral energy distribution with a blackbody spectrum (Fig. A4) motivates the possibility of shock-cooling powering some or all of the early light curve, prior to  $^{56}\text{Ni}$  decay. During the first 3 days, as we show in § 4.2, the temperature declines with a power law slope of  $T \approx t^{-1}$ , significantly more steeply than the expected  $T \approx t^{-0.5}$  for shock-cooling (Rabinak & Waxman 2011; Nakar & Sari 2010; Piro 2015). It is possible to achieve a sharp temperature decline with existing models, assuming a low-mass envelope (Piro et al. 2021), when the luminosity is suppressed due to penetration of the diffusion depth deep into the envelope. While we acquire a good fit to the early-time light curve for a low-mass envelope of  $M_e = 0.05 M_\odot$ ,  $R_e = 110 R_\odot$ , and  $E = 1.5 \times 10^{50} \text{ erg}$  (see Fig. A2), we consider this fit to be unphysical. The fit implies the envelope is fully transparent by day 2.5, ( $t_{\text{ph}} = (0.08 \kappa M_e^2 / E_e)^{1/2} \text{ s} = 2.4 \text{ day}$ ). This implies a break in the photospheric radius to a receding  $R_{\text{BB}}$  should occur at roughly the same time, due to the same change creating the luminosity decline (Piro et al. 2021, their Figs. 1 and 3). However, this does not happen until much later in the evolution, around day 10. Furthermore, a power law of  $R_{\text{BB}} \approx t^{0.8}$  does not fit our data well even during the validity of the model (see Fig. A5), and so we disfavor this interpretation.

Following  $t = 2.2$  days, the temperature evolves with a power law slope of  $\alpha_2 = -0.3 \pm 0.1$ , consistent with the predicted power-law slope for C/O or He/C/O composition (Rabinak & Waxman 2011). We fit a combined shock-cooling and  $^{56}\text{Ni}$  decay model (with the parameters found in § 4.3) to the light curve at  $2 < t < 5$  days when  $^{56}\text{Ni}$  accounts for less than 50% of the observed luminosity. We use the shock-cooling models of Morag et al. (2022), calibrated to numerical grey simulations, and based on realistic opacities for a H-dominated composition. In the case of SN 2022oqm, a composition of C/O or He/C/O is appropriate, as some amount of He might be present even in the absence of He lines in the photospheric spectrum (Hachinger et al. 2012; Teffs et al. 2020). In order to account for a C/O or He/C/O composition of the ejecta, we chose a constant opacity of  $\kappa = 0.2 \text{ cm}^2 \text{ g}^{-1}$ , which we calculate to be appropriate for fully ionized He/C/O mixture (applicable to

the early-time CSM) and for a wide He fraction range.<sup>17</sup> The model is described in detail in § A.2.

We use the nested-sampling (Skilling 2006) package *dynesty* (Higson et al. 2019; Speagle 2020) to fit our likelihood function to the observed photometry. While we consider wide priors on all parameters, we limit ourselves to  $M_{env} < 1 M_{\odot}$ , in order to remain consistent with our estimate for the ejected mass from § 4.3. The light-curve and blackbody evolution are well described by a model with  $R = 310_{-110}^{+30} R_{\odot}$ ,  $M_{env} = 0.23_{-0.07}^{+0.44} M_{\odot}$ , and with a shock velocity parameter (related to the bulk velocity by  $v_{ej} \approx 5 \times v_{s,*}$  Morag et al. 2022) of  $v_{s,*} = 1900_{-190}^{+850} \text{ km s}^{-1}$  which we show in Fig. 14, as well as the corresponding blackbody fits in Fig. A6. In the Sapir & Waxman (2017); Morag et al. (2022) framework, the fit is terminated at  $t_{tr}/2$ , where  $t_{tr} = 9.2$  days is the envelope transparency time for our best fit model, equivalent to  $t_{ph}$  in Piro et al. (2021), and very close to  $\tau_m$  in definition.<sup>18</sup>, in excellent agreement with the diffusion time we get from the fit to the <sup>56</sup>Ni peak, indicating our results are self-consistent. We conclude that while the early ( $t < 2.5$  d) peak is unlikely to be powered by shock cooling, this process can explain the dominant emission seen between  $2 < t < 5$  d, until the Ni luminosity begins to dominate.

### 5.3.2. Ongoing CSM Interaction or Shock Breakout in a Wind?

The presence of lines at velocities of  $4000 \text{ km s}^{-1}$  in both absorption and emission that disappear after 2.5 days provides compelling evidence for the presence of a CSM. We calculate here several estimates for the mass of this CSM lying above the photosphere when SN 2022oqm was first observed. Throughout this section, we assume a profile  $\rho_{CSM} = Ar^{-s}$ , between  $r_{in} = 1.75 \times 10^{14} \text{ cm}$  (the first observed photospheric radius) and  $r_{out} = 5 \times 10^{14} \text{ cm}$  (the approximate location of the photosphere at the time when the early features disappear) with typical values between  $s = 0$ , appropriate for a constant-density CSM shell and  $s = 2$ , appropriate for a continuous wind (Chevalier & Liang 1989; Dwarkadas

2011). We assume the CSM opacity  $\kappa$  is space independent. We can derive limits on  $M_{CSM}$  by using the CSM density profile and considering the optical depth  $\tau$ :

$$M_{CSM} = \int_{r_{in}}^{r_{out}} 4\pi\rho r^2 dr \text{ and } \tau = \int_{r_{in}}^{r_{out}} \kappa\rho dr \quad (12)$$

Since our earliest observations do not show direct evidence for a wind shock breakout still ongoing at the time of detection (in contrast, e.g., to SN 2006aj, Waxman et al. 2007), we can place an upper limit on the mass of the circumstellar material lying ahead of the photosphere during our first observations ( $t \approx 0.5$  days). At this time, the remaining CSM must have an optical depth  $\tau \leq c/v$ , so:

$$\rho_{in} \leq \frac{c}{v_{ej}} |s - 1| \kappa_{cont}^{-1} r_{in}^{-1} \left| \left( \frac{r_{out}}{r_{in}} \right)^{1-s} - 1 \right|^{-1} \quad (13)$$

which gives an upper limit of  $\rho_{in} \leq 2 \times 10^{-12} \text{ g cm}^{-3}$  for  $s = 2$ , and  $\rho_{in} \leq 7 \times 10^{-13} \text{ g cm}^{-3}$  for  $s = 0$  for  $v_{ej} = 20,000 \text{ km s}^{-1}$ . By integrating this density we can limit the CSM mass to  $M_{CSM} \leq 0.06 M_{\odot}$  for  $s = 2$ , and  $M_{CSM} \leq 0.17 M_{\odot}$  for  $s = 0$ .

We can also place a minimum bound on the mass and density of the CSM from the fact that line photons escape. We assume that the C III and C IV lines in the unshocked CSM are emitted from a region  $\tau_l = \int_r^{\infty} \rho\kappa_{eff} dr = 1$  (noting that the effective absorption opacity  $\kappa_{eff} \gg \kappa_T$ ), where  $\kappa_T$  is the Thompson opacity. For Doppler-broadened lines that are resolved in frequency,  $\kappa_{eff}$  will be determined by the peak height of the frequency dependent opacity  $\kappa_{\nu}$  for the broadened line (for an in-depth discussion, see Rabinak & Waxman 2011). We therefore choose  $\kappa_{eff} \approx \frac{c}{v} \kappa_l$ , where the intrinsic line opacity is  $\kappa_l \equiv \frac{1}{\lambda_0} \int \kappa_{\lambda} d\lambda$ , with the integral performed across the line, and  $\lambda_0$  is the natural wavelength of the line. We get as a lower bound a mass of

$$M_{CSM} = 4\pi \frac{s-1}{s-3} \frac{r_{out}^{3-s} - r_{in}^{3-s}}{r_{out}^{1-s} - r_{in}^{1-s}} \kappa_{eff}^{-1}. \quad (14)$$

While we cannot infer an exact value for  $\kappa_l$ , as the density and temperature of the CSM at the line forming region are unknown, we can calculate it for a wide range of values and provide a limit. We calculate the opacity for the C III  $\lambda\lambda 4647, 4650$  and for C IV  $\lambda 4658$  features using the open-source opacity table described in Morag et al. (2022) and based on Kurucz (1995) atomic line lists. We find an upper limit of  $\kappa_l \lesssim 10^{-2} \text{ cm}^2 \text{ g}^{-1}$ . In Fig. A7, we show the line opacities near  $4650 \text{ \AA}$ , for the density resulting in the highest line opacities. The opacity upper

<sup>17</sup> The choice of a constant opacity is in lieu of the approximate temperature-dependent opacity employed in the He/C/O model extensions in Rabinak & Waxman (2011). The shock cooling luminosity is determined deep in the ejecta where the local temperature is higher than both the photosphere temperature and the observed emission temperature, and as a result the opacity in this regime is approximately constant, and higher than the opacity of  $\kappa = 0.07 \text{ cm}^2 \text{ g}^{-1}$  typically assumed for SNe Ic. We defer a more detailed study of the effect of He/C/O composition on shock-cooling emission to later work.

<sup>18</sup> In the framework of Sapir & Waxman (2017); Morag et al. (2022),

$$t_{tr} = \sqrt{\frac{\kappa M_{env}}{8\pi c v_{s,*}}} \approx 0.9\tau_m$$

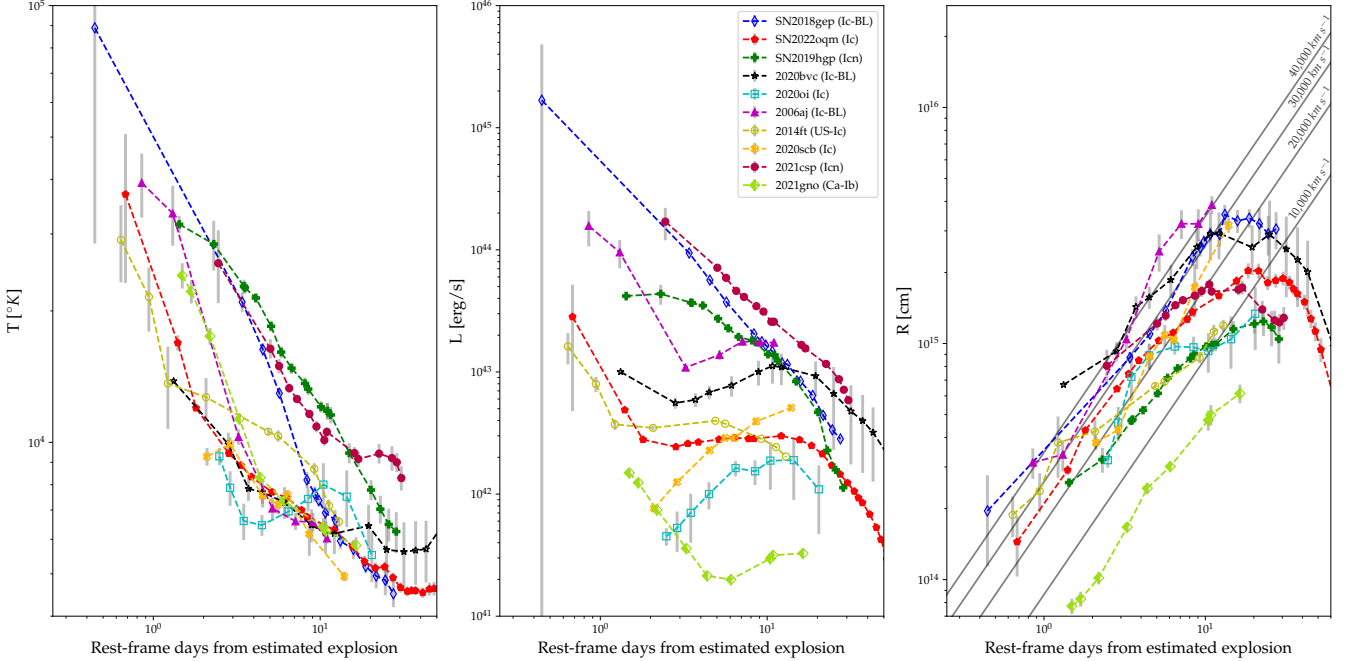


**Figure 11.** Blackbody evolution of SN 2022oqm compared to that of several SNe Ic, Ic-BL, and Icn. Several other SNe Ic have early-time peaks in their luminosity, an initial rapid temperature decline, and high initial photospheric velocities. In particular, SN 2020scb does not show this behavior, while SN 2020oi and SN 2006aj do.

limit implies a lower mass limit of  $M_{\text{CSM}} \gtrsim 7 \times 10^{-4} M_{\odot}$  assuming  $s = 2$ , and  $M_{\text{CSM}} \gtrsim 10^{-3} M_{\odot}$  assuming  $s = 0$ .

The upper mass limit from the continuum optical depth is quite robust. The lower mass limit is less strict: the line opacity depends on the occupation fraction of the electron states of the C ions, which is here determined by LTE, and can vary due to NLTE effects and due to the possible effect of ionizing X-ray photons absorbed in the material. Given these caveats we can proceed.

### 5.3.3. Self-Consistency of the Proposed Scenario

Murase et al. (2014) explore a simple framework for CSM interaction, where the ejecta collide with a CSM shell in a plastic collision. By demanding that the energy and momentum are conserved, the dissipated energy in the collision will provide an estimate for the interaction luminosity up to adiabatic losses. We consider a similar scenario, but modify it, considering only an external layer of the ejecta. The dissipated energy from a plastic collision between a shell of CSM and an ejecta layer with  $M_{\text{ej},i}$  and  $v_{\text{ej},i}$  is

$$\Delta E = \frac{1}{2} \frac{M_{\text{ej},i} M_{\text{CSM}}}{(M_{\text{ej},i} + M_{\text{CSM}})} (v_{\text{ej},i} - v_{\text{CSM}})^2 \quad (15)$$

During this collision, the ejecta creates a forward shock in the CSM, and the CSM will act as a piston on the ejecta, creating a reverse shock and decelerating it. The reverse shock is expected to dissipate when

it sweeps up roughly an equal amount of ejecta mass to the CSM. Considering an external ejecta layer with mass  $M_{\text{ej},i} = M_{\text{CSM}}$  that is colliding with the CSM:

$$\Delta E = \frac{1}{4} M_{\text{CSM}} (v_{\text{ej}} - v_{\text{CSM}})^2 \quad (16)$$

In an optically thin wind, all the dissipated energy (neglecting adiabatic losses) will be radiated within a light travel time  $t \approx R/c$  for a spherical CSM. If the CSM is optically thick, the emission will occur on a dynamical time  $t \approx R/v$ , or a diffusion time  $t = \sqrt{\frac{3\kappa M}{4\pi cv}}$  (Ofek et al. 2010; Chevalier & Irwin 2011).

When integrating the bolometric light curve we find that  $E_{\text{rad}} \approx 1.5 \times 10^{48}$  erg were emitted from 0.5 to 3 days after the explosion. Assuming that the spectroscopic line velocity we see in the first spectra  $v_{\text{CSM}} = 4000 \text{ km s}^{-1}$  is that of the unshocked CSM that is then swept up by the SN ejecta and accelerated to  $v_{\text{ej}} = 20,000 \text{ km s}^{-1}$  that we deduce from the early-time blackbody radius evolution, we can estimate the CSM mass:

$$M_{\text{CSM}} \approx \frac{4E_{\text{rad}}}{(v_{\text{ej}} - v_{\text{CSM}})^2} = 6.6 \times 10^{-4} M_{\odot} \quad (17)$$

The inferred CSM mass is much smaller than the ejecta mass, which is self-consistent with the assumption only the most outer ejecta layer is interacting with the CSM, and is in good agreement with our limits from

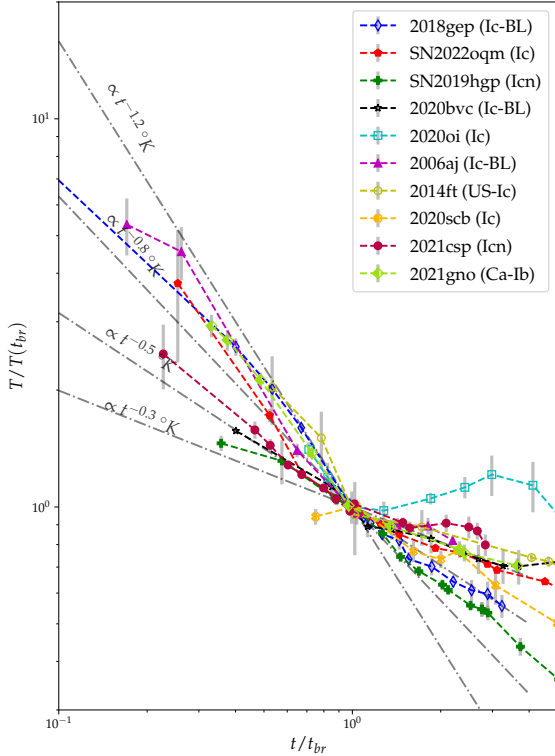


**Figure 12.** Temperature evolution of SN 2022oqm compared with that of several SNe Ic, Ic-BL, and Icn. The temperature has been normalized to an arbitrary time where a break is observed in the power law evolution. Grey dashed lines represent various power laws. While the initial logarithmic slope of the temperature is diverse, fast-evolving SNe (SN 2018gep, SN 2019hgp, and SN 2021csp) exhibit a fast decline, and double-peaked SNe (SN 2022oqm, SN 2020bvc, SN 2020oi, SN 2021gno, and SN 2006aj) show a break in their evolution.

the previous section. If we use Eq. 16 for the upper limit we derived on the CSM mass of  $0.06 M_{\odot}$ , the condition that  $\tau \leq \frac{c}{v}$ , would result in  $3 \times 10^{50}$  erg released as dissipated energy. Alternatively, a CSM mass of  $7 \times 10^{-4} M_{\odot}$  implies an optical depth of  $\tau = 0.4$  for  $s = 0$  or  $\tau = 0.1$  for  $s = 2$ . As  $\tau$  is much smaller than  $\frac{c}{v}$  this argues against either a shock breakout from an optically thick CSM shell, or the interaction of the ejecta with an optically thick wind as the powering mechanism for the early light curve during the observed phase, and is consistent with our assumption of an optically thin wind.

Next, we check if the presence of the reverse shock does not impact the intermediate-time shock-cooling emission, discussed in § 5.3.1. Since the reverse shock

will dissipate when the swept-up CSM mass will match the shocked ejecta, we can estimate the fraction of the ejecta affected by the reverse shock. This estimate is relevant only if the amount of CSM mass above the photosphere is similar to the CSM mass already shocked when observations began. This is the case for  $s = 0 - 2$ , but not for a steep density profile  $s > 2$ . We use Rabinak & Waxman (2011) Eq. 11 (recast in terms of  $v_{s*,8.5}$  using Morag et al. (2022) Eq. 3). Namely,

$$M_{\text{ph}}/M_{\text{ej}} \approx 4 \times 10^{-4} \frac{v_{s*,8.5}^{1.6}}{(M_{\text{ej}}/1 M_{\odot})^{0.8} \kappa_{0.34}^{0.8}} t_{\text{days}}^{1.5} \quad (18)$$

where  $M_{\text{ph}}$  is the mass outside of the photosphere and  $M_{\text{ej}}$  is the ejecta mass. To estimate  $M_{\text{ph}}/M_{\text{ej}}$ , we choose the previously derived values  $v_{s*} = 1900 \text{ km s}^{-1}$ ,  $\kappa = 0.2 \text{ cm}^2 \text{ g}^{-1}$  and  $M_{\text{ej}} \lesssim 1 M_{\odot}$  for  $t > 2.5$  days, we get  $M_{\text{ph}} \gtrsim 10^{-3}$ , which is equal to or larger than our CSM estimate. We conclude the early CSM light-curve component does not significantly impact the use of shock-cooling models at later times, under the assumption the density profile of the CSM is not steep.

Finally, we can check whether our non-detection of X-rays at early time is consistent with the optically thin CSM we find. A shock breakout in a stellar wind is expected to be accompanied by a forward-propagating collisionless shock that would harden the emitted spectrum and convert some of the thermal photons into hard X-rays (Katz et al. 2011), although the exact thermal and hard X-ray spectrum is currently unknown. X-ray radiation emitted by this mechanism is also likely to be absorbed by photo-ionization in the CSM, if it exists. For SN 2006aj, where a wind breakout likely occurred (Waxman et al. 2007) an X-ray flux of the same order of the optical flux was observed during the first day. Assuming this is also the case here, we check if the X-ray opacity of the CSM we deduce is high enough to bring the X-ray emission below our observed limit.

We calculate the X-ray opacities of the CSM for a wide range of CSM temperature and densities and find that at  $T \lesssim 30 \text{ eV}$  the X-ray opacity is in the range  $10^2 - 10^5 \text{ cm}^2 \text{ g}^{-1}$ , so that  $\kappa > 100 \text{ cm}^2 \text{ g}^{-1}$ . In Fig. A8, we show a representative example for the effect of temperature on the bound-free absorption in the CSM. We calculate the optical depth of X-rays given this lower limit and find  $\tau > 130$ . Alternatively, less than  $\sim 7 \times 10^{-5} M_{\odot}$  are sufficient to make the CSM optically thick to X-rays. While our calculation does not include NLTE effects, and taking into account the breakout flash (as opposed to the X-rays from the collisionless shock), this analysis shows that for a C/O composition, unless the CSM is almost fully ionized, a small amount of matter is sufficient to totally absorb the initial X-ray radiation.

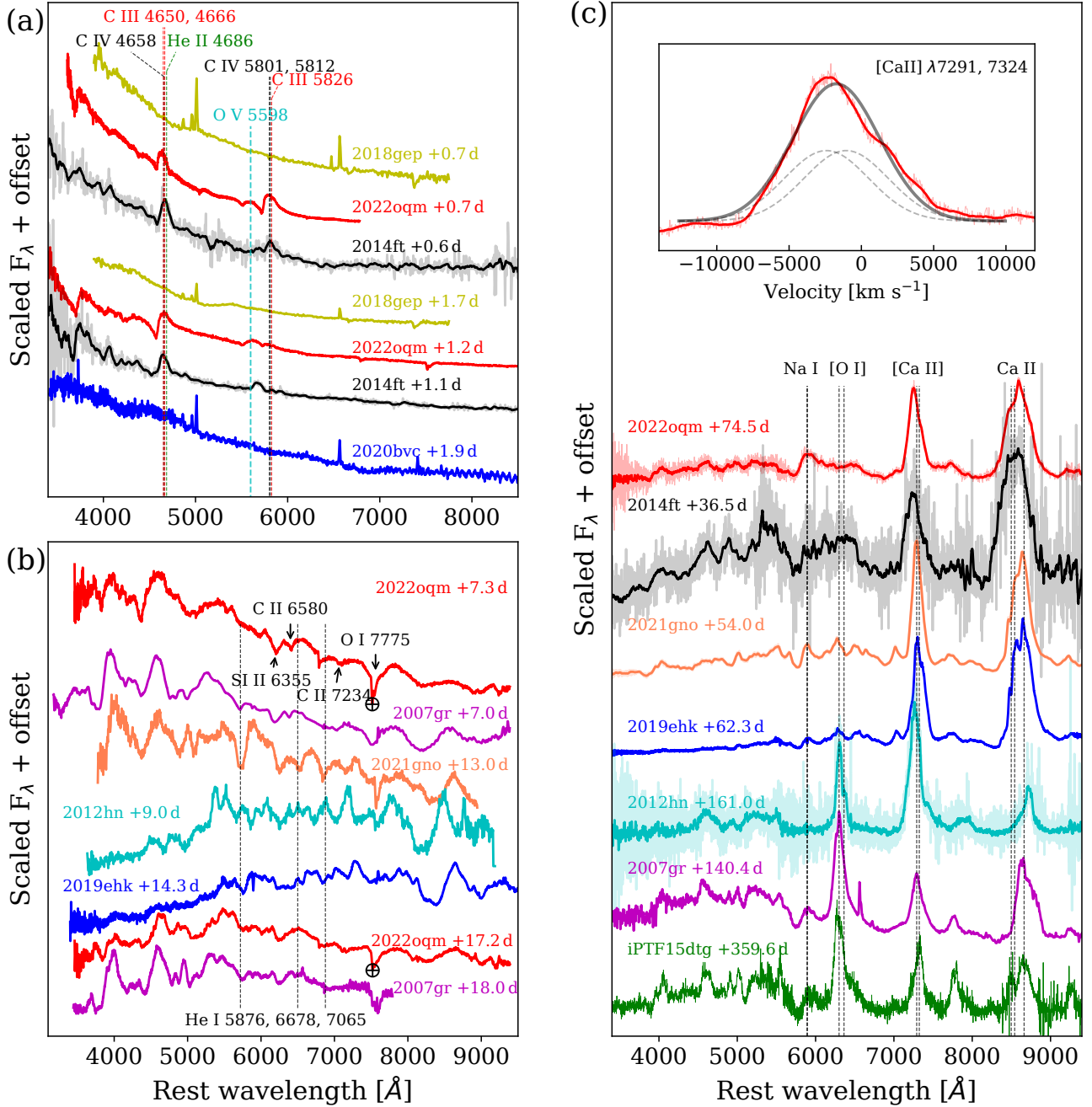


**Figure 13.** Spectral comparison between SN 2022oqm and other SNe at different phases. All of the phases are given relative to the estimated explosion time. (a) Within two days after the estimated explosion time, (b) spectra around the primary peak in optical bands, and (c) spectra at  $> 1$  month after peak light. In panels (a) and (c), features of interest are marked at rest, and in panel (b) with a shift of  $8000 \text{ km s}^{-1}$ . At early times, SN 2022oqm is most similar to SN 2014ft. During the photospheric phase, it is similar to typical SNe Ic such as SN 2007gr, and at late times it is characterized by a Ca-rich spectrum like SN 2014ft and the Type IIb SN 2019ehk, and unlike the double-peaked SN Ic iPTF15dtg. Some spectra are smoothed with a Savitzky–Golay filter (Savitzky & Golay 1964). The inset in panel (c) shows the velocity profile of the Ca II  $\lambda\lambda 7291, 7324$ , where the average wavelength of  $7307.5 \text{ \AA}$  was adopted for the reference wavelength. The black solid line shows the best-fit Gaussian model ( $\text{FWHM} = 6900 \text{ km s}^{-1}$ ,  $\Delta v = 1700 \text{ km s}^{-1}$ ), whereas the dashed lines show the individual emission components for which the fluxes were fixed to be equal in our fitting.

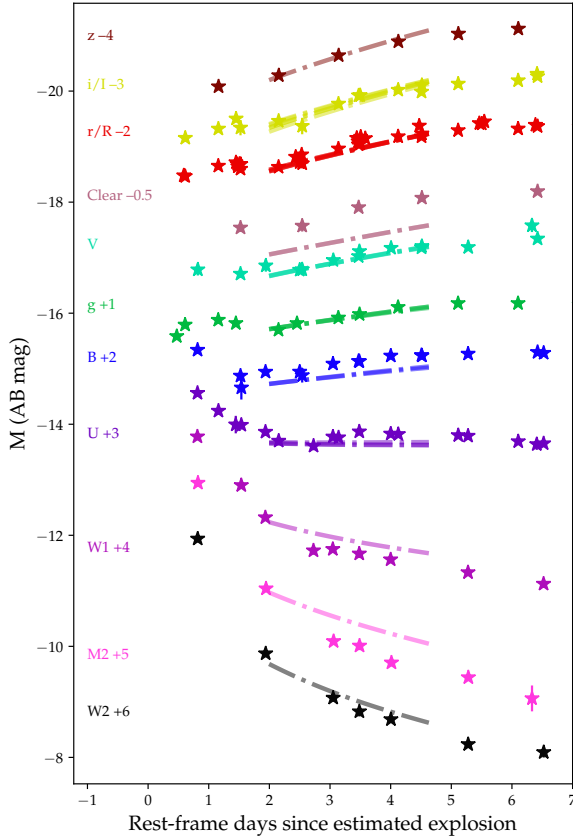


**Figure 14.** Best fit shock-cooling Morag et al. (2022) model to the intermediate-time ( $5 > t > 2$  days) light curves, along with the observations of SN 2022oqm at these times. The best fit model is plotted up to  $t < t_{tr}/2 = 4.6$  days. The light-curve and blackbody evolution are well described by a model with  $R = 310_{-110}^{+30} R_{\odot}$ ,  $M_{env} = 0.23_{-0.07}^{+0.44} M_{\odot}$ , and by  $v_{s,*} = 1900_{-190}^{+850} \text{ km s}^{-1} \approx v_{ej}/5$ . We note  $t_{tr}$  is in good agreement with the equivalent diffusion time  $\tau_m$ , acquired from the  $t > 12$  days  $^{56}\text{Ni}$  fit.

Since both O IV and C IV features are identified in the first spectrum, and the exponential dependence of the ionization fraction on temperature, a large fraction of the CSM being fully ionized is strongly disfavored, and high X-ray suppression is likely.

#### 5.4. Implications of the Lack of Pre-SN Emission

The early emission lines disappear at day three after the explosion which might indicate that the ejecta have swept up the entire CSM at this time. For an ejecta velocity of  $v_{ej} = 20,000 \text{ km s}^{-1}$  as we measure at early times, this would imply that the CSM is located at a

distance of  $R_{\text{CSM}} = 5 \times 10^{14} \text{ cm}$  and that the CSM was ejected  $\sim 15$  days before the SN explosion, given a CSM velocity of  $\sim 4000 \text{ km s}^{-1}$ . We note that if the velocity difference observed between the first two epochs is due to acceleration, the CSM might have been ejected earlier.

We here estimate the energy that is required to unbind  $7 \times 10^{-4} M_{\odot}$  of material from a massive compact progenitor. We assume a W-R progenitor star with a radius of  $R_{\text{star}} = 1 R_{\odot}$  and a mass of  $M_{\text{star}} = 10 M_{\odot}$  (Nugis & Lamers 2000), and find that unbinding the CSM from the stellar surface requires

$$\frac{E_{\text{pot}}}{10^{46} \text{ erg}} = 3.8 \left( \frac{M_{\text{star}}}{10 M_{\odot}} \right) \left( \frac{M_{\text{CSM}}}{10^{-3} M_{\odot}} \right) \left( \frac{R_{\text{star}}}{R_{\odot}} \right)^{-1} \quad (19)$$

, which is negligible compared to the CSM kinetic energy given by

$$\frac{E_{\text{CSM,kin}}}{10^{47} \text{ erg}} = 1.6 \left( \frac{M_{\text{CSM}}}{10^{-3} M_{\odot}} \right) \left( \frac{v_{\text{CSM}}}{4000 \text{ km s}^{-1}} \right)^2. \quad (20)$$

As shown in § 3.4, we can rule out precursors that are brighter than  $-14$  mag in the  $i$  band and last for at least two weeks in the last 100 days before the SN explosion. The precursor luminosity depends on its duration and is given as

$$L_{\text{prec}} = \epsilon \frac{E_{\text{CSM,kin}}}{\Delta t} = 2 \times 10^{41} \text{ erg s}^{-1} \left( \frac{\Delta t}{\text{week}} \right)^{-1} \quad (21)$$

The fact that no precursor was detected allows us to constrain the radiative efficiency  $\epsilon$ , the fraction of CSM kinetic energy converted to optical radiation e.g., by collision with pre-existing CSM.

While the progenitors of most SNe II<sub>n</sub> are likely surrounded by material ejected during earlier eruptions, the immediate surroundings of the progenitor of SN 2022oqm could have had a low matter density at the time of the outburst. This could significantly reduce the efficiency of a pre-explosion outburst. Furthermore, CSM interaction in an optically thin environment would likely result in radiation outside the optical bands. For example, in the first UV observation of SN 2022oqm only a small fraction ( $< 10\%$ ) of the total observed luminosity is radiated in the optical bands.

We require that the precursor is fainter than  $-14$ . For a week-long precursor, this constrains the radiative efficiency to  $\epsilon < 0.45$ , or  $\epsilon < 0.2$  for a 3-day-long outburst, both of which are not constraining limits, and indicate that the CSM could have been ejected in an outburst below our detection threshold in the observed bands.



### 5.5. Searching for $> 100$ keV Breakout Emission

When a massive progenitor explodes, a radiation-mediated shock will travel down the density profile of the star, until the optical depth of the material above the shock region drops below  $c/v$  (Weaver 1976). If it is sufficiently dense, this process will occur in the CSM. Depending on the breakout radius  $R_{\text{br}}$ , an early UV-optical flash might be observed, lasting for a time equal to  $\sim R_{\text{br}}/v$  (Ofek et al. 2010; Chevalier & Irwin 2011; Svirski et al. 2012). As mentioned in § 5.3.3, the optical depth of the CSM above the photosphere is smaller than unity at the time we first start observing. Thus, a CSM breakout would have occurred before observations began. This is consistent with the observations of SN 2006aj a SN accompanied by a low-luminosity GRB lasting  $\sim 10^4$  s, interpreted as the CSM breakout (Waxman et al. 2007). In that case, the optical and UV bands rose to peak over a day timescale, resulting in an early UV-optical peak similar to that observed for SN 2022oqm, as shown in Fig. 9 and 11.

While we most likely did not observe the breakout flash, a considerable amount of CSM (compared to  $\sim 10^{-3} M_{\odot}$  we infer) might have been shocked prior to our observations if the CSM has a steep density profile ( $s > 2$ ). In this case, a large amount of shocked material originating from both the CSM and the ejecta might still be cooling up to  $t = 3$  d, as described by Eq. 18. The post-breakout cooling of this material might account for some of the early radiation, and could possibly account for the shock-cooling-like temperature and radius evolution at  $t > 2$  days. Chevalier & Irwin (2011) show that the shocked CSM can be approximated with a self-similar evolution with  $n = 7$ , compared to  $n = 10$ –12 for stellar envelopes (Matzner & McKee 1999), so the density profile at the photosphere can be steep. If the velocity profile is similar to the stellar case, one might expect a shock-cooling-like blackbody evolution.

As was observed for SN 2006aj, a CSM breakout around a SN Ib/c progenitor is expected to peak in the 100 keV – MeV range (Waxman et al. 2007; Katz et al. 2011; Granot et al. 2018; Margalit et al. 2022), resulting in a low-luminosity GRB. We search for a coincident GRB in the *Fermi*/GBM and *Swift*/BAT instruments. No onboard, or sub-threshold trigger, was found during the putative breakout window of  $2459771.2 \pm 0.5$  JD, that is also consistent with the location of SN 2022oqm. During this time period SN 2022oqm was visible to *Fermi* and *Swift* (above the Earth limb)  $\sim 70\%$  of the time. Using the *Fermi*/GBM trigger sensitivity, we rule out the existence of a GRB with peak flux greater than  $\sim 1 \times 10^{-7}$  erg s $^{-1}$  cm $^{-2}$ , (50–300 keV) within this win-

dow. However, the sensitivity to a GRB 060218-like transient with *Fermi*/GBM is degraded due its relatively slow evolution, with variability timescales comparable to the background variability experienced by *Fermi*/GBM in Low-Earth Orbit. A search using data from Konus-Wind could likely rule out a CSM breakout over the entire time window, but to shallower depths of  $\sim 5 \times 10^{-7}$  erg s $^{-1}$  cm $^{-2}$  (20 keV – 10 MeV) (Ridnaia et al. 2020). Neither of these limits are sensitive enough to constrain a GRB 060218-like transient at the distance of SN 2022oqm, which would peak at a flux of  $\sim 3 \times 10^{-8}$  erg s $^{-1}$  cm $^{-2}$  (15–150 keV).

In the next few years, *The Ultraviolet Transient Astronomy Satellite (ULTRASAT)* will begin a 200 deg $^2$  high-cadence UV survey (Shvartzvald et al. 2023), and is expected to detect the early UV emission of hundreds of CCSNe, of which a fraction will be SNe Ib/c (Ganot et al. 2016). An early UV flash observed with *ULTRASAT* will not only provide information about CSM emission, but will also enable early X-ray observations and a systematic study of coincident GRBs. Finding coincident low-luminosity GRBs for a large fraction of SNe Ib/c with an early UV peak will demonstrate these are the result of spherical CSM breakouts, while having meaningful limits on coincident GRBs will favor a beamed interpretation. We encourage sub-threshold searches for similar future discoveries.

### 5.6. A Population of Explosions?

Although its bulk properties such as peak time and luminosity are similar to those of the general SN Ic population, SN 2022oqm shows several peculiarities separating it from spectroscopically regular SNe Ic. It has an early peak only seen in a few other SNe Ib/c and SNe Ic-BL. The SN interacts with a compact distribution of C/O-dominated CSM, directly observed so far only in rare cases such as SNe Icn (e.g., Ben-Ami et al. 2014; Gal-Yam et al. 2022; Perley et al. 2022; Gagliano et al. 2022; Pellegrino et al. 2022), and indirectly implied in (for example) SN 2018gep through its precursor emission (Ho et al. 2019). Compared with Ca-rich transients, its Ca-dominated nebular spectrum, rise to peak luminosity by 12 days, and offset location are consistent with the Ca-rich population (Perets et al. 2010; Kasliwal et al. 2012; De et al. 2018). However, few examples of Ca-rich SNe Ic (rather than Ib) have been previously observed. SN 2022oqm is significantly more luminous, with a higher  $^{56}\text{Ni}$  mass, and more rapidly declining than most Ca-rich SNe Ib (De et al. 2018; Sharon & Kushnir 2023). Notably, this also holds with respect to the Ca-rich SN Ic SN 2012hn. In at least two Ca-rich SNe Ib (SN 2021gno, SN 2021inl), a short-lived and

blue peak similar to that of SN 2022oqm has been observed. In the case of SN 2019ehk, an early blue peak has been accompanied by short lived and narrow H and He emission lines from a compact CSM. While the early behavior is similar, the different composition challenges a similar progenitor or explosion mechanism as that of SN 2022oqm.

Though different in its total radiated luminosity, a notably similar SN to SN 2022oqm is the Ca-rich Ic SN 2014ft (De et al. 2018). It has an early peak, a fast drop in temperature, a similar peak magnitude, a Ca-dominated nebular spectrum, and is extremely offset ( $\sim 50$  kpc) from the nearest massive galaxy with the same redshift. The common features between the early-time spectrum of SN 2014ft and SN 2022oqm (Fig. 13) suggests a similar CSM composition. We propose that lines of C IV and C III dominate the early spectra, rather than He II as originally inferred from the early-time spectrum of SN 2014ft, as it better matches the peak emission, and owing to the presence of other highly ionized C lines. However, SN 2022oqm has different bulk properties. An order of magnitude more mass was ejected and  $^{56}\text{Ni}$  synthesized in the explosion compared to SN 2014ft, as evident by the slower evolution of SN 2022oqm. It remains to be seen if future SNe show common similarities to these two objects in CSM, location, and nebular-phase spectra, supporting a common origin. Since Ca-rich transients, as well as SNe Ic, are diverse in their properties, and might originate from different channels, it is unclear if SN 2022oqm and SN 2014ft are the extreme end of a distribution of the SN Ic population, the Ca-rich transient population, or represent their own unique group. Any single explosion mechanism or progenitor channel investigated in future studies would need to account for an order of magnitude difference in ejected mass and  $^{56}\text{Ni}$  mass between the two.

## 6. Interpretation

### 6.1. Option 1: A Massive Progenitor, Embedded in CSM Ejected during its Final Weeks

Many of the properties of SN 2022oqm are consistent with the general properties of SNe Ic, favoring a massive star origin. The presence of C/O CSM can be explained naturally in a massive-star scenario by an eruptive ejection of material shortly before the terminal explosion. or by the radiative acceleration of a shell of pre-existing dense CSM. Such a pre-SN eruption is expected to eject material in the last stages of the evolution of massive stars (Smith 2014; Fields & Couch 2021; Varma & Müller 2021; Yoshida et al. 2021; Matsumoto & Metzger 2022). In terms of location, while remote, the offset of SN 2022oqm is consistent with the general offset

distribution of SNe Ic (Schulze et al. 2021), and cannot exclude a massive star origin, and while the [O I] nebular luminosity has been connected to progenitor mass (Jerkstrand et al. 2015), the general SN Ic population shows no correlation between  $M_{\text{ej}}$  and [O I] nebular luminosity (Prentice et al. 2022).

Shock-cooling models of an extended  $R \approx 300 R_{\odot}$  progenitor describe the behavior of the light curves at  $2 < t < 5$  days, and produce a diffusion timescale which is consistent with the one acquired from the  $^{56}\text{Ni}$  fits at  $t > 12$  days. As discussed in § 5.5, the shock cooling following a CSM breakout might also produce a similar behavior, for which we do not have a numerically calibrated model allowing parameter estimation. If we have observed the cooling of the stellar envelope, the progenitor would have to be a stripped star with an inflated envelope. If we are observing CSM cooling, a CSM originating in a W-R star could explain the observations. A massive-star origin has been previously suggested for several Ca-rich transients (Jacobson-Galán et al. 2020; De et al. 2021). Sharon & Kushnir (2023) test various explosion models from the literature and find that most are inconsistent with the observed  $M_{\text{Ni}}-t_{\gamma}$  distribution of He-shell detonations and core collapse of ultrastripped stars, but are consistent with some SNe Ia and core collapse of stripped-star models. Our inferred values for SN 2022oqm of  $M_{\text{Ni}} = 0.106 M_{\odot}$ ,  $M_{\text{ej}} = 1.1 M_{\odot}$ , and  $t_{\gamma} = 36$  d place SN 2022oqm in the region broadly consistent with stripped-envelope SN explosions of Dessart et al. (2016); Woosley et al. (2021), with an ejected mass in the  $0.5-3 M_{\odot}$  range.

### 6.2. Option 2: A White Dwarf Progenitor Disrupting a C/O Companion

Since the ejected mass of the explosion is within the mass range of WDs, we consider a system containing such a star as a possible progenitor for the explosion. The velocity of the features in the first few spectra are around  $4000 \text{ km s}^{-1}$  (P Cygni minimum), and up to  $15,000 \text{ km s}^{-1}$ . Such a velocity is of the order of the escape velocity from the surface of a WD, projected on the line of sight. A WD progenitor for SN 2022oqm is consistent with the lack of detectable nebular [O I] emission, which correlates with progenitor mass in nebular spectral modeling of core-collapse SNe (Jerkstrand et al. 2015), and is thus expected for a massive star progenitor. The strong Ca emission in the nebular phase, marking SN 2022oqm as Ca-rich, connects it with a population of transients which is associated with non-star-forming locations and with a thermonuclear origin (Perets et al. 2010; Kasliwal et al. 2012; Lunnan et al. 2017; De et al. 2020). However, this preference of Ca-rich transients is,

to the best of our knowledge, not demonstrated for Ca-rich spectral subtypes independently. While [De et al. \(2020\)](#) explain all H-poor Ca-rich events within a framework consisting of double detonation of He shells on WDs, some Ca-rich transients have been suggested to have a massive star origin, such as the Ca-rich SNe IIB iPTF 15eqv ([Milisavljevic et al. 2017](#)) and SN 2019ehk ([Jacobson-Galán et al. 2020](#); [De et al. 2021](#)).

A non-massive-star origin would be consistent with the location of the explosion in the outskirts of its host, and  $> 3$  kpc from any luminous UV source. As massive stars have short lifetimes ( $< 10$  Myr), a progenitor star would have to travel at more than  $300 \text{ km s}^{-1}$  for 10 Myr to cover such a distance. While CCSNe (and specifically, SNe Ic) do occur occasionally in offset regions or regions with low star-formation ([Hosseinzadeh et al. 2019](#); [Irani et al. 2019, 2022](#)), a population which preferentially explodes in non-star-forming regions cannot originate from massive stars. If SN 2014ft and SN 2022oqm are part of the same population, and other SNe with similar properties will be found in similar sites, this would imply a non-massive-star origin for these events. Our limits on an underlying point source do not exclude the presence of globular clusters ([Richtler 2003](#)) and ultra-compact dwarf galaxies ([Brüns & Kroupa 2012](#)) where the environment is dense and close binary interactions between compact objects are more likely. However, [De et al. \(2020\)](#) demonstrates that the offset distribution of Ca-rich SNe in general is inconsistent with the globular cluster offset distribution - arguing against their association.

Models predicting an early flux excess for SNe Ia that arise from WD systems involve companion interaction through Roche-lobe overflow ([Kasen 2010](#); [Magee et al. 2021](#)), CSM interaction ([Kromer et al. 2016](#); [Piro & Morozova 2016](#)), and clumpy  $^{56}\text{Ni}$  distribution in the ejecta ([Dimitriadis et al. 2018](#); [Shappee et al. 2018](#); [Magee & Maguire 2020](#)). An early flux excess above the expected  $^{56}\text{Ni}$ -powered light curves has been found to occur in a significant fraction of SNe Ia ([Magee et al. 2020](#); [Deckers et al. 2022](#)).

In the comparisons of [Sharon & Kushnir \(2023\)](#), the location of SN 2022oqm in the  $M_{\text{Ni}}-t_\gamma$  parameter space and its  $M_{\text{ej}}$  are consistent with low-luminosity thermonuclear WD sub-Chandra detonations of [Kushnir et al. \(2020\)](#) or the WD collisions of [Kushnir et al. \(2013\)](#). However the sub-Chandra models of [Kushnir et al. \(2020\)](#) required to produce  $M_{\text{Ni}} = 0.106 M_\odot$  and  $t_\gamma = 36$  d have a progenitor mass of  $M_{\text{prog}} = 0.85 M_\odot$ , in tension with the observed  $M_{\text{ej}} = 1.1 M_\odot$  (on top of the remnant mass).

We propose a scenario where a C/O WD is disrupted by a heavier WD companion. The disruption deposits

the CSM we see, while continuous accretion eventually triggers the explosion of the heavier primary. This could satisfy many of the observed properties of SN 2022oqm. The relatively low amount of  $^{56}\text{Ni}$  synthesized compared to SNe Ia (e.g. [Stritzinger et al. 2006](#); [Scalzo et al. 2014](#)) in combination with the high velocities in the early and nebular phase and the lack of strong Si absorption set this event apart from regular WD explosions as SNe Ia.

## 7. Summary

- SN 2022oqm is a SN Ic detected  $< 1$  day after the explosion, with early UV-optical photometric coverage and a spectrum within 0.6 days of explosion.
- The early spectra of SN 2022oqm show high ionization C/O features, with a mean velocity of  $4000\text{--}5500 \text{ km s}^{-1}$ , with extended blue-edge velocities of  $12,000\text{--}15,000 \text{ km s}^{-1}$  which disappear after 2–3 days. We interpret these lines as a result of combined emission from an optically thin CSM, and the underlying ejecta.
- We infer these lines arise from a CSM with a mass of  $\gtrsim 7 \times 10^{-4} M_\odot$ , which is sufficient to drive the luminosity during the first days.
- We find no significant X-ray emission, expected from interaction shocks, or sub-threshold  $\gamma$ -ray emission. This is consistent with absorption by the CSM mass we estimate, and the expected optical depth in the X-ray band. The  $\gamma$ -ray limits cannot rule out a GRB 060218-like burst, associated with the CSM-breakout of SN 2006aj.
- SN 2022oqm rose rapidly to peak in the optical bands, rising more than  $2.6 \text{ mag day}^{-1}$ , while rapidly declining in the UV. After 3 days, the light curve evolution slows, and the optical light curves rise to a second peak after 15 days.
- During the first 2–3 days, the blackbody temperature and luminosity decline quickly, while the radius expands at  $20,000 \text{ km s}^{-1}$ . This behavior changes roughly at the same time the absorption lines evolve to lower ionization C/O expanding at  $\sim 10,000 \text{ km s}^{-1}$ . The break in the blackbody evolution naturally explains the double-peaked light curve structure.
- Up to the second peak, the luminosity and temperature evolve as expected from shock-cooling.
- About the main peak, SN 2022oqm is similar to a typical SN Ic, with a light curve powered by  $0.12 M_\odot$  of  $^{56}\text{Ni}$ ,  $M_{\text{ej}} = 1.1 M_\odot$ , and  $t_\gamma = 36$  days, and displays a typical spectrum.

- The SN becomes nebular by  $t = 60$  days, developing strong NIR Ca II and [Ca II] emission, with a high FWHM compared to other SNe Ic, and with no detectable [O I]. This marks SN2022oqm as Ca-rich.
- The explosion site is located at the outskirts of a massive star-forming galaxy. While its global properties and the offset are consistent with the general SN Ic population, the combination of no elevated galaxy emission at the SN site and no nearby H II regions challenges a massive star origin.
- SN2022oqm is similar to several other SNe Ic and Ca-rich transients. SN2014ft has a similar early and nebular spectrum. Notably, SN2006aj (a GRB-SN associated with a wind-breakout), SN2020oi (a regular SN Ic associated with CSM through radio emission), and SN2019ehk (a double-peaked Ca-rich SN Iib with He/H narrow features) have an early UV peak, and show similar early declining temperature profiles.
- The upcoming ULTRASAT survey will be able to detect stripped-envelope SNe in their first hours, characterize how common an early UV-optical peak is, and determine its origin.

## 8. Data Availability

All photometric and spectroscopic data of SN2022oqm and SN2020scb used in this paper are made available via WISeREP<sup>19</sup> (Yaron & Gal-Yam 2012). The blackbody fits reported in § 4 will be made available through the journal website in a machine-readable format. The code used for the fitting of the early-time light curve to a power law will be released to <https://github.com/idoirani> upon publication.

## 9. Acknowledgements

We thank Doron Kushnir, Eran Ofek, and Eli Waxman for their insights on the analysis. U.C. Berkeley undergraduate students Raphael Baer-Way, Kate Bostow, Victoria Brendel, Asia deGraw, Kingsley Ehrich, Connor Jennings, Gabrielle Stewart, and Edgar Vidal are acknowledged for their effort in taking Lick/Nickel data. We are grateful to the staff at the various observatories where data were obtained. This work made use of data supplied by the UK Swift Science Data Centre at the University of Leicester.

A.G.-Y.’s research is supported by the EU via ERC grant 725161, the ISF GW excellence center, an IMOS space infrastructure grant and BSF/Transformative and GIF grants, as well as the André Deloro Institute for Advanced Research in Space and Optics, The Helen Kimmel Center for Planetary Science, the Schwartz/Reisman Collaborative Science Program and the Norman E Alexander Family Foundation ULTRASAT Data Center Fund, Minerva and Yeda-Sela; A.G.-Y. is the incumbent of the Arlyn Imberman Professorial Chair. S. Schulze acknowledges support from the G.R.E.A.T research environment, funded by *Vetenskapsrådet*, the Swedish Research Council, project 2016-06012. N.L.S. is funded by the Deutsche Forschungsgemeinschaft (DFG, German Research Foundation) via the Walter Benjamin program – 461903330. A.V.F.’s supernova group at U.C. Berkeley has been supported by Steven Nelson, Alan Eustace, Landon Noll, Sunil Nagaraj, Sandy Otellini, Gary and Cynthia Bengier, Clark and Sharon Winslow, Sanford Robertson, Briggs and Kathleen Wood, the Christopher R. Redlich Fund, the Miller Institute for Basic Research in Science (in which A.V.F. was a Miller Senior Fellow), and numerous individual donors.

Based in part on observations obtained with the Samuel Oschin Telescope 48-inch and the 60-inch Telescope at the Palomar Observatory as part of the Zwicky Transient Facility (ZTF) project. ZTF is supported by the National Science Foundation (NSF) under grants AST-1440341 and AST-2034437, and a collaboration including current partners Caltech, IPAC, the Weizmann Institute of Science, the Oskar Klein Center at Stockholm University, the University of Maryland, Deutsches Elektronen-Synchrotron and Humboldt University, the TANGO Consortium of Taiwan, the University of Wisconsin at Milwaukee, Trinity College Dublin, Lawrence Livermore National Laboratories, IN2P3, University of Warwick, Ruhr University Bochum, Northwestern University, and former partners the University of Washington, Los Alamos National Laboratories, and Lawrence Berkeley National Laboratories. Operations are conducted by COO, IPAC, and UW. The ZTF forced-photometry service was funded under the Heising-Simons Foundation grant #12540303 (PI M. J. Graham). The SED Machine at Palomar Observatory is based upon work supported by the NSF under grant 1106171.

A major upgrade of the Kast spectrograph on the Shane 3 m telescope at Lick Observatory, led by Brad Holden, was made possible through gifts from the Heising-Simons Foundation, William and Marina Kast, and the University of California Observatories. KAIT

<sup>19</sup> <https://www.wiserep.org>

and its ongoing operation were made possible by donations from Sun Microsystems, Inc., the Hewlett-Packard Company, AutoScope Corporation, Lick Observatory, the NSF, the University of California, the Sylvia & Jim Katzman Foundation, and the TABASGO Foundation. Research at Lick Observatory is partially supported by a generous gift from Google. Some of the data presented herein were obtained at the W. M. Keck Observatory, which is operated as a scientific partnership among the California Institute of Technology, the University of California, and NASA; the observatory was made possible by the generous financial support of the W. M. Keck Foundation. The Liverpool Telescope is operated on the island of La Palma by Liverpool John Moores University in the Spanish Observatorio del Roque de los Muchachos of the Instituto de Astrofísica de Canarias

with financial support from the UK Science and Technology Facilities Council. Partly based on observations made with the Nordic Optical Telescope, operated at the Observatorio del Roque de los Muchachos.

*Facilities:* P48, *Swift*(UVOT, XRT), P60 (RC, SEDM), Liverpool telescope (IO:O, SPRAT), Gemini-North, Keck I (LRIS), Shane (KAST), NOT (ALFOSC), P200 (DBSP)

*Software:* *Astropy* ([Astropy Collaboration et al. 2013, 2018](#)), *IPython* ([Perez & Granger 2007](#)), *Matplotlib* ([Hunter 2007](#)), *Numpy* ([Oliphant 2006](#)), *Scipy* ([Virtanen et al. 2020](#)), *extinction* ([Barbary 2016](#)), *FSPS* ([Conroy et al. 2009; Foreman-Mackey et al. 2014](#)), *prospector* V1.1 ([Johnson et al. 2021](#)), *dynesty* ([Skilling 2004, 2006; Feroz et al. 2009; Higson et al. 2019; Speagle 2020](#))

## References

- Ahn, C. P., Alexandroff, R., Allende Prieto, C., et al. 2012, *ApJS*, 203, 21
- Albaret, F. D., Allende Prieto, C., Almeida, A., et al. 2017, *ApJS*, 233, 25
- Arcavi, I. 2017, in *Handbook of Supernovae*, ed. A. W. Alsabti & P. Murdin, 239
- Arcavi, I., Gal-Yam, A., Yaron, O., et al. 2011, *ApJL*, 742, L18
- Arcavi, I., Hosseinzadeh, G., Brown, P. J., et al. 2017, *The Astrophysical Journal*, 837, L2
- Arnett, W. D. 1982, *ApJ*, 253, 785
- Astropy Collaboration, Robitaille, T. P., Tollerud, E. J., et al. 2013, *A&A*, 558, A33
- Astropy Collaboration, Price-Whelan, A. M., Sipőcz, B. M., et al. 2018, *AJ*, 156, 123
- Barbarino, C., Sollerman, J., Taddia, F., et al. 2021, *A&A*, 651, A81
- Barbary, K. 2016, *extinction* v0.3.0, doi:10.5281/zenodo.804967
- Bellm, E. C., Kulkarni, S. R., Graham, M. J., et al. 2019, *Publications of the Astronomical Society of the Pacific*, 131, 018002
- Ben-Ami, S., Konidaris, N., Quimby, R., et al. 2012, in *Society of Photo-Optical Instrumentation Engineers (SPIE) Conference Series*, Vol. 8446, *Ground-based and Airborne Instrumentation for Astronomy IV*, ed. I. S. McLean, S. K. Ramsay, & H. Takami, 844686
- Ben-Ami, S., Gal-Yam, A., Mazzali, P. A., et al. 2014, *The Astrophysical Journal*, 785, 37
- Bersten, M. C., Benvenuto, O. G., Nomoto, K., et al. 2012, *ApJ*, 757, 31
- Bersten, M. C., Folatelli, G., García, F., et al. 2018, *Nature*, 554, 497
- Bianco, F. B., Modjaz, M., Hicken, M., et al. 2014, *ApJS*, 213, 19
- Blagorodnova, N., Neill, J. D., Walters, R., et al. 2018, *Publications of the Astronomical Society of the Pacific*, 130, 035003
- Branch, D., Baron, E., Hall, N., Melakayil, M., & Parrent, J. 2005, *PASP*, 117, 545
- Breeveld, A. A., Landsman, W., Holland, S. T., et al. 2011, in *American Institute of Physics Conference Series*, Vol. 1358, *Gamma Ray Bursts 2010*, ed. J. E. McEnery, J. L. Racusin, & N. Gehrels, 373–376
- Bruch, R. J., Gal-Yam, A., Schulze, S., et al. 2021, *ApJ*, 912, 46
- Brüns, R. C., & Kroupa, P. 2012, *A&A*, 547, A65
- Burrows, D. N., Hill, J. E., Nousek, J. A., et al. 2005, *SSRv*, 120, 165
- Calzetti, D., Armus, L., Bohlin, R. C., et al. 2000, *ApJ*, 533, 682
- Campana, S., Mangano, V., Blustin, A. J., et al. 2006, *Nature*, 442, 1008
- Cardelli, J. A., Clayton, G. C., & Mathis, J. S. 1989, *ApJ*, 345, 245
- Cenko, S. B., Fox, D. B., Moon, D.-S., et al. 2006, *PASP*, 118, 1396
- Chabrier, G. 2003, *PASP*, 115, 763
- Chambers, K. C., Magnier, E. A., Metcalfe, N., et al. 2016, arXiv:1612.05560
- Chevalier, R. A., & Fransson, C. 2006, *ApJ*, 651, 381
- Chevalier, R. A., & Irwin, C. M. 2011, *ApJL*, 729, L6
- Chevalier, R. A., & Liang, E. P. 1989, *ApJ*, 344, 332
- Conroy, C., Gunn, J. E., & White, M. 2009, *ApJ*, 699, 486
- Corsi, A., Ofek, E. O., Gal-Yam, A., et al. 2014, *ApJ*, 782, 42

- Curti, M., Cresci, G., Mannucci, F., et al. 2017, *MNRAS*, 465, 1384
- Dahiwal, A., & Fremling, C. 2020, *Transient Name Server Classification Report*, 2020-2811, 1
- De, K., Fremling, U. C., Gal-Yam, A., et al. 2021, *ApJL*, 907, L18
- De, K., Kasliwal, M. M., Ofek, E. O., et al. 2018, *Science*, 362, 201
- De, K., Kasliwal, M. M., Tzanidakis, A., et al. 2020, *ApJ*, 905, 58
- Deckers, M., Maguire, K., Magee, M. R., et al. 2022, *MNRAS*, 512, 1317
- Dekany, R., Smith, R. M., Riddle, R., et al. 2020, *PASP*, 132, 038001
- Dessart, L., Hillier, D. J., Woosley, S., et al. 2016, *MNRAS*, 458, 1618
- Dey, A., Schlegel, D. J., Lang, D., et al. 2019, *The Astronomical Journal*, 157, 168
- Dimitriadis, G., Foley, R. J., Rest, A., et al. 2018, *The Astrophysical Journal*, 870, L1
- Dwarkadas, V. V. 2011, *MNRAS*, 412, 1639
- Evans, P. A., Beardmore, A. P., Page, K. L., et al. 2007, *A&A*, 469, 379
- . 2009, *MNRAS*, 397, 1177
- Feroz, F., Hobson, M. P., & Bridges, M. 2009, *MNRAS*, 398, 1601
- Fields, C. E., & Couch, S. M. 2021, *The Astrophysical Journal*, 921, 28
- Filippenko, A. V. 1982, *PASP*, 94, 715
- Filippenko, A. V. 1997, *Annual Review of Astronomy and Astrophysics*, 35, 309
- Filippenko, A. V., Chornock, R., Swift, B., et al. 2003, *International Astronomical Union Circular*, 8159, 2
- Flewelling, H. A., Magnier, E. A., Chambers, K. C., et al. 2020, *ApJS*, 251, 7
- Foley, R. J., Smith, N., Ganeshalingam, M., et al. 2007, *ApJL*, 657, L105
- Foreman-Mackey, D., Sick, J., & Johnson, B. 2014, *Python-Fsps: Python Bindings To Fsps (V0.1.1)*, doi:10.5281/zenodo.12157
- Fraser, M., Magee, M., Kotak, R., et al. 2013, *ApJL*, 779, L8
- Fremling, C., Sollerman, J., Taddia, F., et al. 2016, *A&A*, 593, A68
- Förster, F., Moriya, T. J., Maureira, J. C., et al. 2018, *Nature Astronomy*, 2, 808, number: 10 Publisher: Nature Publishing Group
- Gagliano, A., Izzo, L., Kilpatrick, C. D., et al. 2022, *ApJ*, 924, 55
- Gal-Yam, A. 2017, in *Handbook of Supernovae*, ed. A. W. Alsabti & P. Murdin (Springer International Publishing AG), 195
- Gal-Yam, A., Kasliwal, M. M., Arcavi, I., et al. 2011, *ApJ*, 736, 159
- Gal-Yam, A., Arcavi, I., Ofek, E. O., et al. 2014, *Nature*, 509, 471
- Gal-Yam, A., Bruch, R., Schulze, S., et al. 2022, *Nature*, 601, 201
- Galbany, L., Anderson, J. P., Sánchez, S. F., et al. 2018, *ApJ*, 855, 107
- Ganot, N., Gal-Yam, A., Ofek, E. O., et al. 2016, *ApJ*, 820, 57
- Ganot, N., Ofek, E. O., Gal-Yam, A., et al. 2022, *The Astrophysical Journal*, 931, 71
- Garnavich, P. M., Tucker, B. E., Rest, A., et al. 2016, *The Astrophysical Journal*, 820, 23
- Gehrels, N., Chincarini, G., Giommi, P., et al. 2004, *ApJ*, 611, 1005
- Graham, M. J., Kulkarni, S. R., Bellm, E. C., et al. 2019, *PASP*, 131, 078001
- Granot, A., Nakar, E., & Levinson, A. 2018, *MNRAS*, 476, 5453
- Hachinger, S., Mazzali, P. A., Taubenberger, S., et al. 2012, *MNRAS*, 422, 70
- HI4PI Collaboration, Ben Bekhti, N., Flöer, L., et al. 2016, *A&A*, 594, A116
- Higson, E., Handley, W., Hobson, M., & Lasenby, A. 2019, *Statistics and Computing*, 29, 891
- Ho, A. Y. Q., Goldstein, D. A., Schulze, S., et al. 2019, *ApJ*, 887, 169
- Ho, A. Y. Q., Kulkarni, S. R., Perley, D. A., et al. 2020a, *ApJ*, 902, 86
- Ho, A. Y. Q., Perley, D. A., Kulkarni, S. R., et al. 2020b, *ApJ*, 895, 49
- Hook, I. M., Jørgensen, I., Allington-Smith, J. R., et al. 2004, *PASP*, 116, 425
- Hosh, A., Sfaradi, I., Ergon, M., et al. 2020, *ApJ*, 903, 132
- Hosseinzadeh, G., McCully, C., Zabludoff, A. I., et al. 2019, *ApJ*, 871, L9
- Hosseinzadeh, G., Kilpatrick, C. D., Dong, Y., et al. 2022, *ApJ*, 935, 31
- Hunter, D. J., Valenti, S., Kotak, R., et al. 2009, *A&A*, 508, 371
- Hunter, J. D. 2007, *Computing in Science & Engineering*, 9, 90
- Inserra, C., Smartt, S. J., Jerkstrand, A., et al. 2013, *ApJ*, 770, 128
- Irani, I., Schulze, S., Gal-Yam, A., et al. 2019, *ApJ*, 887, 127
- Irani, I., Prentice, S. J., Schulze, S., et al. 2022, *ApJ*, 927, 10
- Izzo, L., Auchettl, K., Hjorth, J., et al. 2020, *A&A*, 639, L11
- Jacobson-Galán, W., Venkatraman, P., Margutti, R., et al. 2022a, *arXiv e-prints*, arXiv:2203.03785
- Jacobson-Galán, W. V., Margutti, R., Kilpatrick, C. D., et al. 2020, *ApJ*, 898, 166
- Jacobson-Galán, W. V., Dessart, L., Jones, D. O., et al. 2022b, *ApJ*, 924, 15
- Jerkstrand, A., Ergon, M., Smartt, S. J., et al. 2015, *A&A*, 573, A12
- Johnson, B. D., Leja, J., Conroy, C., & Speagle, J. S. 2021, *ApJS*, 254, 22
- Jones, D. O., Foley, R. J., Narayan, G., et al. 2021, *ApJ*, 908, 143

- Junde, H. 1999, *Nuclear Data Sheets*, 86, 315
- Kasen, D. 2010, *ApJ*, 708, 1025
- Kasliwal, M. M., Kulkarni, S. R., Gal-Yam, A., et al. 2012, *ApJ*, 755, 161
- Katz, B., Sapir, N., & Waxman, E. 2011, arXiv e-prints, arXiv:1106.1898
- Katz, B., Sapir, N., & Waxman, E. 2012, in *Death of Massive Stars: Supernovae and Gamma-Ray Bursts*, ed. P. Roming, N. Kawai, & E. Pian, Vol. 279, 274–281
- Khazov, D., Yaron, O., Gal-Yam, A., et al. 2016, *ApJ*, 818, 3
- Kim, Y. L., Rigault, M., Neill, J. D., et al. 2022, *PASP*, 134, 024505
- Kromer, M., Fremling, C., Pakmor, R., et al. 2016, *Monthly Notices of the Royal Astronomical Society*, 459, 4428
- Kulkarni, S. R. 2013, *The Astronomer's Telegram*, 4807, 1
- Kurucz, R. L. 1995, in *ASP Conference Series*, Vol. 81, 583
- Kushnir, D., Katz, B., Dong, S., Livne, E., & Fernández, R. 2013, *ApJL*, 778, L37
- Kushnir, D., Wygoda, N., & Sharon, A. 2020, *MNRAS*, 499, 4725
- Lang, D. 2014, *AJ*, 147, 108
- Law, N. M., Kulkarni, S. R., Dekany, R. G., et al. 2009, *Publications of the Astronomical Society of the Pacific*, 121, 1395
- Levinson, A., & Nakar, E. 2020, *Physics Reports*, 866, 1, aDS Bibcode: 2020PhR...866....1L
- Lunnan, R., Kasliwal, M. M., Cao, Y., et al. 2017, *ApJ*, 836, 60
- Lupton, R., Blanton, M. R., Fekete, G., et al. 2004, *PASP*, 116, 133
- Maeda, K., & Moriya, T. J. 2022, arXiv:2201.00955 [astro-ph], arXiv: 2201.00955
- Maeda, K., Chandra, P., Matsuoka, T., et al. 2021, *The Astrophysical Journal*, 918, 34, publisher: American Astronomical Society
- Magee, M. R., & Maguire, K. 2020, *A&A*, 642, A189
- Magee, M. R., Maguire, K., Kotak, R., & Sim, S. A. 2021, *Monthly Notices of the Royal Astronomical Society*, 502, 3533
- Magee, M. R., Maguire, K., Kotak, R., et al. 2020, *A&A*, 634, A37
- Maguire, K. 2017, *Type Ia Supernovae*, ed. A. W. Alsabti & P. Murdin (Cham: Springer International Publishing), 293–316
- Margalit, B., Quataert, E., & Ho, A. Y. Q. 2022, *ApJ*, 928, 122
- Margutti, R., Milisavljevic, D., Soderberg, A. M., et al. 2013, *The Astrophysical Journal*, 780, 21
- Martin, D. C., Fanson, J., Schiminovich, D., et al. 2005, *ApJL*, 619, L1
- Martinez, L., Bersten, M. C., Anderson, J. P., et al. 2022, *A&A*, 660, A41
- Masci, F. J., Laher, R. R., Rusholme, B., et al. 2019, *Publications of the Astronomical Society of the Pacific*, 131, 018003
- Matsumoto, T., & Metzger, B. D. 2022, *ApJ*, 936, 114
- Matzner, C. D., & McKee, C. F. 1999, *The Astrophysical Journal*, 510, 379
- Mauerhan, J. C., Smith, N., Filippenko, A. V., et al. 2013, *Monthly Notices of the Royal Astronomical Society*, 430, 1801
- Medler, K., Mazzali, P. A., Teffs, J., et al. 2022, *Monthly Notices of the Royal Astronomical Society*, 513, 5540
- Milisavljevic, D., Patnaude, D. J., Raymond, J. C., et al. 2017, *ApJ*, 846, 50
- Miller, J. S., Robinson, L. B., & Goodrich, R. W. 1988, in *Instrumentation for Ground-Based Optical Astronomy*, 157
- Modjaz, M., Gutiérrez, C. P., & Arcavi, I. 2019, *Nature Astronomy*, 3, 717
- Morag, J., Sapir, N., & Waxman, E. 2022, arXiv e-prints, arXiv:2207.06179
- Mould, J. R., Huchra, J. P., Freedman, W. L., et al. 2000, *ApJ*, 529, 786
- Murase, K., Thompson, T. A., & Ofek, E. O. 2014, *MNRAS*, 440, 2528
- Nakar, E., & Sari, R. 2010, *ApJ*, 725, 904
- Nugent, P. E., Sullivan, M., Cenko, S. B., et al. 2011, *Nature*, 480, 344
- Nugis, T., & Lamers, H. J. G. L. M. 2000, *A&A*, 360, 227
- Ofek, E. O., Rabinak, I., Neill, J. D., et al. 2010, *ApJ*, 724, 1396
- Ofek, E. O., Sullivan, M., Cenko, S. B., et al. 2013, *Nature*, 494, 65
- Ofek, E. O., Sullivan, M., Shaviv, N. J., et al. 2014a, *ApJ*, 789, 104
- Ofek, E. O., Zoglauer, A., Boggs, S. E., et al. 2014b, *ApJ*, 781, 42
- Ofek, E. O., Adams, S. M., Waxman, E., et al. 2021, *The Astrophysical Journal*, 922, 247
- Oke, J. B., & Gunn, J. E. 1982, *PASP*, 94, 586
- Oke, J. B., Cohen, J. G., Carr, M., et al. 1995, *PASP*, 107, 375
- Oliphant, T. 2006, *Guide to NumPy*
- Pastorello, A., Smartt, S. J., Mattila, S., et al. 2007, *Nature*, 447, 829
- Pastorello, A., Cappellaro, E., Inserra, C., et al. 2013, *The Astrophysical Journal*, 767, 1
- Pellegrino, C., Howell, D. A., Terreran, G., et al. 2022, arXiv e-prints, arXiv:2205.07894
- Perets, H. B., Gal-Yam, A., Mazzali, P. A., et al. 2010, *Nature*, 465, 322
- Perez, F., & Granger, B. E. 2007, *Computing in Science and Engineering*, 9, 21
- Perley, D. A. 2019, *PASP*, 131, 084503
- Perley, D. A., Mazzali, P. A., Yan, L., et al. 2018, *Monthly Notices of the Royal Astronomical Society*, 484, 1031
- Perley, D. A., Ho, A. Y. Q., Yao, Y., et al. 2021, *MNRAS*, 508, 5138
- Perley, D. A., Sollerman, J., Schulze, S., et al. 2022, *ApJ*, 927, 180

- Pian, E., & Mazzali, P. A. 2017, *Hydrogen-Poor Core-Collapse Supernovae*, ed. A. W. Alsabti & P. Murdin (Cham: Springer International Publishing), 277–292
- Piascik, A. S., Steele, I. A., Bates, S. D., et al. 2014, in *Society of Photo-Optical Instrumentation Engineers (SPIE) Conference Series*, Vol. 9147, *Ground-based and Airborne Instrumentation for Astronomy V*, ed. S. K. Ramsay, I. S. McLean, & H. Takami, 91478H
- Piro, A. L. 2015, *ApJL*, 808, L51
- Piro, A. L., Haynie, A., & Yao, Y. 2021, *ApJ*, 909, 209
- Piro, A. L., & Morozova, V. S. 2016, *The Astrophysical Journal*, 826, 96
- Planck Collaboration, Aghanim, N., Akrami, Y., et al. 2018, arXiv e-prints, arXiv:1807.06209
- Podsiadlowski, P., Joss, P. C., & Hsu, J. J. L. 1992, *ApJ*, 391, 246
- Poznanski, D., Prochaska, J. X., & Bloom, J. S. 2012, *MNRAS*, 426, 1465
- Prentice, S., Maguire, K., Magee, M., & Deckers, M. 2020, *Transient Name Server Classification Report*, 2020-2674, 1
- Prentice, S. J., Maguire, K., Siebenaler, L., & Jerkstrand, A. 2022, *MNRAS*, 514, 5686
- Prentice, S. J., Maguire, K., Boian, I., et al. 2020, *Monthly Notices of the Royal Astronomical Society*, 499, 1450
- Prochaska, J., Hennawi, J., Westfall, K., et al. 2020, *The Journal of Open Source Software*, 5, 2308
- Rabinak, I., & Waxman, E. 2011, *ApJ*, 728, 63
- Relaño, M., & Kennicutt, Robert C., J. 2009, *ApJ*, 699, 1125
- Rho, J., Evans, A., Geballe, T. R., et al. 2021, *The Astrophysical Journal*, 908, 232
- Richtler, T. 2003, in *Stellar Candles for the Extragalactic Distance Scale*, ed. D. Alloin & W. Gieren, Vol. 635, 281–305
- Ridnaia, A., Svinkin, D., & Frederiks, D. 2020, *J. Phys. Conf. Ser.*, 1697, 012030
- Rigault, M., Neill, J. D., Blagorodnova, N., et al. 2019, *A&A*, 627, A115
- Roberson, M., Fremling, C., & Kasliwal, M. 2022, *The Journal of Open Source Software*, 7, 3612
- Rodríguez, Ó., Maoz, D., & Nakar, E. 2022, arXiv e-prints, arXiv:2209.05552
- Roming, P. W. A., Kennedy, T. E., Mason, K. O., et al. 2005, *SSRv*, 120, 95
- Rubin, A., & Gal-Yam, A. 2017, *The Astrophysical Journal*, 848, 8
- Rubin, A., Gal-Yam, A., Cia, A. D., et al. 2016, *The Astrophysical Journal*, 820, 33
- Salim, S., Rich, R. M., Charlot, S., et al. 2007, *ApJS*, 173, 267
- Sapir, N., & Waxman, E. 2017, *ApJ*, 838, 130
- Savitzky, A., & Golay, M. J. E. 1964, *Analytical Chemistry*, 36, 1627
- Scalzo, R., Aldering, G., Antilogus, P., et al. 2014, *MNRAS*, 440, 1498
- Schlafly, E. F., & Finkbeiner, D. P. 2011, *ApJ*, 737, 103
- Schlegel, D. J., Finkbeiner, D. P., & Davis, M. 1998, *ApJ*, 500, 525
- Schulze, S., Yaron, O., Sollerman, J., et al. 2021, *ApJS*, 255, 29
- Shappee, B. J., Holoiien, T. W.-S., Drout, M. R., et al. 2018, *The Astrophysical Journal*, 870, 13
- Sharon, A., & Kushnir, D. 2020, *MNRAS*, 496, 4517
- . 2023, *MNRAS*, 522, 6264
- Shvartzvald, Y., Waxman, E., Gal-Yam, A., et al. 2023, arXiv e-prints, arXiv:2304.14482
- Silverman, J. M., Foley, R. J., Filippenko, A. V., et al. 2012, *MNRAS*, 425, 1789
- Skilling, J. 2004, in *American Institute of Physics Conference Series*, Vol. 735, *Bayesian Inference and Maximum Entropy Methods in Science and Engineering: 24th International Workshop on Bayesian Inference and Maximum Entropy Methods in Science and Engineering*, ed. R. Fischer, R. Preuss, & U. V. Toussaint, 395–405
- Skilling, J. 2006, *Bayesian Analysis*, 1, 833
- Skrutskie, M. F., Cutri, R. M., Stiening, R., et al. 2006, *AJ*, 131, 1163
- Smith, N. 2014, *ARA&A*, 52, 487
- Smith, R. J., Piascik, A. S., Steele, I. A., & Barnsley, R. M. 2016, in *Society of Photo-Optical Instrumentation Engineers (SPIE) Conference Series*, Vol. 9913, *Software and Cyberinfrastructure for Astronomy IV*, ed. G. Chiozzi & J. C. Guzman, 991317
- Soderberg, A. M., Berger, E., Page, K. L., et al. 2008, *Nature*, 453, 469
- Soumagnac, M. T., Ofek, E. O., Gal-yam, A., et al. 2019, *ApJ*, 872, 141
- Soumagnac, M. T., Ganot, N., Irani, I., et al. 2020, *ApJ*, 902, 6
- Speagle, J. S. 2020, *MNRAS*, 493, 3132
- Stahl, B. E., Zheng, W., de Jaeger, T., et al. 2019, *MNRAS*, 490, 3882
- Steele, I. A., Smith, R. J., Rees, P. C., et al. 2004, in *Society of Photo-Optical Instrumentation Engineers (SPIE) Conference Series*, Vol. 5489, *Ground-based Telescopes*, ed. J. Oschmann, Jacobus M., 679–692
- Stritzinger, M., Mazzali, P. A., Sollerman, J., & Benetti, S. 2006, *A&A*, 460, 793
- Stritzinger, M. D., Taddia, F., Burns, C. R., et al. 2018, *A&A*, 609, A135
- Strotjohann, N. L., Ofek, E. O., Gal-Yam, A., et al. 2015, *ApJ*, 811, 117
- . 2021, *ApJ*, 907, 99
- Svirski, G., Nakar, E., & Sari, R. 2012, *ApJ*, 759, 108
- Swartz, D. A., Sutherland, P. G., & Harkness, R. P. 1995, *ApJ*, 446, 766
- Taddia, F., Sollerman, J., Leloudas, G., et al. 2015, *A&A*, 574, A60



- Taddia, F., Fremling, C., Sollerman, J., et al. 2016, *A&A*, 592, A89
- Taddia, F., Sollerman, J., Fremling, C., et al. 2018, *A&A*, 609, A106
- Tartaglia, L., Sand, D. J., Valenti, S., et al. 2018, *ApJ*, 853, 62
- Teffs, J., Ertl, T., Mazzali, P., Hachinger, S., & Janka, H. T. 2020, *MNRAS*, 499, 730
- Terreran, G., Jacobson-Galán, W. V., Groh, J. H., et al. 2022, *ApJ*, 926, 20
- Tinyanont, S., Ridden-Harper, R., Foley, R. J., et al. 2022, *MNRAS*, 512, 2777
- Tonry, J. L., Denneau, L., Heinze, A. N., et al. 2018, *Publications of the Astronomical Society of the Pacific*, 130, 064505
- Valenti, S., Elias-Rosa, N., Taubenberger, S., et al. 2008, *ApJL*, 673, L155
- Valenti, S., Yuan, F., Taubenberger, S., et al. 2014, *MNRAS*, 437, 1519
- Varma, V., & Müller, B. 2021, *Monthly Notices of the Royal Astronomical Society*, 504, 636
- Virtanen, P., Gommers, R., Oliphant, T. E., et al. 2020, *Nature Methods*, 17, 261
- Waxman, E., & Katz, B. 2017, in *Handbook of Supernovae*, ed. A. W. Alsabti & P. Murdin, 967
- Waxman, E., Mészáros, P., & Campana, S. 2007, *ApJ*, 667, 351
- Weaver, T. A. 1976, *ApJS*, 32, 233
- Woosley, S. E., Sukhbold, T., & Kasen, D. N. 2021, *ApJ*, 913, 145
- Wright, A. H., Robotham, A. S. G., Bourne, N., et al. 2016, *MNRAS*, 460, 765
- Wright, E. L., Eisenhardt, P. R. M., Mainzer, A. K., et al. 2010, *AJ*, 140, 1868
- Yaron, O., & Gal-Yam, A. 2012, *Publications of the Astronomical Society of the Pacific*, 124, 668
- Yaron, O., Perley, D. A., Gal-Yam, A., et al. 2017, *Nature Physics*, 13, 510
- Yoon, S. C., Woosley, S. E., & Langer, N. 2010, *ApJ*, 725, 940
- Yoshida, T., Takiwaki, T., Kotake, K., et al. 2021, *The Astrophysical Journal*, 908, 44
- Zackay, B., Ofek, E. O., & Gal-Yam, A. 2016, *ApJ*, 830, 27
- Zimmerman, E., Irani, I., Bruch, R., et al. 2022, *Transient Name Server AstroNote*, 142, 1
- Zou, H., Zhou, X., Fan, X., et al. 2017, *Publications of the Astronomical Society of the Pacific*, 129, 064101

## Appendix A

### A.1 SN 2020scb

In this paper, we publish the light curves of SN 2020scb (ZTF20abwxywy), a SN Ic detected by ZTF on UT August 26.38, 2020, and classified as a SN Ic shortly after (Prentice et al. 2020). SN 2020scb exploded in the face-on spiral CGCG 456-055, at a redshift of  $z = 0.017429$ , for which we adopt a distance estimate of 76.1 Mpc, corrected for Virgo, Great Attractor and Shapley supercluster infall as discussed in § 2.1. We acquired ZTF, LT/IO:O, and *Swift*/UVOT photometry of the SN using the methods described in Sec 3.2, and correct these for a Galactic extinction value of 0.052 mag. We also infer a host-galaxy extinction of  $E(B - V) = 0.022$  mag using the  $g - r$  color 10 days after maximum light (Stritzinger et al. 2018), as discussed in § 2.3. We recover a pre-discovery detection of  $r = 20.53 \pm 0.16$  mag on August 25.36, following a non-detection 0.9 day prior. Our high cadence light curve and rapid UVOT triggering allowed us to acquire UV photometry by August 26.668, only 2.2 days after the non-detection, and 1.3 days after the first detection - making SN 2020scb one of the earliest observed SNe Ic in the UV. We fit the early  $t - t_{first} < 5$  days light curve to a power-law evolution in the radius and temperature according to Eq. 1, and find a good fit for  $t_0 = \text{JD } 2459086.3 \pm 0.3$  days. The spectral data for this object will be published together with the rest of the ZTF SNe Ic (Yang et al., in prep.).

### A.2 Shock-Cooling Models

For § 5, we fit intermediate-time observations to the shock-cooling model of Morag et al. (2022). This model describes the blackbody evolution of a cooling envelope until recombination or sufficient transparency of the envelope, using a set of four free parameters: (1)  $R_{13}$ , the radius of the progenitor star in units of  $10^{13}$  cm, (2)  $f_\rho M_0$ , where  $f_\rho$  describes the structure of the density near the edge of the stellar envelope and  $M_0$  is the progenitor mass prior to the SN in units of  $M_\odot$ , (3)  $v_{s*,8.5}$ , the shock-velocity parameter in units of  $10^{8.5}$   $\text{cm s}^{-1}$ , which roughly corresponds to  $v_{ej}/5$ , and (4)  $M_{env}$ , the envelope mass; also,  $\kappa_{0.34}$  is the opacity in units of  $0.34 \text{ cm}^2 \text{ g}^{-1}$ , and  $t_d/t_{hr}$  is the time since explosion in units of days or hours (respectively). Following their notation,  $L$  and  $T$  evolve according to

$$L_{SC} = L_{\text{planar}} + 0.9 \exp \left[ - \left( \frac{2t}{t_{\text{tr}}} \right)^{0.5} \right] L_{\text{RW}}, \quad (\text{A1})$$

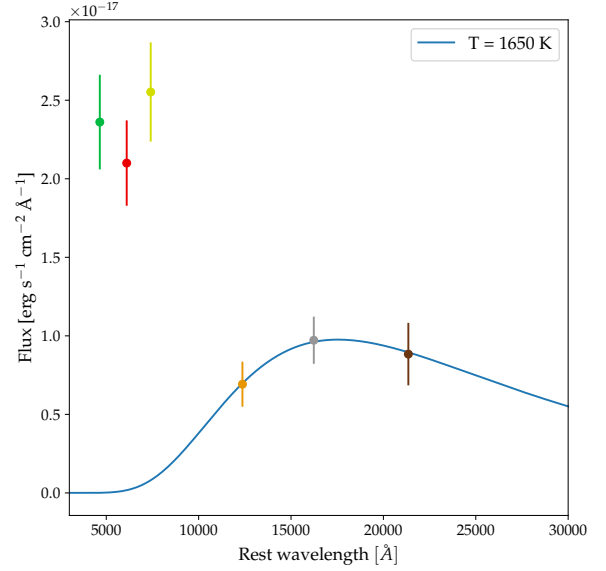


**Figure A1.** Blackbody fit to the SED of SN 2022oqm at  $t = 66$  days, fit separately for  $JHK_s$  bands. The best-fit blackbody has a temperature of 1650 K and a radius of  $4.4 \times 10^{15}$  cm, consistent with the size of the system at  $t = 66$  days. We did not fit a blackbody to the optical component, since the spectrum is line dominated.

$$T_{\text{col}} = 1.1 \min [T_{\text{ph,planar}}, T_{\text{ph,RW}}], \quad (\text{A2})$$

which are valid during

$$3R/c = 17 R_{13} \min < t < \min [t_{0.7\text{eV}}, t_{\text{tr}}/2]. \quad (\text{A3})$$

The terms in Eqs. (A1–A3) are

$$\frac{L_{\text{planar}}}{10^{42} \text{ erg s}^{-1}} = 3.01 R_{13}^{2.46} v_{s*,8.5}^{0.60} (f_\rho M_0)^{-0.06} t_{\text{hr}}^{-4/3} \kappa_{0.34}^{-1.06}, \quad (\text{A4})$$

$$\frac{T_{\text{ph,planar}}}{\text{eV}} = 6.94 R_{13}^{0.12} v_{s*,8.5}^{0.15} (f_\rho M_0)^{-0.02} \kappa_{0.34}^{-0.27} t_{\text{hr}}^{-1/3}, \quad (\text{A5})$$

$$\frac{L_{\text{RW}}}{2.08 \times 10^{42} \text{ erg s}^{-1}} = R_{13} v_{s*,8.5}^{1.91} (f_\rho M_0)^{0.09} \kappa_{0.34}^{-0.91} t_d^{-0.17}, \quad (\text{A6})$$

$$\frac{T_{\text{ph,RW}}}{\text{eV}} = 1.66 R_{13}^{1/4} v_{s*,8.5}^{0.07} (f_\rho M_0)^{-0.03} \kappa_{0.34}^{-0.28} t_d^{-0.45}, \quad (\text{A7})$$

$$t_{0.7\text{eV}} = 6.86 R_{13}^{0.56} v_{s*,8.5}^{0.16} \kappa_{0.34}^{-0.61} (f_\rho M_0)^{-0.06} \text{ days}, \quad (\text{A8})$$

$$\text{and } t_{\text{tr}} = 19.5 \sqrt{\frac{\kappa_{0.34} M_{\text{env},0}}{v_{s*,8.5}}} \text{ days}. \quad (\text{A9})$$

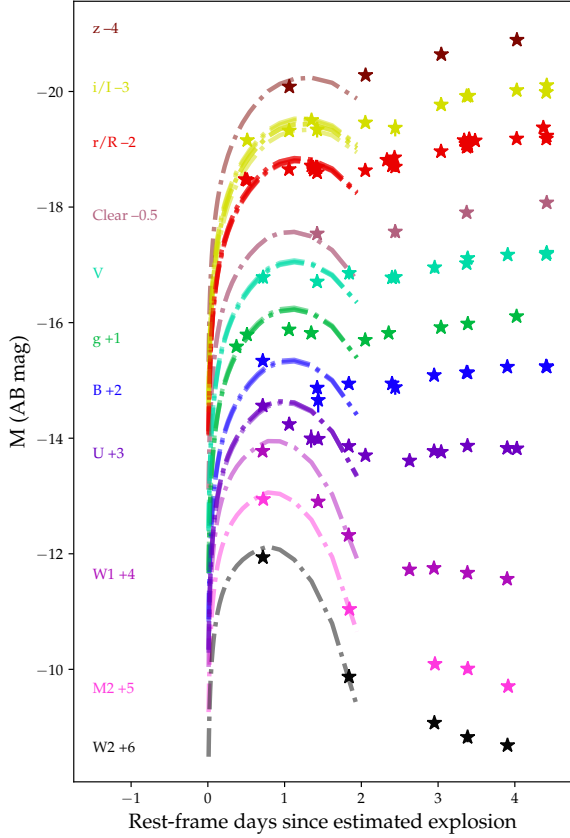


**Figure A2.** Best Piro et al. (2021) shock-cooling fits to the light curves of SN 2022oqm, for a model with  $M_e = 0.05 M_\odot$ ,  $R_e = 110 R_\odot$ , and  $E = 1.5 \times 10^{50}$  erg.

In addition to the luminosity set by the shock-cooling component, we assume a  $^{56}\text{Ni}$  decay component, such that the temperature is simply  $T_{\text{col}}$  and the total luminosity is a sum of Eqs. A1 and 5:

$$L = L_{56\text{Ni}} + L_{SC}, \quad T = T_{\text{col}}. \quad (\text{A10})$$

Since the validity of this model is dependent on the model parameters, a  $\chi^2$  minimization is not applicable. Instead, we fit this model with a likelihood function adapted for a variable validity domain, as discussed in detail by Soumagnac et al. (2020):

$$\mathcal{L} = \text{PDF}(\chi^2, \text{dof}); \quad \chi^2 = \sum_i \frac{f_i - m_i}{\sigma_i^2}, \quad (\text{A11})$$

where PDF is the  $\chi^2$  distribution given the number of degrees of freedom,  $f_i$  are the observed fluxes,  $\sigma_i$  are the observational uncertainties including a 10% systematic

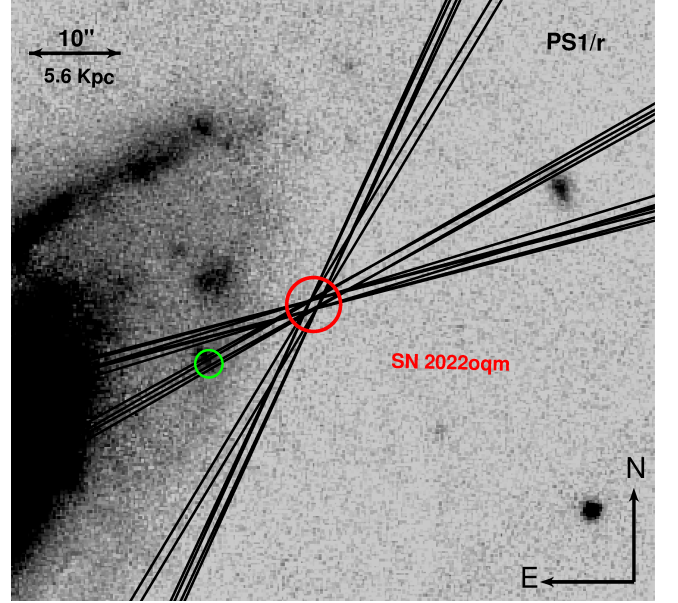


**Figure A3.** The host environment of SN 2022oqm, displayed using PS1  $r$ -band images overlaid with the 8 NOT and GMOS spectra slit orientations. Slits are drawn with a representative width of  $1''$ . The nearest (3.8 kpc) H II region we identify is marked with a green circle.

error, and  $m_i$  are the integrated synthetic fluxes for the model. We do not treat deviations from a blackbody spectrum in our fitting process.

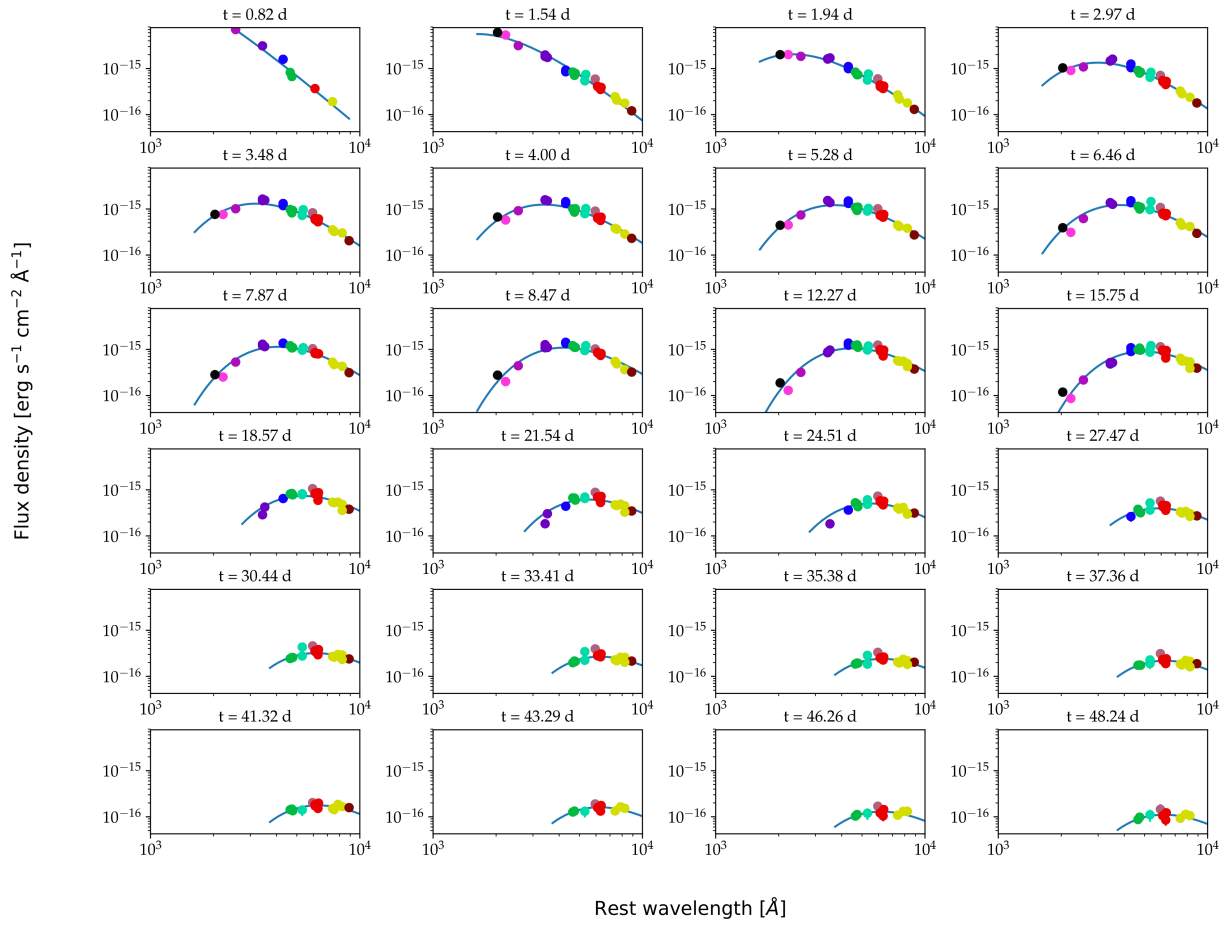
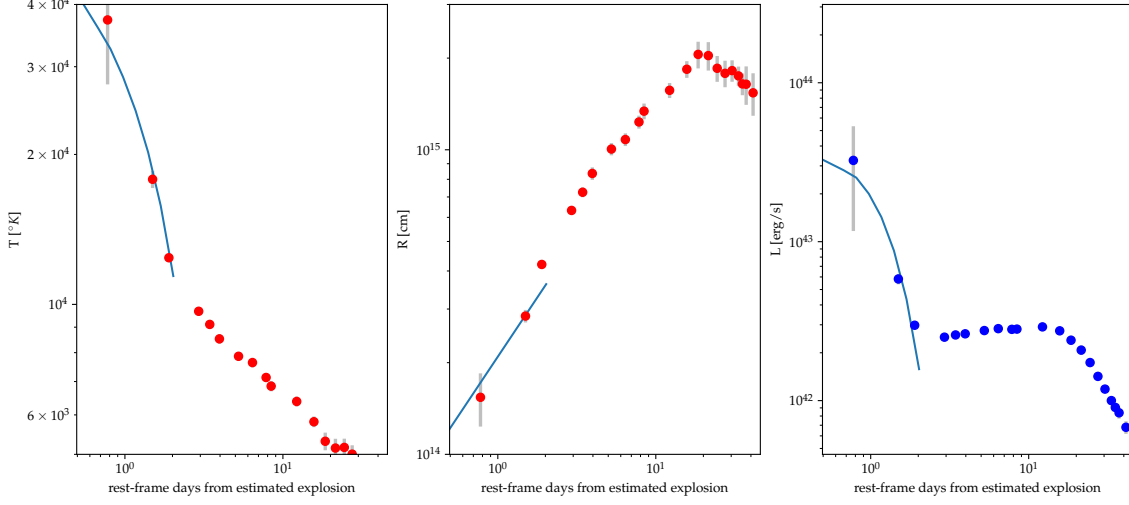
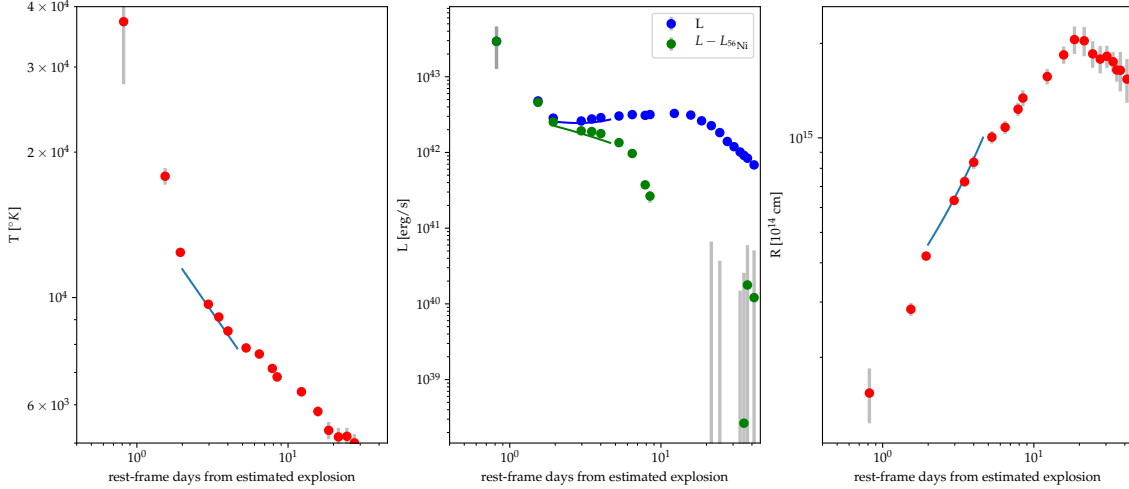


Figure A4. Blackbody fits to the photometry of SN 2022oqm.



**Figure A5.** The blackbody evolution of the best-fitting shock-cooling Piro et al. (2021) model with the blackbody evolution of SN 2022oqm. The models are plotted up to  $t = t_{\text{ph}}$ , when the envelope becomes fully transparent.



**Figure A6.** The blackbody evolution of the best-fit shock-cooling model to the intermediate-time ( $5 > t > 2$  days) light curve, along with the blackbody of SN 2022oqm at these times. In the middle panel, we show both the combined  $^{56}\text{Ni}$  and shock-cooling luminosity (blue line) with the bolometric luminosity of SN 2022oqm (blue points), and the shock-cooling fit alone (green curve), with the residual bolometric luminosity from the  $^{56}\text{Ni}$  fit (green curve). The best-fit model is plotted at  $t < t_{\text{tr}}/2 = 4.6$  days.

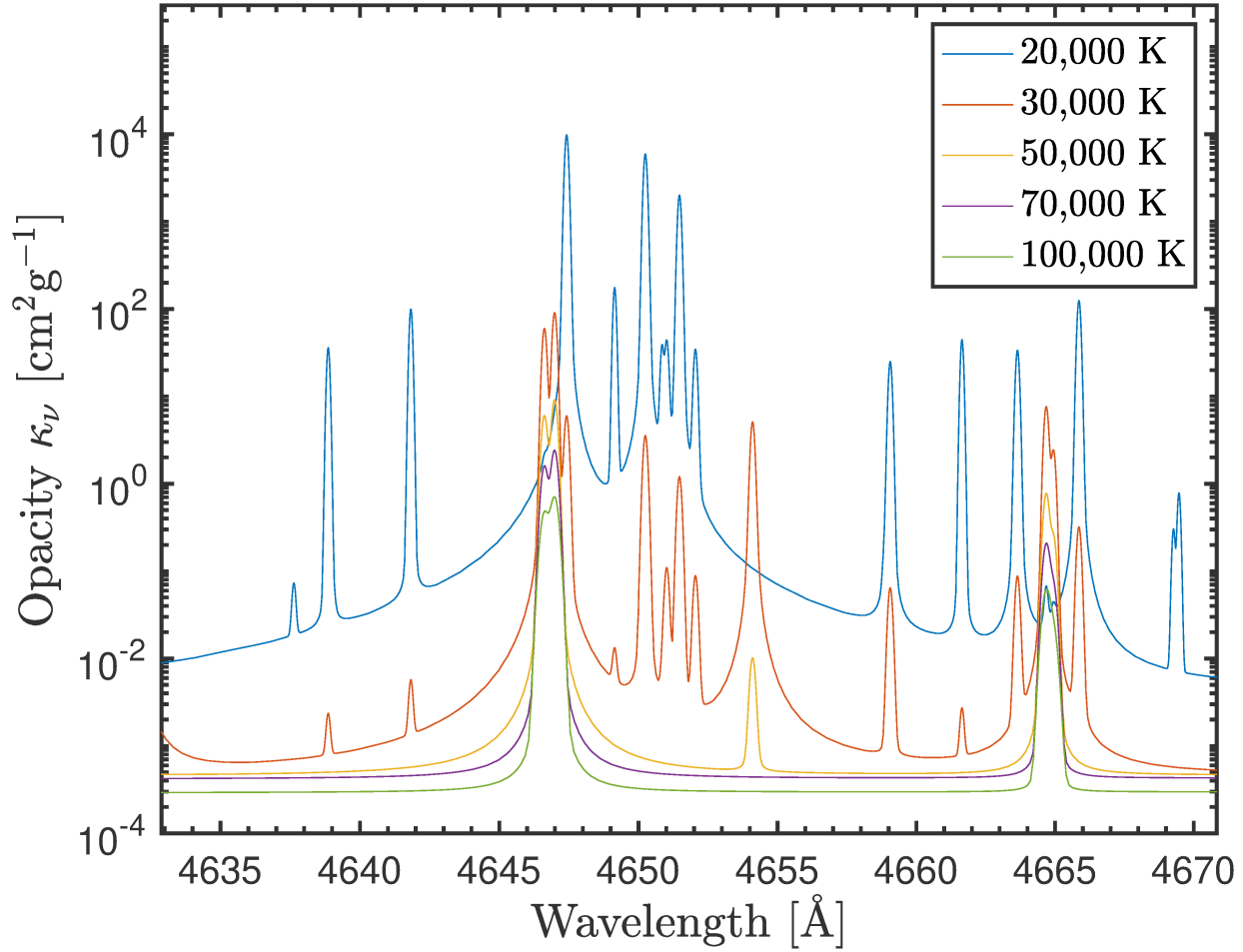


**Figure A7.** Line opacities, produced using the code of [Morag et al. \(2022\)](#) for an equal C/O composition near 4650 Å. For illustration purposes, we show the most constraining (i.e., the highest) set of opacities we acquired for a density of  $\rho = 10^{-12} \text{ g cm}^{-3}$  and at various CSM temperatures.

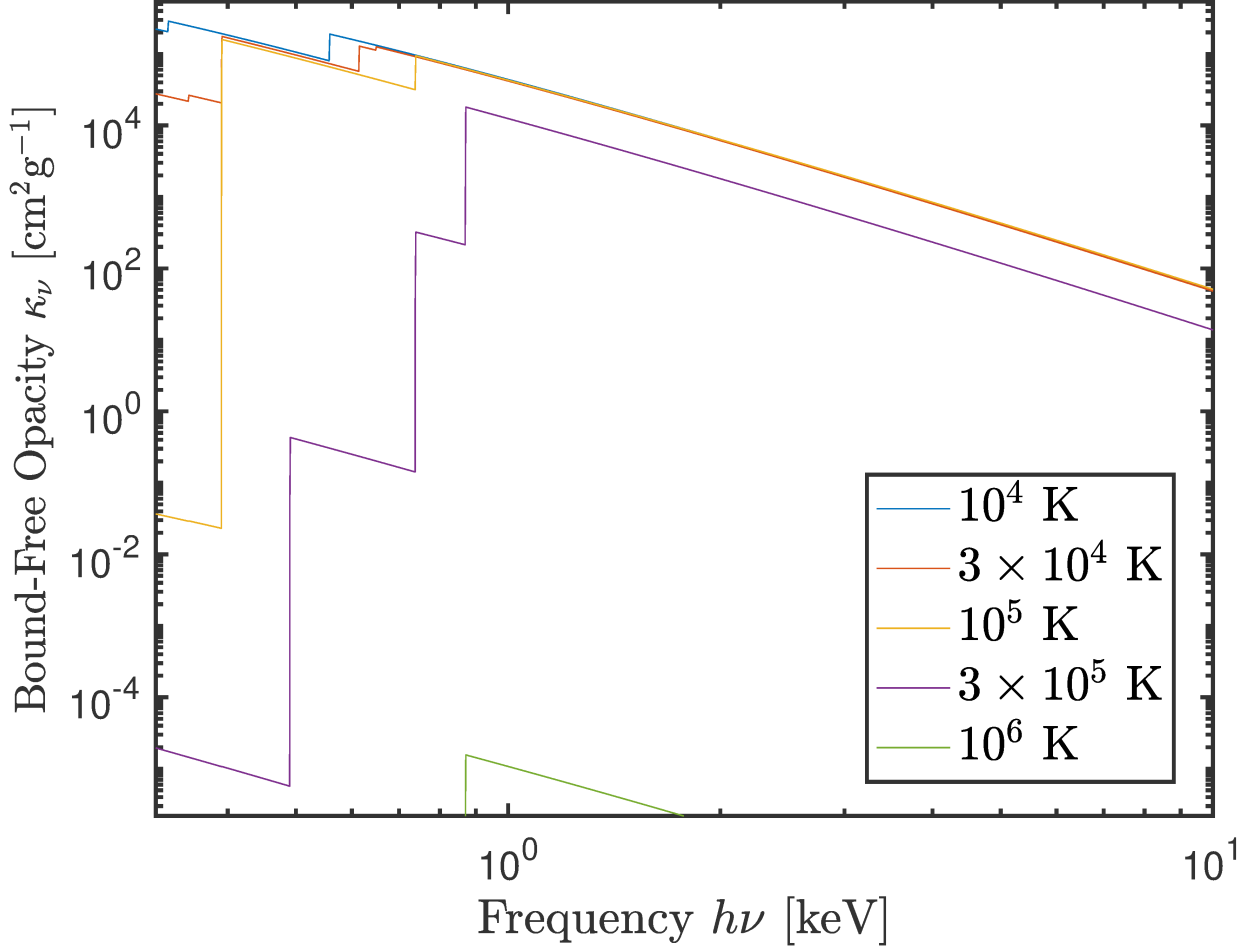


**Figure A8.** Bound-free opacities in the *Swift*/XRT band (0.3–10 keV), produced using the code of [Morag et al. \(2022\)](#) for an equal He/C/O composition. For illustration purposes, we show the most constraining (i.e., the lowest) set of opacities we acquired for a density of  $\rho = 10^{-12}$  g cm<sup>-3</sup> and at various CSM temperatures. These opacities are representative of various fractions of He in the composition.